

DOCTORAL THESIS

**On the effects of the Initial Mass
Function on galactic chemical
enrichment: the role of Pair
Instability Supernovae**

Candidate:

Sabyasachi Goswami

Supervisors:

Prof. Alessandro Bressan

Dr. Laura Silva

Prof. Andrea Lapi

*A thesis submitted in fulfillment of the requirements
for the degree of Doctor Philosophie*

in

Astrophysics & Cosmology



SISSA



“Nothing in life is to be feared, it is only to be understood. Now is the time to understand more, so that we may fear less. ”

— Marie Curie

Abstract

Big Bang nucleosynthesis produced H and He and some other light elements. Essentially all of the elements that are heavier than lithium were produced by stellar nucleosynthesis in evolving and exploding stars. The first stars which were formed were metal free and, possibly, very massive. The first heavy elements were formed through the evolution of the first stars and were ejected in the inter stellar medium (ISM) when they died. The subsequent generation of stars have formed out of this metal-rich gas and hence, when they died, they further enriched the ISM. This process is still continuing. The abundance pattern of the elements that we see today, gives us valuable information about the processes which contributed to the formation of these elements and about the different populations which exist in the Universe. With the advent of the large spectroscopic surveys, a large amount of abundance data has been and is being collected. This provides a unique opportunity, for galactic chemical evolution (GCE) studies, to understand and constrain better the evolution of the early universe, the star formation histories of galaxies and, ultimately, their current properties. One of the main ingredients of GCE models are stellar yields. Stellar yields are the amount of newly produced metals that are ejected into the ISM during and at the end of the life cycle of stars. Stars of different masses and metallicities go through different nuclear cycles and hence produce different elements. A large amount of work exists on stellar evolution and on the elements they synthesize. Stellar yields are then adopted in chemical evolution studies to interpret observed abundances in terms of galaxy evolution properties. Among the ejecta, those from very massive objects (VMOs) have not been studied in much detail yet. VMOs are stars with masses in the range $100 \lesssim M_i / M_\odot \lesssim 300 M_\odot$. They may enter the pair instability regime prior or during central oxygen burning, which may trigger a final thermonuclear explosion. In that case, they end up ejecting a large amount of elements such as ^{16}O , ^{24}Mg , ^{28}Si , S, Ar, Ca, Ti and Fe, due to C and O ignition within a collapsing core. There has been also recent evidence showing that these massive stars could have also played an important role in the early universe. In this thesis, I concentrate on the modelling of the ejecta of VMOs and on investigating their role in galaxy evolution with GCE models.

Massive and very massive stars contribute to the chemical enrichment of galaxies via both stellar winds and much more energetic stellar explosions. In the first part of the thesis, I use the PARSEC models of massive stars and VMOs to derive their stellar wind ejecta. These models are interfaced with explosive ejecta models to compute complete stellar ejecta tables, covering a wide range of initial masses and metallicities. The initial mass range includes the contribution of VMO, up to $M_i = 350 M_\odot$, with explosive ejecta for e-Capture Supernovae (ECSN), Core-Collapse Supernovae (CCSN), Pulsational Pair Instability SN (PPISN), and of Pair Instability SN (PISN) taken from the recent literature. These new ejecta are incorporated in a chemical evolution model to analyse the impact of varying the initial mass function(IMF) and its upper mass limit.

Additionally, we have tested different sets of chemical yields and checked their ability in reproducing the observed chemical abundances in the Milky Way (MW). For this purpose we have collected from the literature various sets of yields, that cover the contributions from low-, intermediate-mass and massive stars, the latter being usually provided up to $M_i \approx 100 M_\odot$. Our reference yields for AGB stars are computed with the COLIBRI code.

We use a one-zone chemical evolution code, CHE-EVO for simulating the chemical evolution of the MW and we focus primarily on the thick and thin disc populations. To this aim, we use recent data which are based on accurate abundance measurements and kinematic classification. We create a large grid of models using the different yield sets we adopted to reproduce some of the observational constraints and the abundance patterns separately for the thin and the thick disc. Our priority was the reproduce the $[\text{O}/\text{Fe}]$ vs. $[\text{Fe}/\text{H}]$ relation together with some observable constraints, i.e. the star formation rate, the $[\text{Fe}/\text{H}]$ distribution, and the supernovae rates. The difference in the two populations was most clear for the case of oxygen. Furthermore, for another commonly observed element, Mg, the stellar yield are not yet robust. Hence, I generally choose oxygen as the reference element to analyze.

The thin disc is on average more metal-rich and younger as compared to the thick disc and hence we use different star formation histories for the two populations. We find that, with most of the yield sets adopted in the study, we are able to reproduce the the previous paragraph and the $[\text{O}/\text{Fe}]$ vs $[\text{Fe}/\text{H}]$ relation for thin-disc stars.

The thick disc stellar population is older and show higher $[\alpha/\text{Fe}]$ ratios, compared to the thin disc. Obviously, we could not reproduce the thick disc using the same models adopted for the thin disc. In searching for alternative models, we first investigated the importance of stellar rotation adopting also yields from rotating stars, as has been suggested in the literature. In a second step, we also changed the upper mass limit of the IMF and the slope in the high mass domain, to see if we can reproduce the thick disc by including, in the chemical evolution, the effects of the VMOs. We found out that rotation is helpful in reproducing the thick disc as it helps to increase the oxygen production due to shear mixing. But the $[\text{O}/\text{Fe}]$ vs. $[\text{Fe}/\text{H}]$ slope of the models does not exactly match the observed trend of the thick disc data. On the other hand, by increasing the upper mass limit and changing the IMF slope in the high mass domain we were able to bracket the entire thick disc population with the right $[\text{O}/\text{Fe}]$ vs $[\text{Fe}/\text{H}]$ slope. Hence, we conclude that the effect of the VMOs, and their later evolutionary stages such as the PISN, should be included in chemical evolution studies because they could have played an important role at low metallicities.

We have then investigated the impact of VMOs on the evolution of nearby extremely metal-poor low mass starburst galaxies (EMPGs). The study of extremely metal-poor stars is extremely important since it allows us to directly analyse the

early stages of galaxy evolution. Recently, two EMPGs have been observed with peculiarly high Fe/O ratios at low metallicities compared to the other EMPGs in the study. Another striking peculiarity of these EMPGs, could be the observed fast decrease of the (Fe/O) at increasing (O/H) abundance, in spite of having similar low masses and similar high specific star formation rates. Since massive stars which undergo the PISN phase depending on the mass of the He core and metallicities, they produce large amounts of iron and oxygen at lower metallicities where PISN is more active, I investigate if I could reproduce the high Fe/O and the fast decreasing trend with metallicity, using the VMOs yields. To this aim, we have run various models by changing the upper mass limit and the slope in the high mass domain of the IMF. I conclude that, by increasing the upper mass limit to $300 M_{\odot}$ and adopting a top-heavy IMF, I could indeed reach the required large Fe/O ratios. But the reproduction of the observed EMPGs sequence of data suggested the necessity of a recalibration of the PISN ejecta, in terms of the maximum metallicity for the fading away of this uncertain stellar phase. Anyway this work further strengthens the contribution of PISN in the earlier stages of the universe and hence, it cannot be ignored in chemical evolution modelling. If the effect is confirmed, this could also be another piece of evidence that the IMF has not a universal shape.

As a work still in progress, I have investigated the low metallicity evolution of the relative abundance of the CNO elements, that is known to be a challenging problem for chemical evolution studies. It has been suggested that to reproduce these ratios, the stellar rotation should be accounted, especially to explain the nitrogen at low metallicities. Since all these investigations adopt a canonical IMF, I used the yields including VMOs, discussed above, to test their impact on the (C/O) and (N/O) evolution. My conclusion is that, although I am able to find the observed trend of the (C/O) ratio at low metallicities, the model overpredict the final metallicity and the (N/O) ratio is still not simultaneously reproduced. Hence, more work needs to be done on this subject.

In particular, I suggest performing a thorough analysis with models that include rotation, VMOs and possibly modulation of the IMF with the metallicity, the latter having been already suggested in the literature.

Acknowledgements

Foremost, I would like to express my sincere gratitude to my supervisors Prof. Alessandro Bressan, Dr. Laura Silva and Prof. Andrea Lapi for the continuous support of my PhD study and research, for their patience, motivation, honesty, enthusiasm, and immense knowledge. I could not have imagined having better advisors and mentors for my PhD. Working closely with Sandro has not only developed me immensely as a researcher but also the number of things and the ways to approach a problem that I have learned from him during my PhD will be staying with me for the rest of my research career. I thank Laura, for guiding me with all her knowledge, calm and for always being available even if being from a different institute in Trieste. I thank Andrea for always being so supportive and kind to me during my PhD tenure. I have learnt how to be so productive and so prompt from him.

I would also like to thank all the professors in the Astrophysics and Cosmology department of SISSA for their lectures in the first year of the PhD. Generally in a PhD, we are so busy with our own research that we don't get time to study much about other topics. Thanks to the coursework of SISSA that it was not only helpful for my thesis but also to get a broad idea about different fields in Astrophysics and Cosmology. Work becomes more fun when you have wonderful people around. The Astrophysics group has an extremely friendly and social environment. From journal clubs to barbecues to paintball trips to football, one cannot ask for a more fruitful environment for not only work but overall day to day life. Taking names would make a long list but I would like to thank everyone who was part of the group and more especially my office mates during my tenure.

SISSA, in general, offers a unique atmosphere which one might not get in Trieste. People coming from different parts and all very open and welcoming make the social part of the work culture very lively. The administrative staff deserves a special thanks for taking care of all the bureaucracy which would have been a nightmare for international students if they hadn't helped us so much.

Family and friends generally do not contribute to our research directly, but they keep us sane so that we can carry our research productively. Firstly, I would like to thank my family: my parents Mr. Samir Kumar Goswami and Mrs. Jyotsna Goswami and my sister Mrs. Mrinmoyee Goswami and brother-in-law Mr. Pallab Biswas for always being so supportive in whatever I do and taking care of everything back in India so that I can happily do my research here.

I initially thought of adding a List of friends to acknowledge like the List of figures etc, but due to reasons, I would like to thank everyone, from 'Nadaan Parindey' group to various football groups I was part of to Babel to people from SISSA I met and to people I met randomly and ended up becoming friends. Without these people, the experience and life in Trieste wouldn't have been the same.

People make memories, and certainly, without the people mentioned here, in brief, this thesis wouldn't have been possible.

Contents

Abstract	ii
Acknowledgements	v
List of Tables	ix
List of Figures	x
1 Introduction	1
1.1 Stellar populations	1
1.2 Stellar mass ranges	2
1.3 Stellar IMF	3
1.4 This thesis	4
2 Chemical evolution and stellar ejecta	6
2.1 Stellar classes and mass limits	8
2.2 Chemical ejecta of massive and very massive stars using PARSEC models	9
2.2.1 Evolutionary models	9
2.2.2 Calculation of the chemical ejecta	12
2.2.3 Wind ejecta	12
2.2.4 Explosion ejecta of electron capture supernovae	13
2.2.5 Explosion ejecta of core collapse supernovae	14
2.2.6 Explosion ejecta of pulsational pair instability and pair instability supernovae	17
2.2.7 Ejecta of very massive stars that directly collapse to black holes	20
2.3 Ejecta of AGB stars	22
2.4 Chemical ejecta from other authors	22
3 Modelling chemical evolution: code, data, parameters	30
3.1 Method to choose the data	32
3.1.1 Chemical properties of stars in the solar vicinity	33
3.1.2 Selection of Data	34
3.2 Effect of Model parameters	37
3.2.1 Effect of k-sch	37
3.2.2 Effect of the gas infall timescale, τ_{inf}	39
3.2.3 Effects of varying the parameter ASNIa	39

3.2.4	Effect of varying the start formation rate efficiency, ν	39
3.3	The Library of Models	43
3.4	Method	44
4	Chemical evolution of the thin disc	46
4.1	Previous analyses of the Milky Way thin and thick discs	46
4.2	Model constraints for the thin disc	48
4.2.1	MTW yields	48
4.2.2	KTW yields	49
4.2.3	Rr and Rd yields	49
4.2.4	MLr yields	49
4.3	Predicted Elemental abundances	52
4.3.1	MTW yields	52
4.3.2	KTW yields	53
4.3.3	Rr and Rd yields	53
4.3.4	MLr yields	53
4.4	Conclusions	55
5	Chemical evolution of thick disc	57
5.1	Introduction	57
5.2	Effects of Rotation	60
5.3	Effects of a top heavy IMF	63
5.4	Conclusions	68
6	The impact of PISNe in the chemical evolution of extremely metal-poor galaxies	70
6.1	Introduction	70
6.2	Chemical evolution model and stellar ejecta	72
6.3	Observational data	73
6.4	Results	74
6.5	Conclusions	82
7	Effect of IMF on the evolution of CNO elements	84
7.1	Introduction	84
7.2	Effect of IMF on (C/O) and (N/O) ratios	86
7.2.1	Slope $x=1.7$	86
7.2.2	Slope $x=1.5$	86
7.2.3	Slope $x=1.3$	88
7.2.4	Slope $x=0.8$	88
7.2.5	N/O ratio	88
7.3	Conclusions	91
8	Summary and Future prospects	92
8.1	Summary	92
8.2	Future Prospects	97

A	Tables of chemical ejecta	98
B	Chemical and high-z galaxy evolution	101
B.1	Merging Rates of Binary Compact Objects in Galaxies: Perspectives for Gravitational Wave Detections	101
B.2	New Analytic Solutions for Galaxy Evolution: Gas, Stars, Metals, and Dust in Local ETGs and Their High-z Star-forming Progenitors	104
	Bibliography	110

List of Tables

2.1	Description of the main quantities used in this thesis.	11
3.1	The values of the four parameters for our initial exploration of chemical evolution models. The first row shows the reference values that have been kept fixed when varying the other parameters. . .	37
3.2	Sets of chemical ejecta adopted in the chemical evolution models . .	43
3.3	The different values of the chemical evolution input parameters adopted in this work	44
4.1	Parameters for the best model for each ejecta combination as given in Table. 3.2 and defined in Sect. 3.3.	55
5.1	Adopted parameters for the thick disc models	58
6.1	Input parameters of the selected models.	73
7.1	Chemical evolution parameters of the test model.	86
A.1	An example of a table containing the total ejecta, $E_j = E_j^w + E_j^{sn}$ (in M_\odot , see Sect. 2.2.2), of massive and very massive stars used in this thesis (extracted from the set MTW), for $Z_i = 0.02$ and a few selected chemical species. The complete tables, available online, include more nuclides, from H to Zn.	100

List of Figures

2.1	Pre-SN mass M_{fin} as function of initial M_i for different values of the initial metallicity Z_i , as indicated. Stellar tracks are taken from PARSEC VI.1 models.	10
2.2	M_{HE} (top panel) and M_{CO} (bottom panel) as a function of M_i , for different values of Z_i . Lines show the data extracted from PARSEC stellar evolution models, while crosses represent the models of Chieffi & Limongi (2004)	15
2.3	PISN Ejecta from Woosley et al. (2002) and (Kozyreva et al. 2014b), as labelled in the figure.	19
2.4	The He core mass, M_{HE} , as a function of the initial mass. M_i , for different values of the metallicity Z_i in PARSEC stellar evolution models. Crosses represent the models of Chieffi & Limongi (2004)	20
2.5	Final fate of massive and very massive stars as a function of M_i and Z_i . Green dot is a successful SN, from ECSN if the background is light green or CCSN if it is yellow; red dot is a BH from a failed CCSN; red dot in a black box is a BH from PPISN; yellow star is a thermonuclear explosion from PISN and black dot is a DBH.	21
2.6	Fractional wind ejecta, W_j , derived from PARSEC stellar models, as a function of M_i and Z_i . The chemical species shown are ^4He , ^{12}C , ^{14}N , ^{16}O , ^{20}Ne , ^{24}Mg , ^{28}Si , S, Ar, Ca, Ti, Fe.	25
2.7	Fractional total ejecta (winds and explosion) of new production, P_j , for $Z_i = 0.0001$ as a function of M_i . Our MTW ejecta are compared with those of other literature works. The chemical species shown are ^4He , ^{12}C , ^{14}N , ^{16}O , ^{20}Ne , ^{24}Mg , ^{28}Si , S, Ar, Ca, Ti, Fe.	26
2.8	The same as in Fig. 2.7 but for $Z_i = 0.001$	27
2.9	The same as in Fig. 2.7 but for $Z_i = 0.006$. Note that the LC18 ejecta for this metallicity are interpolated.	28
2.10	The same as in Fig. 2.7 but for $Z_i = 0.02$	29
3.1	Simple star formation with no second episode	31
3.2	Complex star formation with constant second episode	31
3.3	Complex star formation with Schimdt type second episode	32
3.4	The $[\text{X}/\text{Fe}]$ vs. $[\text{Fe}/\text{H}]$ evolution of the four elements O, Mg, Si, Ca. The data has been taken from Bensby et al. (2014) . The thin disc stars are shown in blue whereas the thick disc stars are shown in magenta.	35

3.5	The effect of changing the k_{sch} on the chemical evolution. The models have been run for three values of $k_{sch} = 0.5, 1.0, 1.5$ depicted by the blue, red and green lines respectively. The other three parameters have been kept fixed to their reference values. The first four panels, from upper left to lower right show, respectively, the evolution of the SFR [M_{\odot}/yr], gas fraction, SNII and SNIa rates per century and total gas metallicity. The vertical bars plotted at an age of 13 Gyr show their current estimated values, which will be discussed in more detail later. The solid triangle in the metallicity panel marks the initial value of the solar metallicity, resulting from the PARSEC calibration. The bottom panels show the run of the abundances ratios [O/Fe] [Mg/Fe] against [Fe/H]. In these panels, the data are the same of those plotted in Fig. 3.4.	38
3.6	Same as Fig. 3.5 but changing the infall timescale here for the values $\tau_{inf} = 2.0, 5.0, 10$ Gyr and keeping the other parameters fixed to their reference values.	40
3.7	Same as Fig. 3.5 but varying the parameter ASNIa. We explore here $ASNIa = 0.02, 0.05, 0.09$, keeping the other three parameters fixed to their reference values.	41
3.8	Same as Fig. 3.5 but changing the parameter that regulates the efficiency of star formation, ν . Values of $\nu = 0.2, 0.5, 1.0$ are explored here, keeping the other parameters fixed to their reference values.	42
4.1	From upper left to lower right we show the evolution of the SFR [M_{\odot}/yr], gas fraction, SNII and SNIa rates per century and total gas metallicity of the best models computed using the MTW, KTW, Rr, Rd and MLr sets of yields. Vertical bars at an age of 13Gyr show their current estimated values. The solid triangle in the lower right panel marks the initial value of the solar metallicity resulting from the PARSEC calibration. The chemical evolution parameters of the models are listed in Table. 4.1	50
4.2	Observed [Fe/H] distribution of thin disc stars (solid brown) and thick disc stars (dotted yellow). Superimposed are selected model of the thin disc for the cases MTW (blue). Vertical lines mark the median values of the distributions	51
4.3	Comparison of the best models of Fig. 4.1 with selected observations of stars of the thin disc in the solar neighbourhood Bensby et al. (2014) (blue points). Also plotted are data of thick disc stars from the same author (magenta points). Grey dots represent a sample of metal-poor halo stars (Gratton & Sneden 1988 ; McWilliam et al. 1995 ; Fulbright 2000 ; Carretta et al. 2002 ; Cayrel et al. 2003).	54

5.1	Observed [Fe/H] distribution of thin disc stars (solid yellow) and thick disc stars (dotted brown). Superimposed is a selected model of the thick disc for the case MTW with $M_{\text{UP}} = 120 M_{\odot}$ and $\chi = 1.5$ (blue). Vertical lines mark the median values of the corresponding distributions.	59
5.2	Comparison of the observed [O/Fe] and [Mg/Fe] and vs. [Fe/H] ratios of the thick disc (magenta dots) with those predicted model TD1.	60
5.3	[O/Fe] vs. [Fe/H] abundances predicted by massive star models without and with rotation. The blue, orange and green lines refer to Limongi & Chieffi (2018) yields for initial rotational velocities $V_{\text{rot}}=0$, $V_{\text{rot}}=150$ and $V_{\text{rot}}=300$ km/s, respectively. The cyan line represents the MLr model with rotation-averaged yields.	62
5.4	Observed [Fe/H] distribution of thin disc stars (dotted brown) and thick disc stars (solid yellow). Superimposed are the model of the thick disc with MTW yields computed with $M_{\text{UP}} = 200 M_{\odot}$ and $\chi = 1.4$ (red). Vertical lines mark the median values of the distributions	64
5.5	Comparison of the observed [O/Fe] vs. [Fe/H] ratios of the thick disc (magenta dots) with those predicted by models with different IMF parameters of Table ???. We see that increasing M_{UP} , so as to include the contributions of VMO (winds, PPISN and PISN), thick disc stars can be reproduced pretty well. Moreover, changing both the IMF slope and M_{UP} , different populations can be recovered.	66
5.6	Same as in Fig. 5.5, but for [Mg/Fe].	67
6.1	Evolution of Fe/O as a function of metallicity, (O/H) for the models of Table. 6.1. EMPGs from Kojima et al. (2020a) are shown numbered from 1-9, Object 10 an EMPG from Izotov et al. (2018a) . Blue and magenta dots represent thin and thick disc stars from Bensby et al. (2014) , respectively. Gray dots are low metallicity stars from Cayrel et al. (2004) . The dotted lines in M1 and M2 correspond to the fits to thin and thick discs obtained previous chapters. The five squares on the models from left to right are the ages at 30 Myr, 60 Myr, 0.1 Gyr, 0.3 Gyr and 0.6 Gyr respectively.	75
6.2	Normalized O yields, P_{O} , for massive and very massive stars from MTW yield combination. $P_j = [E_j(M_i) - (M_i - M_{\text{rem}}) X_{j,0}] / M_i$ where M_i , M_{rem} , $E_j(M_i)$ and, $X_{j,0}$ are, respectively, the initial and the remnant masses, the total ejecta and the initial stellar abundance (in mass fraction) of the element j	78
6.3	Same as Figure 6.2, but for Fe	79
6.4	The evolution of EMPGs star formation rates as a function the metallicity, (O/H). Symbols and models are the same of Fig. 6.1.	80
6.5	The evolution of the EMPGs stellar masses as a function the metallicity, (O/H). Symbols and models are the same of Fig. 6.1.	81

7.1	(C/O) evolution (left panel) and (N/O) evolution (right panel). Data are taken from Akerman et al. (2004) ; Spite et al. (2005) for (C/O) ratio, the N/O ratio the data is taken from Israelian et al. (2004) ; Roederer et al. (2014) ; Suárez-Andrés et al. (2016) ; Spite et al. (2005) as detailed in the text. The slope of the IMF is $x = 1.7$, and the different models show the effect of varying the upper mass limit of the IMF.	87
7.2	Same as Fig. 7.1 but with the slope of IMF of $x=1.5$	87
7.3	Same as Fig. 7.1 but with the slope of IMF of $x=1.3$	88
7.4	Same as Fig. 7.1 but with the slope of IMF of $x = 0.8$	89
7.5	The N/O ratio predicted by a model with yields from Limongi & Chieffi (2018) , which include rotation. The data are the same as in Fig. 7.1.	90
B.1	Left panel: Compact remnant mass as a function of the zero-age main sequence star mass at different metallicities $Z = 0.01 Z_{\odot}$ (blue lines), $0.03 Z_{\odot}$ (cyan lines), $0.05 Z_{\odot}$ (green lines), $0.1 Z_{\odot}$ (magenta lines), $0.3 Z_{\odot}$ (yellow lines), $0.5 Z_{\odot}$ (orange lines), Z_{\odot} (brown lines), $2 Z_{\odot}$ (saddle brown lines). Solid lines illustrates the relation $m_{\bullet}(m_{*};Z)$ by Spera & Mapelli (2017) for single stellar evolution, based on the delayed SN engine and including (P)PSNe. We have adopted a compact mass remnant distribution $dp = d\log m_{\bullet}$ with a log-normal shape centered around this relation and with a $1-\sigma$ dispersion of 0.1 dex (illustrated by the shaded areas). Right panel: Compact remnants birthrate $R_{birth}(\log m_{\bullet}; z)$ at different redshift $z \sim 0$ (solid lines), 3 (dashed line), and 6 (dotted line). Green lines refer to the approach based on the cosmic SFR density and cosmic metallicity, while black lines refer to our computation taking into account redshift-dependent galaxy statistics and the star formation and chemical enrichment histories of individual galaxies (blue lines refer to disk-dominated galaxies at $z \lesssim 2$).	102
B.2	Left panel: Top panel: merging rate density of compact binaries $R_{merg}(z)$ as a function of redshift. Solid lines refer to BH-BH, dashed lines to NS-NS and dotted lines to BH-NS events. Color-code as in Fig. 4. The cyan and orange shaded areas illustrate the local BH-BH and NS-NS merging rates estimated by LIGO in the O2 run, respectively. Bottom panels: merging rate $R_{merg}(M_{\bullet\bullet}; z)$ as a function of the chirp mass at redshift $z \sim 0$ (left), 3 (middle), and 6 (right). Right panel: GW event rate per unit redshift expected for the AdvLIGO/Virgo (top panel) and ET (bottom panel) with SNR threshold $\rho \gtrsim 8$. Linestyles and color-code as in Fig. 4. The orange lines refer to galaxy-scale gravitational lensing of GWs with magnification $\mu \gtrsim 10$	103

- B.3 Left panel: Star formation efficiency $f_* = M_*/f_b M_H$ vs. stellar mass M_* at different observation redshifts $z \approx 0$ (red), 2 (orange), 4 (cyan), and 6 (blue); the shaded areas illustrate the 1 variance associated with the average over different formation redshifts. Data points are from [Mandelbaum et al. \(2016, circles\)](#), [Hudson et al. \(2015, hexagons\)](#), and [Velandar et al. \(2014, squares\)](#) via weak lensing; [Rodríguez & Rubin \(2005, triangles\)](#) via subhalo abundance matching; [Wojtak & Mamon \(2013, diamonds\)](#) and [More et al. \(2011, pentagons\)](#) via satellite kinematics; [Kravtsov et al. \(2018, pacmans\)](#) via X-ray observations of BCGs; and [Burkert et al. \(2016, crosses\)](#) via mass profile modeling of galaxies at $z \sim 1-2$. If not explicitly indicated, error bars are ≈ 0.25 dex. Right panel: The SFR vs. stellar mass M_* , alias the MS of star-forming galaxies, at different observation redshifts $z \approx 2$ (orange), 4 (cyan), and 6 (blue); the shaded areas illustrate the 1 variance associated with the average over different formation redshifts. The black filled stars are the observational determinations of the MS at $z \sim 2$ based on the statistics of large mass-selected samples by [Rodighiero et al. \(2015\)](#). The other symbols (error bars omitted for clarity) refer to far-IR data for individual objects at $z \sim 1-4$ (those in the range $z \sim 1.5-2.5$ are marked with a dot) by [Dunlop et al. \(2017, triangles\)](#), [Koprowski et al. \(2016, diamonds\)](#), [Ma et al. \(2016, pentagons\)](#), [Negrello et al. \(2014\)](#); [Dye et al. \(2015, circles\)](#) and [da Cunha et al. \(2015, squares\)](#); for reference, the determination at $z \approx 0$ by [Popesso et al. \(2019, crosses\)](#) is also reported. 107
- B.4 Left panel: Gas metallicity Z_{gas} vs. stellar mass M_* at different observation redshifts, $z \approx 2$ (orange), 4 (cyan), and 6 (blue); the shaded areas illustrate the 1σ variance associated with the average over different formation redshifts. Data points are from [de los Reyes et al. \(2015, circles\)](#) at $z \sim 1$, [Suzuki et al. \(2017, triangles\)](#) at $z \sim 3$, and [Onodera et al. \(2016, squares\)](#) at $z \sim 3-4$. All gas metallicities have been converted to PP04O3N2 calibration. Right panel: Stellar metallicity Z_* vs. stellar mass M_* at different observation redshifts, $z \approx 0$ (red), 2 (orange), and 4 (cyan); the shaded areas illustrate the 1 variance associated with the average over different formation redshifts. Data for SDSS samples of local ETGs are from [Thomas et al. \(2010, solid contours\)](#) solid contours, and data for individual galaxies at $z \sim 0.7$ are from [Gallazzi et al. \(2014, triangles\)](#). Inset: as above for α -element-to-iron abundance ratio $[\alpha/Fe]$ vs. stellar mass M_* at observation redshift $z \approx 0$ (red). . . . 108

List of Abbreviations

AGB	A symptotic G iant B ranch
BSG	B lue S uper G iants
CCSN	C ore C ollapse S uper N ovae
CNO	C arbon N itrogen O xygen
DBH	D irect collapse to B lack H ole
DTD	D elay T ime D istribution
ECSN	E lectron C apture S uper N ovae
EMPG	E xtrremely M etal P oor G alaxy
EMPRESS	E xtrremely M etal- P oor R epresentatives E xplored by the S ubaru S urvey
ETG	E arly T ype G alaxy
GALAH	G ALactic A rcheology with H ERMES
GCE	G alactic C hemical E volution
GW	G ravitational W ave
HSC	H yper S uprime- C am
IMF	I nitial M ass F unction
ISM	I nterstellar M edium
JWST	J ames W ebb S pace T elescope
KLr	K arakas et al. 2010 + L imongi et al. 2018 R otating
KTW	K arakas et al. 2010 + T his W ork
LBV	L uminous B lue V ariables
LIMS	L ow-and I ntermediate- M ass S tar
MDF	M etallicity D istribution F unction
MLnr	M arigo et al. 2020 + L imongi et al. 2018 N on R otating
MLr	M arigo et al. 2020 + L imongi et al. 2018 R otating
MS	M ain S equence
MTW	M arigo et al. 2020 + T his W ork
MW	M ilky W ay
OPAL	O paCity P roject A t L ivermore
PARSEC	P Aдова and T Rieste S tellar E volution C ode
PISN	P air I nstability S uper N ovae
PPISN	P ulsational P air I nstability S uper N ovae
RGB	R ed G iant B ranch
SFE	S tar F ormation E fficiency
SFR	S tar F ormation R ate
SN	S uper N ovae
SNIa	S uper N ovae T ype I a
SNIi	S uper N ovae T ype I i

TP-AGB	T hermally P ulsating A symptotic G iant B ranch
VMO	V ery M assive O bjects
WC	W olf-Rayet stars enriched in C arbon
WD	W hite D warf
WN	W olf-Rayet stars enriched in N itrogen
WO	W olf-Rayet stars enriched in O xxygen

*Dedicated to everyone who lost their lives and
livelihoods during this pandemic...*

Chapter 1

Introduction

The chemical evolution of the Milky Way is one of the most important astrophysical topics because it provides direct hints on the more general question of how galaxies formed and evolved. It is also an anchor for galaxy models because of the possibility to study their properties through the analysis of individual stars. Indeed this field of research is continuously growing providing, on one side, an increasing amount of observational abundance data that contribute to enlarge and sharpen the whole picture (e.g. [Gilmore et al. 2012](#); [Bensby et al. 2014](#); [Majewski et al. 2017](#); [de Laverny et al. 2013](#)) and, on the other, a growing number of interpretative tools that go from simple chemical evolutionary models to more complex chemo-hydrodynamical models (e.g. [Valentini et al. 2019](#)).

A key ingredient to interface model predictions with observations are the stellar chemical yields, describing the contribution of stars of different types to the metal enrichment of the galaxies. Other physical processes play of course an important role in the chemical evolution of the galaxies, like the functional forms adopted to describe the stellar birthrate function, of the gas inflows and outflows, the mixing of newly ejected elements with the surrounding medium, the relative displacement of individual stars from their original positions, etc. However stellar yields keep a key role because, being the result of the evolution of stars, they may provide a tight link between stellar and galactic time-scales. The contribution of individual stars to the metal enrichment has been the subject of many studies in the past (e.g. [Matteucci 2014](#), for a thorough review). The chemical enrichment from stars takes place when elements newly produced by nuclear reactions in the deep stellar interiors are ejected into the interstellar medium, via stellar winds or supernova explosions. At this point, it is important to briefly recall the different stellar populations in the MW and their main characteristics which we refer to in the next sections.

1.1 Stellar populations

The different kinds of stellar populations that exist are broadly classified in three groups: Population III, Population II and Population I. Population III stars are considered to be one of the first stars with negligible or very low metal content. These stars have not yet been observed, so the common idea is that they were massive stars and hence the timescales for which they lived were short. Pop II stars

are low metallicity and old stars. Globular cluster stars belong to this population. Population I stars are metal-rich stars and are mostly stars which belong to the thin disc of the MW. However, with the advancement of our knowledge of the MW, a more detailed classification has been performed:

- Halo: The halo consists generally of old and metal-poor stars, with $[\text{Fe}/\text{H}] < -1.0$.
- Thick disc: stars in the thick disc are characterized by high $[\alpha/\text{Fe}]$ ratios and old and intermediate ages. Their metallicities are in the range $-1.0 < [\text{Fe}/\text{H}] < -0.6$.
- Thin disc: such stars have high metallicities, $-0.6 < [\text{Fe}/\text{H}] < 0.5$. These are relatively younger stars and there is even active star formation going on in these regions. $[\alpha/\text{Fe}]$ ratios are generally lower than thick stars, however, there is some overlap between the two populations. Also, some old, high $[\alpha/\text{Fe}]$ stars do exist locally with high $[\text{Fe}/\text{H}]$ that point to non-negligible effects of stellar radial migration (e.g. [Anders et al. 2017](#), and refs therein)
- Bulge: Bulge is the central part of the MW and it contains stars belonging to a large variety of metallicities. Although it consists of old stars, the metallicities are in the range $-1.0 < [\text{Fe}/\text{H}] < 1.0$.

I recall here that, one of the ways to define the stellar metallicity is using $[\text{Fe}/\text{H}]$, the iron content of the stars. We follow the standard notation for abundances, i.e.:

$$[X/Y] = \log_{10} \left(\frac{N_x}{N_y} \right)_{star} - \log_{10} \left(\frac{N_x}{N_y} \right)_{\odot} \quad (1.1)$$

where N_x and N_y are the number of atoms for elements x and y per unit volume and the suffix star refer to the ratio measured in the star, while the Sun symbol denotes the reference solar abundances.

1.2 Stellar mass ranges

The contribution of stars to the chemical enrichment of galaxies is mostly driven by their initial masses.

Low- and intermediate-mass stars, $M_i \simeq 0.8 M_{\odot} - 7 M_{\odot}$, never reach the carbon ignition temperature and enrich the interstellar medium (ISM) mainly during the Red Giant Branch (RGB) and Asymptotic Giant Branch (AGB) phases ([Marigo 2001](#); [Cristallo et al. 2009, 2011, 2015](#); [Karakas 2010](#); [Karakas & Lugaro 2016](#); [Karakas et al. 2018](#); [Ventura et al. 2013, 2017, 2018](#); [Pignatari et al. 2016](#); [Slemer et al. 2017](#); [Ritter et al. 2018](#), and references therein).

Stars in a narrow mass interval, $M_i \simeq 7 M_{\odot} - 10 M_{\odot}$, are able to burn carbon in their non- or mildly degenerate cores and experience the so-called Super-AGB phase ([Ritossa et al. 1996](#); [García-Berro et al. 1997](#); [Iben et al. 1997](#)). Depending

on the efficiency of stellar winds and the growth of the core mass, the final fate of Super-AGB stars splits in two channels that lead either to the formation of an O-Ne-Mg white dwarf ($7 \lesssim M_i/M_\odot \lesssim 9$) or to an electron-capture supernova ($9 \lesssim M_i/M_\odot \lesssim 10$; Hurley et al. 2000; Siess 2007; Poelarends et al. 2008).

Massive stars ($M_i \approx 10 - 120 M_\odot$) experience more advanced nuclear burnings (Ne, O, Si) up to the formation of an iron core, that eventually implodes producing either a successful core-collapse supernova (CCSN) explosion, or the direct collapse into a black hole as a *failed* SN (Woosley & Weaver 1995; Fryer 1999; Chieffi & Limongi 2004; Limongi & Chieffi 2006; Nomoto et al. 2006; Fryer et al. 2006; Fryer & Kalogera 2001; Heger & Woosley 2002; Heger et al. 2003a; Fryer et al. 2012; Janka 2012; Ugliano et al. 2012; Ertl et al. 2016; Pignatari et al. 2016; Ritter et al. 2018; Limongi & Chieffi 2018).

Very massive objects (VMO), $100 \lesssim M_i/M_\odot \lesssim 300 M_\odot$, enter the pair instability regime during central oxygen burning, which may trigger their final thermonuclear explosion (Heger & Woosley 2002; Umeda & Nomoto 2002; Kozyreva et al. 2014c; Woosley & Heger 2015; Woosley 2017).

The chemical ejecta contributed by all stars of different initial masses and evolutionary stages are key ingredients of galactic chemical evolution studies. In most cases, the adopted stellar IMF is truncated at around $M_i \approx 100 M_\odot$, which implies that no chemical contribution from VMO is taken into account. This common assumption is due to the fact that very few evolutionary models exist for stars with $M_i > 100 M_\odot$. With the exception of zero-metallicity stars (e.g., Haemmerlé et al. 2018; Yoon et al. 2012; Ohkubo et al. 2009, 2006; Lawlor et al. 2008; Marigo et al. 2003, 2001), the lack of systematic evolutionary studies of VMO has effectively limited the exploration area of chemical evolution models, which focussed on the role of population III stars only (e.g., Cherchneff & Dwek 2010, 2009; Rollinde et al. 2009; Ballero et al. 2006; Matteucci & Pipino 2005; Ricotti & Ostriker 2004). In fact, the occurrence of VMO and their final fates were thought to apply only to primordial population III stellar populations (Bond et al. 1982, 1984; Heger & Woosley 2002; Nomoto et al. 2013).

1.3 Stellar IMF

The stellar initial mass function (IMF) describes the distribution of stellar masses at their birth. It is usually defined as a power law:

$$\phi(M_i) = \frac{dn}{d\log(M_i)} \propto M_i^{-x}. \quad (1.2)$$

where x is the slope of the IMF in mass ($x = 1.35$ for the Salpeter IMF). Different observational estimates of the IMF in the MW have been proposed, with less massive stars with respect to a simple extrapolation of the Salpeter (1955) law (e.g. Kroupa 1993), or with less abundant low-mass stars (e.g. Chabrier 2003). The mass limit of the IMF is usually taken within the range $0.1 - 100 M_\odot$.

In recent years our understanding of the evolution of massive and very massive stars has dramatically changed as a result of important discoveries. We can now rely on studies focussed on young super star clusters (Evans et al. 2010; Walborn et al. 2014; Schneider et al. 2018; Crowther 2019; Crowther et al. 2016) and on the identification of massive stellar black holes hosted in binary systems (Abbott et al. 2016; Abbott et al. 2020; Spera & Mapelli 2017; Spera et al. 2015). This piece of evidence points to an IMF that extends up to VMO either as an original top-heavy IMF or by virtue of early efficient merging in binary systems (Senchyna et al. 2020).

In summary, nowadays there is strong evidence supporting the existence of stars with initial mass up to $M_i \simeq 350 M_\odot$. Consistently with this scenario, recent theoretical studies on the evolution of VMO (Langer et al. 2007; Kozyreva et al. 2014c; Slemer 2016) pointed out that suitable physical conditions for the occurrence of pair instability events are present not only in primordial zero-metallicity stars, but cover a wider metallicity range, up to $\approx Z_\odot/3$.

Parallel to these studies, Bressan et al. carried out the first systematic analysis of stellar models for massive stars and VMO, extending up to $M_i = 350 M_\odot$, for a large grid of initial metallicity, from $Z_i = 0.0001$ to $Z_i = 0.06$ (Tang et al. 2014; Chen et al. 2015; Costa et al. 2020a). These models, computed with the PARSEC code, are based on updated input physics and, above all, rely on the most recent advances in the theory of stellar winds, which critically affect the evolution of massive stars and VMO.

Metal-poor galaxies or stars provide us with an enormous opportunity to probe the early universe and understand the chemistry at that epoch. Such galaxies, could help us understand the star formation going on at early times, which will prove to be a great deal for Galaxy formation and evolution studies. Such galaxies are believed to be made from Pop III stars which are massive stars mostly metal free and having a high specific star formation rates. Recently there have been observations (Kojima et al. 2020a) that show signatures of contribution from massive stars in their chemical enrichment. This further provides us with an possibility to understand and explore the contribution of massive and super massive stars in chemical evolution of galaxies.

1.4 This thesis

The structure of the thesis is as follows.

In Chapter. 2, I shortly summarize the basics of chemical evolution theory, of stellar classification and of the relevant mass limits, and of how the chemical ejecta of massive stars have been calculated. Also in this chapter, our new set of chemical ejecta for massive and very massive stars are presented. After an outline of the PARSEC code, I describe the method adopted to combine PARSEC stellar

evolution models of massive stars with explosive models available in the literature. Then I discuss the resulting ejecta due to both stellar winds and explosions (CCSN, PPISN, and PISN). Sect. 2.3 summarizes the main characteristics of the AGB yields obtained with the COLIBRI code. Sect. 2.4 introduces and compares various sets of chemical ejecta for AGB and massive stars taken from the recent literature.

In Chapter. 3 I describe our one-zone chemical evolution code, the role of its parameters in the output star formation and abundance ratios histories, the generation of the grid of models we then use to search for best fit models to interpret observed abundances. We describe also the choice of the data of the MW we take as a reference for our next chapters.

In Chapters 4 and 5, I analyse the predictions of chemical evolution models calculated adopting the different sets of chemical ejecta under consideration. Their performance is tested through the use of various diagnostics, with particular focus on the observed $[O/Fe]$ vs. $[Fe/H]$ diagram populated by thin- and thick disc stars. We have performed a thorough analysis and interpretation of the MW data for the thin and the thick disk in terms of star formation history, variation of the IMF slope and upper mass limit, and accounting for the vast range of different input ejecta discussed in Chapter. 2.

In Chapter. 6, we have investigated the origin of the peculiar abundance ratios of a sample of well observed nearby extremely metal-poor galaxies. We exploit our extensive tables of stellar ejecta to test the possibility that the extremely large Fe/O ratios measured in these galaxies may be the signature of the distinctive ejecta from PISN, and therefore also of a top-heavy IMF at low metallicities. Along the same line of testing non-standard IMF via abundance ratios, in Chapter. 7 I discuss a work in progress that aims at studying the evolution of the CNO elements and how the IMF affects the evolution of their relative ratios.

Chapter. B, I discuss briefly the summaries of two studies I have been part of during my PhD , one related to merging of compact binaries and the other about analytical solution for the evolution of the gas/stellar mass and metal content in a star-forming galaxies.

Chapter. 8 recaps the studies and its main conclusions.

Most of the work in Chapters 2 to 5 is included in the paper Goswami et al. (2020a), A&A, submitted. Chapter. 6 will be presented in a paper in preparation (Goswami et al. 2020b). Chapter. B summarizes the work presented in the papers Pantoni et al. (2019) and Boco et al. (2019).

Chapter 2

Chemical evolution and stellar ejecta

During the big bang, only light elements were formed. Heavier elements are products of stellar nucleosynthesis. Some light elements, such as Li, Be, and B, may be formed by the spallation processes, which are collision between cosmic rays and C, N, O atoms present in the interstellar medium. The stars are born, live, and die, and they can die in a quiescent fashion like white dwarfs or violently as supernovae.

We briefly summarize below the ingredients for modelling chemical evolution, and we refer to [Matteucci \(2002, 2016\)](#) for comprehensive reviews.

- Stellar birthrate function: this is the history of star formation in a galaxy, and it can be expressed as the product of the star formation rate (SFR) and the IMF.
- Stellar nucleosynthesis: Stellar yields are defined as the masses of chemical elements produced by stars of different masses. Here we summarize the element production in stars briefly: i) low and intermediate mass stars ($0.8 - 8M_{\odot}$) produce He, N, C, and heavy s-process elements. They die as C-O white dwarfs, when single, and can die as Type Ia SNe when binaries. ii) Stars with $M < 0.8M_{\odot}$ do not contribute to galactic chemical enrichment and have lifetimes longer than the Hubble time. iii) Massive stars ($M > 8 - 10M_{\odot}$) produce mainly α -elements (O, Ne, Mg, S, Si, Ca), some Fe, light s-process elements, some r-process elements and explode as core-collapse SNe. The stellar yields used in my work will be discussed in detail in later sections.
- Assumptions on gas flows in and/or out of the system

With these ingredients, the following quantities can be computed.

The yield per stellar generation is defined as:

$$y_i = \frac{\int_1^{\infty} m p_{im} \phi(m) dm}{(1 - R)} \quad (2.1)$$

where p_{im} is the mass of the newly produced element i ejected by a star of mass m , and R is the returned fraction:

$$R = \int_1^{\infty} (m - M_{rem}) \phi(m) dm \quad (2.2)$$

The yield y_i is, therefore, the mass fraction of the element i newly produced by a generation of stars relative to the fraction of mass in remnants (white dwarfs, neutron stars, and black holes) and never dying low mass stars.

The stellar yield p_{zm} is just the difference between what is ejected and what was initially present. It is the sum of the wind and supernova contributions.

$$p_{zm} = p_{zm}^{wind} + p_{zm}^{SN} \quad (2.3)$$

with

$$mp_{zm}^{wind} = \int_0^{\tau(m)} \dot{M}(m,t) [Z_s(t) - Z_0] dt \quad (2.4)$$

$$mp_{zm}^{SN} = \int_{remnant}^{m(\tau)} [Z(m') - Z_0] dm' \quad (2.5)$$

where $\dot{M}, Z_s, Z(m'), Z_0, \tau$ and $m(\tau)$ are the mass loss rates, the mass fraction of the element Z at the surface, the mass fraction of element Z at the mass level m' in the star, the initial mass fraction of element Z , the age of the star and the remaining mass at age τ .

Under the closed box model assumption, i.e. the system evolves in isolation with no gas inflows or outflows, the equation for the evolution of the gas metallicity reads:

$$\frac{d(ZM_{gas})}{dt} = -Z\psi(t) + \int_{m(t)}^{\infty} [(m - M_R)Z(t - \tau_m) + mp_{zm}] \psi(t - \tau_m) \phi(m) dm \quad (2.6)$$

where the first term in the square brackets represents the mass of pristine metals which are restored into the ISM without suffering any nuclear processing, whereas the second term contains the newly formed and ejected metals.

A complete chemical evolution model in the presence of both galactic wind, gas infall, and radial flows can be described by a number of equations equal to the number of chemical species: in particular, if M_i is the mass of the gas in the form of any chemical element i , we can write the following set of integro-differential equations which can be solved only numerically (Matteucci 2012, 2016):

$$\begin{aligned} \dot{M}_i(t) = & -\psi(t)X_i(t) + \int_{M_L}^{M_{Bm}} \psi(t - \tau_m) Q_{mi}(t - \tau_m) \phi(m) dm + \\ & A_b \int_{M_{Bm}}^{M_{BM}} \phi(m) \left[\int_{\mu_{Bmin}}^{0.5} f(\mu_B) \psi(t - \tau_{m2}) Q_{mi}(t - \tau_{m2}) d\mu_B \right] dm + \\ & (1 - A_B) \int_{M_{Bm}}^{M_{BM}} \psi(t - \tau_m) Q_{mi}(t - \tau_m) \phi(m) dm + \\ & \int_{M_{BM}}^{M_U} \psi(t - \tau_m) Q_{mi}(t - \tau_m) \phi(m) dm + X_{iA}(t)A(t) \\ & - X_i(t)W(t) + X_i(t)I(t) \quad (2.7) \end{aligned}$$

where M_i can be substituted by σ_i , namely the surface gas density of the element i . The quantity $X_i(t) = \sigma_i(t) / \sigma_{gas}(t) = M_i(t) / M_{gas}(t)$ represents the abundance by mass of the element i , and by definition, the summation over all the mass abundances of the elements present in the gas mixture is equal to unity. These equations include the products from Type Ia SNe (the third term on the right), the products of stars ending their lives as white dwarfs and core-collapse SNe, and the outflow and inflow terms.

2.1 Stellar classes and mass limits

The final fate of stars depends primarily on their initial mass, M_i , and metallicity, Z_i . To characterize the chemical contributions of stars, it is convenient to group them in classes as a function of M_i , according to evolutionary paths and final fates. Let us introduce a few relevant limiting masses that define each stellar family. Mass limits and other relevant quantities used throughout the thesis are also defined in Table. 2.1.

It should be noticed that the mass ranges specified below should not be considered as strict, but rather approximate limits, since they significantly depend on the efficiency of processes like convective mixing and stellar winds and, especially for massive stars, also on the initial chemical composition.

We define with $M_{AGB} \simeq 6 M_{\odot}$ the maximum initial mass for a star to build a highly electron-degenerate C-O core after the end of the He-burning phase. This class comprises low- and intermediate-mass stars, which then proceed through the AGB phase leaving a C-O WD as a compact remnant.

Stars with $M_i > M_{AGB}$ are able to burn the carbon in mildly or non-degenerate conditions. Those stars that build an electron-degenerate O-Ne-Mg core are predicted to enter the Super-AGB phase, undergoing recurrent He-shell flashes and powerful mass loss, similarly to the canonical AGB phase. If stellar winds are able to strip off the entire H-rich envelope while the core mass is still lower than $\simeq 1.38 M_{\odot}$, then the evolution will end as an O-Ne-Mg WD (Nomoto 1984; Iben et al. 1997). We denote with $M_{SAGB} \simeq 8 M_{\odot}$ the upper mass limit of this class of stars (Herwig 2005; Siess 2006, 2007; Doherty et al. 2014).

Stars with $M_i > M_{SAGB}$ and having an electron-degenerate O-Ne-Mg core that is able to grow in mass up to the critical value of $\simeq 1.38 M_{\odot}$, are expected to explode as electron capture supernovae (ECSN; Nomoto 1984; Poelarends et al. 2008; Leung et al. 2020).

Let us denote with M_{mas} the minimum initial mass for a star to avoid electron degeneracy in the core after carbon burning. We note that following this definition the progenitors of electron capture SN cover the range $M_{SAGB} < M_i < M_{mas}$.

Stars with $M_{mas} \leq M_i < M_{VMO} \simeq 100 M_{\odot}$ are able to proceed through all hydrostatic nuclear stages up to Si-burning, with the formation of a Fe core that eventually undergoes a dynamical collapse triggered by electron-captures and photodisintegrations (Woosley & Weaver 1995; Thielemann et al. 2011).

Very massive stars with $M_i \geq M_{\text{VMO}}$ may experience electron-positron pair creation instabilities before and during oxygen burning, with a final fate that is mainly controlled by the mass of the helium core, M_{HE} (Heger & Woosley 2002; Heger et al. 2003a; Nomoto et al. 2013; Kozyreva et al. 2014c; Woosley 2016, 2017; Leung et al. 2019), resulting in a successful/failed CCSN or thermonuclear explosion. For further details, we refer to Sect. 2.2.6.

2.2 Chemical ejecta of massive and very massive stars using PARSEC models

In this thesis our reference set of evolutionary tracks for massive and very massive stars is taken from the large database of Padova and TRIeste Stellar Evolution Code (PARSEC)^{1, 2}. The PARSEC code is extensively described elsewhere (Bressan et al. 2012; Costa et al. 2019a,b) and here we will provide only a synthetic description of the relevant input physics.

2.2.1 Evolutionary models

The PARSEC database includes stellar models with initial masses from $8 M_{\odot}$ to $350 M_{\odot}$ and metallicity values $Z_i = 0.0005, 0.001, 0.004, 0.006, 0.008, 0.017, 0.02, 0.03$ (Chen et al. 2015; Tang et al. 2014). The adopted reference solar abundances are taken from Caffau et al. (2011), with a present-day solar metallicity $Z_{\odot} = 0.01524$. For all metallicities the initial chemical composition of the models is assumed to be scaled-solar. The isotopes included in the code are: H, D, ^3He , ^4He , ^7Li , ^7Be , $^{12,13}\text{C}$, $^{14,15}\text{N}$, $^{16,17,18}\text{O}$, ^{19}F , $^{20,21,22}\text{Ne}$, ^{23}Na , $^{24,25,26}\text{Mg}$, $^{26,27}\text{Al}$, ^{28}Si . Opacity tables are from Opacity Project At Livermore (OPAL)³ team (Iglesias & Rogers 1996, and references therein) for $4.2 \leq \log(T/\text{K}) \leq 8.7$, and from ÆSOPUS tool⁴ (Marigo & Aringer 2009), for $3.2 \leq \log(T/\text{K}) \leq 4.1$. Conductive opacities are included following Itoh et al. (2008). Neutrino energy losses by electron neutrinos are taken from Munakata et al. (1985), Itoh & Kohyama (1983) and Haft et al. (1994). The equation of state is from FREEEOS⁵ code version 2.2.1 by Alan W. Irwin.

The mass loss prescriptions employed in PARSEC are the law of de Jager et al. (1988) for red super giants (RSG; $T_{\text{eff}} \leq 12000$ K), the Vink et al. (2000) relations for blue super giants (BSG; $T_{\text{eff}} > 12000$ K), and Gräfener (2008) and Vink et al. (2011) during the transition phase from O-type to Luminous Blue Variables (LBV) and RSG, and finally to Wolf Rayet (WR) stars.

¹<https://people.sissa.it/~sbressan/parsec.html>

²<http://stev.oapd.inaf.it/cgi-bin/cmd>

³<http://opalopacity.llnl.gov/>

⁴<http://stev.oapd.inaf.it/aesopus>

⁵<http://freeeos.sourceforge.net/>

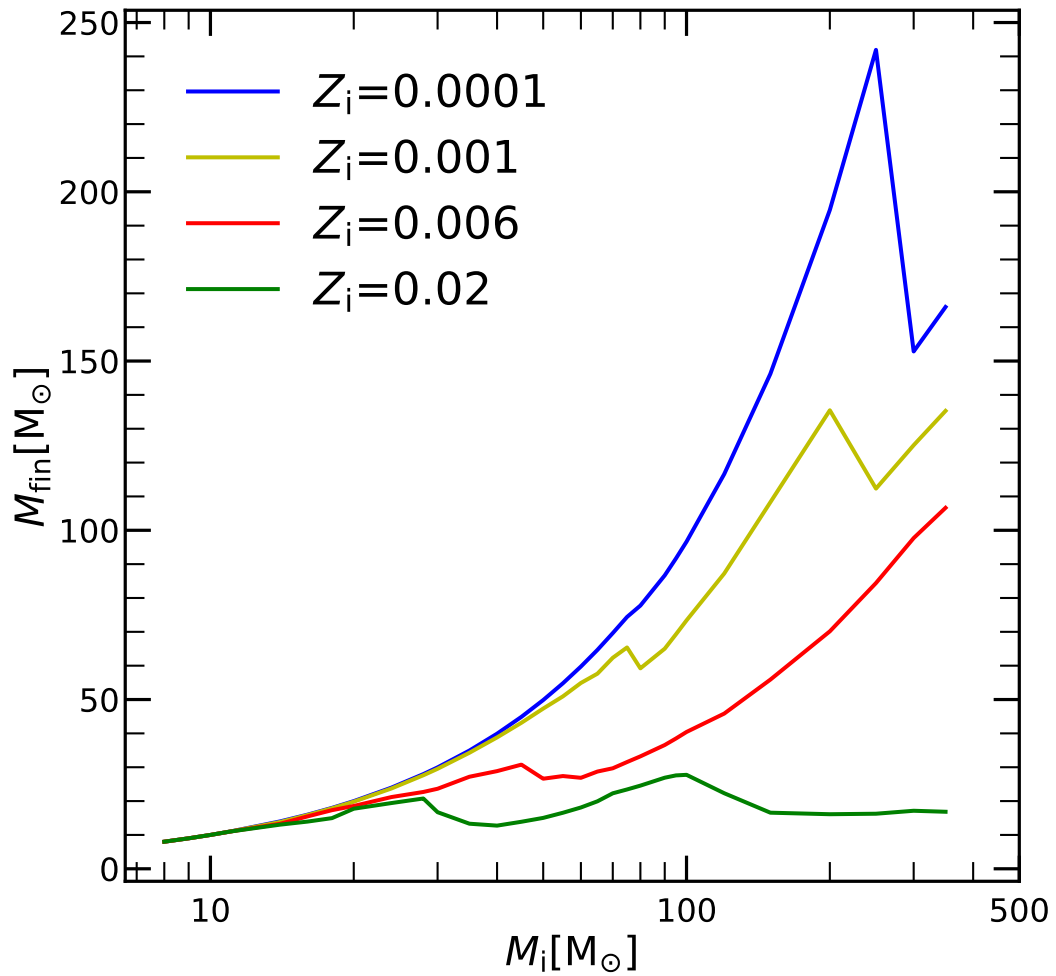


FIGURE 2.1: Pre-SN mass M_{fin} as function of initial M_i for different values of the initial metallicity Z_i , as indicated. Stellar tracks are taken from PARSEC VI.1 models.

TABLE 2.1: Description of the main quantities used in this thesis.

name	definition
Z_i	Initial metallicity.
M_i	Mass of the star at the zero-age main sequence
M_{fin}	Mass of the star at the beginning of central carbon burning (almost equivalent to the pre-SN mass)
M_{rem}	Mass of the remnant
M_{cut}	Mass-cut, in a pre-supernova model, enclosing the entire mass that will collapse and form the compact remnant
M_{He}	Mass of the He-core at the beginning of central carbon burning
M_{CO}	Mass of CO-core at the beginning of central carbon burning
M_{AGB}	Maximum mass for a star to experience the AGB phase and leave a C-O WD
M_{SAGB}	Maximum mass for a star to evolve through the Super-AGB and leave an O-Ne-Mg WD
M_{mas}	Minimum mass for a star to experience all hydrostatic nuclear burnings up to the Si-burning stage, with the formation of an iron core which eventually collapses, leading to either a successful CCSN or a failed SN
M_{VMO}	Mass boundary between massive stars and VMO

2.2.2 Calculation of the chemical ejecta

Since the PARSEC code does not evolve the star up to the pre-supernova stage and beyond, we combine our evolutionary tracks with existing explosive models covering a range of initial masses that corresponds to different final fates (CCSN, failed SN, PPISN and PISN). Following the work by [Slemer \(2016\)](#), for each stellar model of given initial mass M_i we first compute the amount of ejected mass of the element j due to the stellar winds, $E_j^w(M_i)$, and then the contributions of the associated supernova channels, $E_j^{\text{sn}}(M_i)$. The total ejecta $E_j(M_i)$ are given by

$$E_j(M_i) = E_j^w(M_i) + E_j^{\text{sn}}(M_i) \quad (2.8)$$

The complete tables of wind and explosion ejecta for massive and very massive stars ($8 \leq M_i/M_\odot \leq 350$) and four values of the initial metallicity ($0.0001 \leq Z_i \leq 0.02$) are described in Appendix A. They are available online at the URL [xxxx](#).

We consider the most important chemical species and their isotopes from H to Zn. The species explicitly included in PARSEC nuclear networks are all the isotopes from ^1H to ^{28}Si . Heavier elements are present in the initial chemical composition, according to the adopted scaled-solar mixture (see Sect. 2.2), and are not affected by the nuclear reactions and mixing events during the hydrostatic H- and He-burning phases.

In the following, we detail how we calculate the wind and explosion ejecta, $E_j^w(M_i)$ and $E_j^{\text{sn}}(M_i)$, that appear in Eq. 2.8.

2.2.3 Wind ejecta

The wind ejecta of a species j contributed by a star of initial mass M_i is computed with the following equation:

$$E_j^w(M_i) = \int_0^{\tau_C} \dot{M}(M_i, t) X_j^s(t) dt \quad (2.9)$$

where the integral is performed over the stellar lifetime, from the zero age main sequence (ZAMS) up to the stage of carbon ignition, τ_C . For a given M_i the quantities $\dot{M}(M_i, t)$ and $X_j^s(t)$ denote, respectively, the mass-loss rate and surface abundance (in mass fraction) of the species j , at the current time t .

The total amount of mass lost by a star during its hydrostatic evolution, $M_i - M_{\text{fin}}$, can be appreciated from Fig. 2.1, which shows the pre-SN mass (M_{fin}) as a function of M_i , for a few selected values of the initial metallicity.

Fig. 2.6, illustrates the fractional wind ejecta, $E_j^w(M_i)/M_i$, of the main chemical species considered in the PARSEC models, as a function of M_i and Z_i . For $M_i \leq 100 M_\odot$ the wind ejecta generally increase with initial mass and metallicity, which is explained by the strengthening of stellar winds at higher luminosities and larger abundances of metals. This applies to H, He, N, Ne, Na, Mg, Al, and Si.

The metallicity trends for C and O reverse in the case of VMO. Compared to the predictions for $Z_i = 0.02$, at low metallicities and high initial masses, $Z_i \leq$

0.006 and $M_i > 100 - 200 M_\odot$, the wind ejecta may be larger by even one order of magnitude for C and up to two orders of magnitude for O. This result is explained when considering the stage at which stars of different M_i and Z_i enter the WC and WO phases, which are characterized by powerful winds enriched in C and O.

At $Z_i = 0.02$ all VMO experience high mass loss before entering in the WC regime, which is attained close to the end of the He-burning phase. We note that these models are not expected to go through the WO regime. As a consequence, their ejecta are characterized by low amounts of primary C and O. Conversely, at lower metallicities, $Z_i = 0.0001$ and 0.004 , due to the relatively weak stellar winds during the early evolutionary stages, VMO reach the WC and WO regimes with a much larger mass, hence producing higher ejecta of C and O.

2.2.4 Explosion ejecta of electron capture supernovae

To account for the ECSN channel we take advantage of the recent revision of the PARSEC code (Costa et al. 2020a), who extended the sequence of hydrostatic nuclear burnings up to oxygen. In this way, we can check which models develop a degenerate O-Ne-Mg core after the carbon burning phase. As mentioned in Sect. 2.3, we did not follow the Super-AGB phase and the corresponding yields are taken from Ritter et al. (2018) using the models with $M_i = 6 M_\odot$ and $7 M_\odot$.

As to the ECSN channel we proceed as follows. Given the severe uncertainties that affect the definition of the mass range for the occurrence of ECSN (e.g., Doherty et al. 2017; Poelarends et al. 2008) and the modest chemical contribution expected from the explosive nucleosynthesis (e.g., Wanajo et al. 2009), we adopt a simple approach. For each Z_i we look over the mass range $8 \leq M_i/M_\odot \leq 10$, and assign the ECSN channel to the PARSEC models that, after the carbon-burning phase, develops a degenerate core with mass close to the critical value of $1.38 M_\odot$. In the metallicity range under consideration ($0.0001 \leq Z_i \leq 0.02$), this condition is met by PARSEC models with $8 \leq M_i/M_\odot \leq 9$.

The ECSN explosion ejecta are taken from the work of Wanajo et al. (2009, their table 2) using the FP3 model as suggested by the authors. The nucleosynthesis results derive from a neutrino-driven explosion of a collapsing O-Ne-Mg core of mass $= 1.38 M_\odot$, with a stellar progenitor of $M_i = 8.8 M_\odot$ (Nomoto 1984). According to this model, the total mass ejected by the explosion is quite low, $\approx 1.39 \cdot 10^{-2} M_\odot$. This fact, together with the neutron-richness of the ejecta, lead to a modest production of radioactive ^{56}Ni and hence of stable ^{56}Fe ($\approx 0.002 - 0.004 M_\odot$). In addition, the ECSN yields are characterized by a minor production of α -elements (e.g., O and Mg), and an appreciable synthesis of heavier species like ^{64}Zn and some light p-nuclei (e.g., ^{74}Se , ^{78}Kr , ^{84}Sr , and ^{92}Mo). Assuming no fall back during the explosion, the ECSN event is expected to produce a neutron star with mass $M_{\text{rem}} = 1.366 M_\odot$. Finally, we add the ejecta of the layers above M_{rem} with the chemical composition predicted by the corresponding PARSEC model.

We note that the specific ECSN model adopted for each Z_i serves as a bridge between AGB and massive stars, to avoid a coarse mass-interpolation of the ejecta

in the transition region $M_{\text{AGB}} < M_i/M_{\odot} < M_{\text{mas}}$ (see Table 2.1). A more careful consideration of this mass interval is certainly desirable and is postponed to a future study.

2.2.5 Explosion ejecta of core collapse supernovae

Stars in this class have $M_{\text{mas}} < M_i < M_{\text{VMO}}$. The upper limit, M_{VMO} , corresponds to a star that reaches $M_{\text{He}} \sim 32M_{\odot}$ after central He burning and enters the pair-instability regime during O-burning (Woosley 2017), thus avoiding the standard evolutionary path to the silicon burning stage (see Sect. 2.2.6). At solar composition, this mass limit is typically $M_{\text{VMO}} \sim 100M_{\odot}$ but it is expected to vary with metallicity, as it is affected by mass loss during the early evolutionary phases.

Of particular relevance for this mass range is the determination of the explodability of a model, i.e. the conditions that lead to a successful SN or to a failed SN. In recent years there have been many attempts to explore the dependence of the outcome of the supernova collapse on the input physics, with the final goal to possibly determine a relation between the explodability and the main stellar parameters, in particular the initial or pre-supernova mass of the star (Fryer 1999; Fryer et al. 2006; Fryer & Kalogera 2001; Heger & Woosley 2002; Heger et al. 2003a; O'Connor & Ott 2011; Fryer et al. 2012; Janka 2012; Ugliano et al. 2012; Ertl et al. 2016).

We briefly recall that Fryer et al. (2012) provided simple relations of the explodability with the final C-O core mass (M_{CO}), O'Connor & Ott (2011) introduced the compactness criterion as a threshold for the explodability and Ertl et al. (2016) introduced a two-parameter explodability criterion. Fryer et al.'s models depend only on the C-O core mass after carbon burning and on the pre-supernova mass of the star. Instead, the other models predict a non-monotonic behaviour of the explodability with the core mass, with the existence of islands of explodability intermixed with islands of failures.

A related issue concerns the material that may fall back onto the surface of the proto-neutron star after the explosion, leading eventually to the formation of a black hole and possibly also to a failed SN (Fryer et al. 2012).

It is clear that the present theoretical scenario is heterogeneous and there is no unanimous consensus of different authors on the explodability of a massive star following the collapse of its Fe core. This is mainly due to the fact that when the models are near the critical conditions for explosion they become critically sensitive to slight variations in the input micro-physics and numerical treatments (Burrows et al. 2018).

All these facts make it hard to unambiguously set a threshold mass between successful and failed explosions. However, since indications exist that a reasonable limit could be in the range $25M_{\odot} \lesssim M_i \lesssim 30M_{\odot}$ (e.g. O'Connor & Ott 2011; Sukhbold et al. 2016), we assume that massive stars with $M_i \geq 30M_{\odot}$ will fail to explode.

The other important parameter needed to obtain the ejecta is the remnant mass, M_{rem} . To derive this quantity one could use the observed relation between the

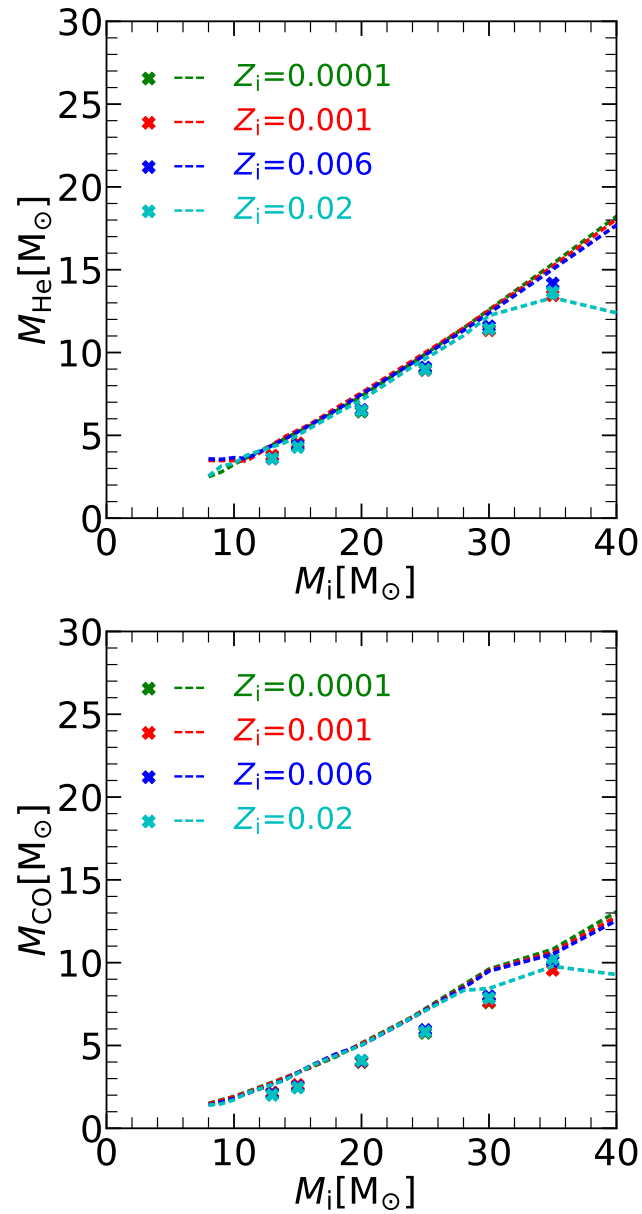


FIGURE 2.2: M_{HE} (top panel) and M_{CO} (bottom panel) as a function of M_i , for different values of Z_i . Lines show the data extracted from PARSEC stellar evolution models, while crosses represent the models of Chieffi & Limongi (2004).

ejecta of ^{56}Ni and the pre-supernova mass of CCSN (Umeda & Nomoto 2008; Utrobin & Chugai 2009; Utrobin et al. 2010). We note that also this relation is affected by some uncertainty, in particular on the determination of the pre-supernova mass M_{fin} . For this reason, we prefer to use, as the calibrating value for the models, the estimated value of the ^{56}Ni mass ejected by SN1987A, $^{56}\text{Ni} \sim 0.07M_{\odot}$ (Nomoto et al. 2013; Prantzos et al. 2018).

Given the explodability criterion and the ejected mass of ^{56}Ni , we adopt suitable explosion models to derive the corresponding ejecta. For this purpose, we use the CCSN models by Limongi & Chieffi (2003) and Chieffi & Limongi (2004) (hereafter CL04) because they tabulate the explosion isotopes as a function of the internal mass coordinate.

Each stellar model of the PARSEC grid is characterized by four known parameters, namely: M_i , Z_i , M_{fin} and M_{CO} . We use the mass of the C-O core, M_{CO} , to match the PARSEC models to CL04 ones for $Z_i = 0.0001, 0.001, 0.006, 0.02$. These are the only values of Z_i in common between CL04 and PARSEC. Once identified the CL04 explosion model that corresponds to a given M_{CO} , it is straightforward to integrate from the external layers inward until the desired ejecta of ^{56}Ni is reached. The corresponding mass coordinate of the inner layer provides the mass cut, M_{cut} , and hence the explosion ejecta.

This scheme needs to be made a bit more articulated to take into account that for the same M_i the PARSEC and CL04 models do not predict exactly the same M_{CO} . Simple interpolations are therefore applied.

We proceed as follows. For each PARSEC model of metallicity Z_i we identify in the corresponding CL04 grid the two explosive models that bracket the mass of the core, $M_{\text{CO}1} < M_{\text{CO}} < M_{\text{CO}2}$, with pre-explosive masses $M_{\text{fin}1}$ and $M_{\text{fin}2}$, respectively. Using the ^{56}Ni criterion we derive the corresponding mass cuts, $M_{\text{cut}}(M_{\text{CO}1})$ and $M_{\text{cut}}(M_{\text{CO}2})$, and the explosive ejecta, integrating from $M_{\text{cut}}(M_{\text{CO}1,2})$ to $M_{\text{fin}1,2}$. Finally, we use M_{CO} of the PARSEC model as interpolating variable to obtain $M_{\text{cut}}(M_i, Z_i, M_{\text{CO}})$ and the explosion ejecta $E_j^{\text{sn}}(M_i, Z_i, M_{\text{CO}})$ for all chemical species under consideration.

To estimate the mass of the remnant, M_{rem} , we assume that in successful CCSN the efficiency of fall-back is negligible, as shown by recent hydrodynamical simulations (Ertl et al. 2016). It follows that $M_{\text{rem}} = M_{\text{cut}}$ for successful CCSN and $M_{\text{rem}} = M_{\text{fin}}$ for failed SN. As to the nature of the compact remnant, we assign a neutron star for $M_{\text{rem}} < 2.9M_{\odot}$, or a black hole otherwise (Tews & Schwenk 2020; Kalogera & Baym 1996).

Before closing this section, two remarks are worth. The first applies to the matching parameter M_{CO} . Fig. 2.2 compares the PARSEC values of M_{HE} and M_{CO} with those derived from CL04 models, as a function of M_i . We note that the values of M_{HE} and M_{CO} of our PARSEC models, derived at the end of central carbon burning with a recent version of the PARSEC code (Fu et al. 2018), are a bit larger than predicted by CL04. This is due to the fact that in PARSEC we adopt a slightly more efficient core overshooting. An implication of this difference will be discussed later (Sect. 2.4).

The second consideration deals with the pre-supernova evolution. The stellar models of the CL04 grid were computed at constant mass, while our PARSEC tracks include mass loss by stellar winds for $M_i \geq 14 M_\odot$. However, this difference should not affect our results because besides the fact that we match the models using M_{CO} , mass loss is not so important for the progenitors of successful CCSN with $M_i \leq 25 M_\odot$, and especially for $Z_i \leq 0.006$. Powerful stellar winds affect the pre-supernova evolution of more massive stars, but these latter are not matched with CCSN explosive models as they fail to explode and only their wind ejecta are considered.

2.2.6 Explosion ejecta of pulsational pair instability and pair instability supernovae

Very massive stars that develop a final helium core mass in the range between $\sim 32 M_\odot$ and $\sim 64 M_\odot$ are expected to enter the domain of pulsational pair-instability supernovae (PPISN), before ending their life with a successful or failed core-collapse supernova (Woosley et al. 2002; Chen et al. 2014; Yoshida et al. 2016; Woosley 2017). During the pair-instability phase, several strong pulses may eject a significant fraction of the star's residual envelope and, possibly, a small fraction of the core mass. In contrast, the thermonuclear ignition of oxygen in stars with helium core masses between $\sim 64 M_\odot$ and $\sim 135 M_\odot$ leads to a pair-instability supernova (PISN), assimilated to a single strong pulse that disrupts the entire star, leaving no remnant behind (Heger & Woosley 2002; Heger et al. 2003b).

PISN has been usually associated with the first, extremely metal-poor stellar generations (e.g. Karlsson et al. 2008). However, recent stellar evolution models suggest that PISN could occur also for stars with initial metallicity $Z_i \approx Z_\odot/3$, which implies that they are potentially observable even in the local universe (Yusof et al. 2013; Kozyreva et al. 2014c). For these reasons, PPISN and PISN may play a key role to understand the chemical evolution of the Galaxy.

While the physical mechanisms behind PPISN and PISN are quite well understood, severe uncertainties affect the range of helium (or, equivalently, carbon-oxygen) core masses that drive stars to enter the pair-instability regime (e.g. Leung et al. 2019; Farmer et al. 2019; Marchant & Moriya 2020; Renzo et al. 2020; Costa et al. 2020a). In this thesis we adopt the indications from Woosley (2017), who suggests $32 \lesssim M_{\text{HE}}/M_\odot \lesssim 64$ for PPISN and $64 \lesssim M_{\text{HE}}/M_\odot \lesssim 135$ for PISN.

We model PPISN as a super-wind phase that ejects the surface layers, without any appreciable synthesis of new elements, until the star collapses to a BH. For each PARSEC model with a given helium core mass, the corresponding M_{rem} is obtained by interpolation in M_{HE} , between the values tabulated by Woosley (2017). Then, the total PPISN ejecta are estimated by integrating in mass the PARSEC structures from M_{rem} to M_{fin} . Finally, we add the PARSEC wind ejecta.

For PISN, we calculate the explosion ejecta from the zero-metallicity pure-helium stellar models provided by Heger & Woosley (2002), as a function of the mass $M_{\text{He-star}}$. Similarly to the case of PPISN, the helium core mass, M_{HE} , of our PARSEC tracks is taken as interpolating variable to perform the match with the

explosion models and derive the ejecta. Finally, we add the PARSEC contributions of all layers from M_{HE} to M_{fin} and the wind ejecta.

To better appreciate the contribution of PISNe we plot, in Fig. 2.3, the total ejecta of ^{12}C , ^{16}O , ^{24}Mg , ^{28}Si , S and Fe of the models by Heger & Woosley (2002), against the initial stellar mass, M_{HE} . In the same figure, we plot also the ejecta of two different models, computed by Kozyreva et al. (2014b). They latter models are evolved from the hydrogen zero age main sequence and for a non zero metallicity, $Z_i = 0.001$. The reason why we did not plot ejecta for ^{14}N is that they are negligible. In the Heger & Woosley (2002) models, the ejected masses of ^{14}N are below $0.0001 M_{\odot}$ while, in the Kozyreva et al. (2014b) models, the ejecta of ^{14}N are a fraction of a solar mass, but the $^{14}\text{N}/^{16}\text{O}$ mass ratio is at maximum 0.001.

The comparison of the Heger & Woosley (2002) models with the two Kozyreva et al. (2014b) models, is particularly interesting because it allows to assess the impact of the metallicity and of the H-rich envelope, on the ejecta. We first note that the ejecta of ^{16}O , and ^{28}Si , S and Fe, at the same M_{HE} values, are very similar. This indicates that PISN ejecta for these elements do not depend strongly on the metallicity of the models (at least at those low metallicities) and are practically unaffected by the surrounding H-rich envelopes. For ^{12}C and ^{24}Mg the ejecta are different, with the ones by Heger & Woosley (2002) being larger than those of Kozyreva et al. (2014b). We also note that, for the Heger & Woosley (2002) models, the total ejected mass of metals⁶, M_{metals} , comprises most of the PISN ejecta, with a fractional contribution, $M_{\text{metals}}/M_{\text{He-star}}$, that is generally larger than 97% for all tabulated models. This indicates that, at the end of the evolution, almost all the entire He mass is processed into metals.

We are thus quite confident that the results of this investigation are not significantly affected, even if we use the older Heger & Woosley (2002) zero metallicity pure He models, also for $Z_i \geq 0$.

Concerning the ejecta themselves, we note, from Fig. 2.3, that stars explode as PISN when their $65M_{\odot} \leq M_{\text{HE}} \leq 130M_{\odot}$ and that, within this interval, M_{HE} is well sampled.

We also can appreciate the odd behaviour of the plotted α -elements and the iron ejecta at increasing M_{HE} . Models with M_{HE} near the lower limit for PISN explosion do not produce iron but, instead, large amounts of α -elements, in particular oxygen. However, at increasing M_{HE} , the iron production quickly increases, becoming even larger than that of oxygen when M_{HE} reaches the upper limit. The relations of M_{HE} and M_i , the initial mass, at varying metallicity, are thus a fundamental ingredient to understand the relative contribution of PISNe to α -elements and Fe enrichment. The relations adopted here, similar to those shown in Fig. 2.2, is shown in Fig. 2.4, but for the full range of initial masses computed with PARSEC and for the metallicities used in this thesis.

With these relations we find that, for $Z_i \leq 0.006$, stars with $M_i > 100 M_{\odot}$ may enter the PPISN and PISN regimes (see Fig. 2.5). In this respect, our models

⁶According to standard terminology, metals refer to chemical species heavier than helium.

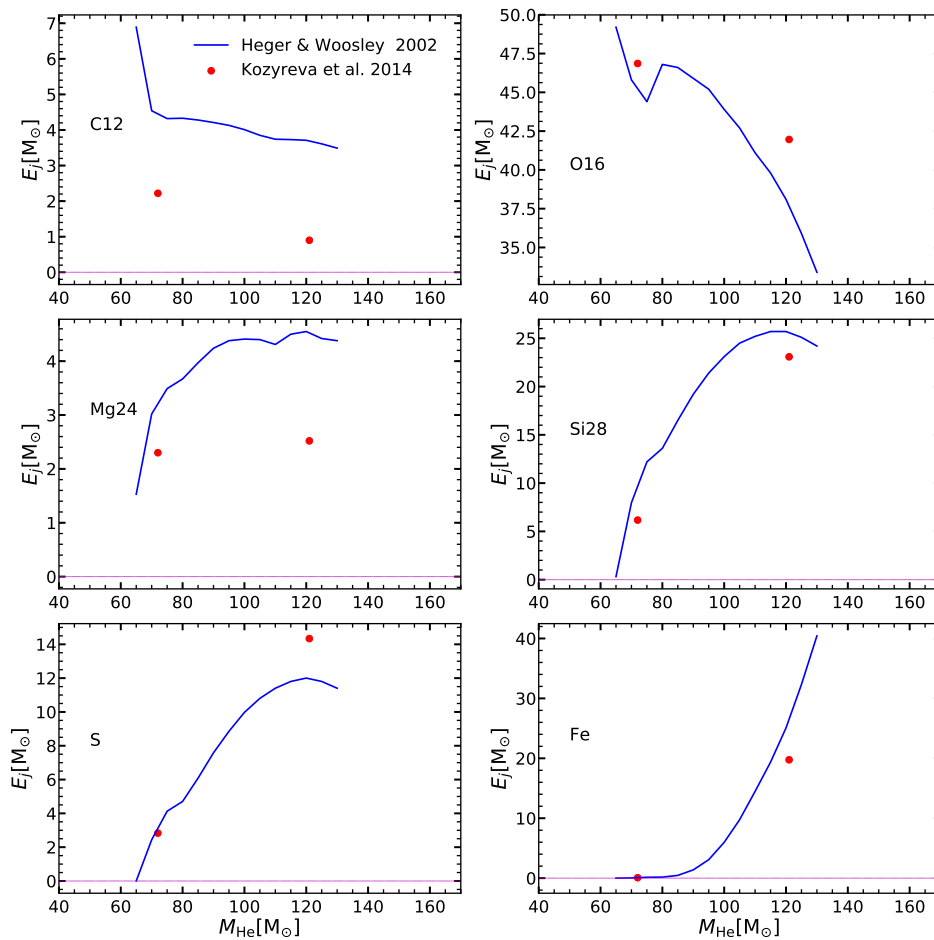


FIGURE 2.3: PISN Ejecta from [Woosley et al. \(2002\)](#) and [\(Kozyreva et al. 2014b\)](#), as labelled in the figure.

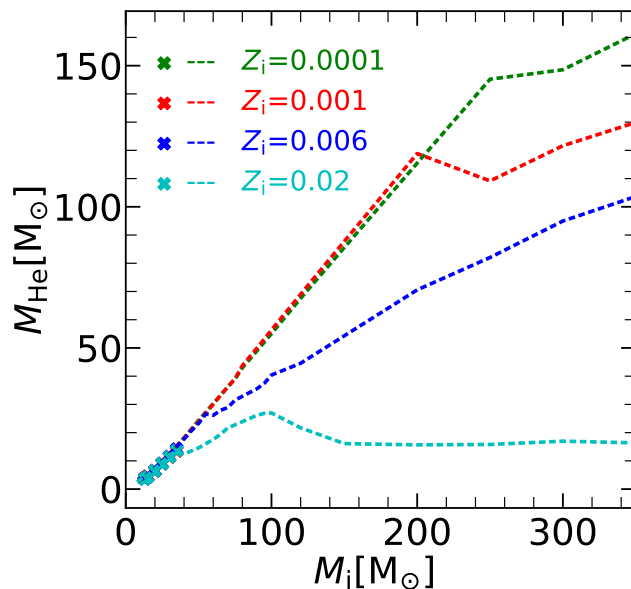


FIGURE 2.4: The He core mass, M_{HE} , as a function of the initial mass, M_i , for different values of the metallicity Z_i in PARSEC stellar evolution models. Crosses represent the models of [Chieffi & Limongi \(2004\)](#).

agree with earlier theoretical findings (e.g., [Kozyreva et al. 2014c](#)) and support the hypothesis that some superluminous supernovae recently observed at metallicity $\approx Z_{\odot}/3$, may be explained through the pair-instability mechanism, provided the IMF extends to VMO, that is $M_i > 150 M_{\odot}$ ([Woosley et al. 2007](#); [Kozyreva et al. 2014a](#)).

We note, however, that the M_{HE} and M_i relation is affected by uncertainties arising from different assumptions that must be performed in stellar evolution models. Among the most important ones, we recall here those concerned with the efficiency of the $^{12}\text{C}(\alpha, \gamma)^{16}\text{O}$ nuclear reaction rate ([Costa et al. 2020a](#); [Farmer et al. 2019](#)), and those concerned with the adopted formulations for the mass loss rates and their dependence on the stellar chemical composition, and on the enhancement due to evolution in proximity of the Eddington luminosity (e.g. [Vink et al. 2011](#)).

2.2.7 Ejecta of very massive stars that directly collapse to black holes

If a star is massive enough to build a helium core with $M_{\text{HE}} > 135 M_{\odot}$, no material will be able to avoid the direct collapse into a black hole (DBH), induced by the pair creation instability. Under these conditions no explosive ejecta are produced ([Fryer & Kalogera 2001](#); [Heger & Woosley 2002](#); [Nomoto et al. 2013](#)), and the only chemical contribution comes from wind ejecta. With the adopted mass-loss rates in PARSEC, these objects appear only at a low metallicity, $Z_i = 0.0001$, and

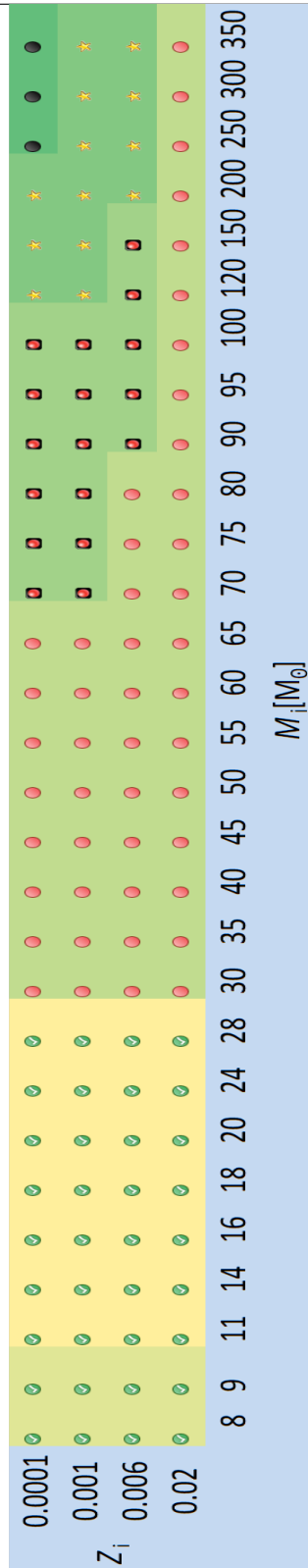


FIGURE 2.5: Final fate of massive and very massive stars as a function of M_i and Z_i . Green dot is a successful SN, from ECSN if the background is light green or CCSN if it is yellow; red dot is a BH from a failed CCSN; red dot in a black box is a BH from PPISN; yellow star is a thermonuclear explosion from PISN and black dot is a DBH.

initial masses $M_i > 200 M_\odot$. Conversely, at larger metallicities stars with $M_i > 200 M_\odot$ avoid the DBH channel, since the mass loss is efficient enough to drive their He-core masses into the regimes of PISN or failed CCSN.

2.3 Ejecta of AGB stars

We have complemented the ejecta of massive stars with those of AGB stars computed with the COLIBRI code (Marigo et al. 2013), in the mass range $0.7 \lesssim M_i / M_\odot \lesssim 6$ and for several metallicity values ($Z_i = 0.0005, 0.001, 0.002, 0.004, 0.006, 0.008, 0.01, 0.014, 0.017, 0.02, 0.03$). These models follow the whole thermally pulsing phase, TP-AGB, up to the ejection of the entire envelope by stellar winds. The initial conditions are taken from the PARSEC grid of stellar models at the first thermal pulse or at an earlier stage on the Early-AGB. COLIBRI and PARSEC share the same input physics (e.g., opacity, equation of state, nuclear reaction rates, mixing-length parameter) and the numerical treatment to solve the structures of the atmosphere and the convective envelope. For these reasons, the PARSEC+COLIBRI combination provides a dense, homogeneous and complete grid of models for low- and intermediate-mass stars (roughly ≈ 70 values of M_i for each metallicity value).

In COLIBRI models, the parameters describing the main processes that affect the TP-AGB phase, such as the mass-loss rates and the efficiency of the third dredge-up, have been thoroughly calibrated with observations of AGB stars in the Galaxy, Magellanic Clouds, and low-metallicity nearby galaxies (Girardi et al. 2010; Rosenfield et al. 2014, 2016; Marigo et al. 2017; Lebzelter et al. 2018; Pastorelli et al. 2019, 2020; Marigo et al. 2020). The COLIBRI yields account for the chemical changes due to the first, second, third dredge-up episodes and hot-bottom burning in the most massive AGB stars ($M_i \gtrsim 3 - 4 M_\odot$), and include the same chemical species as in PARSEC, from ^1H to ^{28}Si (see Sect. 2.2.1).

Finally, super-AGB stars are not treated explicitly here and their ejecta are taken from Ritter et al. (2018), for stars with $M_i = 6, 7 M_\odot$ and $Z_i = 0.0001, 0.001, 0.006, 0.02$ ⁷. The chemical composition of the ejecta is the result of third dredge-up episodes and hot-bottom burning. An overshoot scheme is applied to the borders of convective regions, including the bottom of the pulse-driven convection zone. As a consequence, the intershell composition is enriched with primary ^{16}O ($\approx 15\%$) in Ritter et al. (2018) computations, much more than in standard models without overshoot ($^{16}\text{O} \approx 1 - 2\%$), like in Karakas (2010).

2.4 Chemical ejecta from other authors

Here we present various combinations of chemical ejecta taken from the literature and compare the main trends as a function of M_i and Z_i . They are summarized in Table 3.2. The different sets of ejecta are then incorporated in our chemical evolution model of the MW (see Chapter. 4 and 5).

⁷<https://github.com/NuGrid/NuPyCEE>

As to the yields from AGB stars, we consider three sets, namely: M20 (from the COLIBRI code, Sect. 2.3), K10 (Karakas 2010) and R18 (Ritter et al. 2018). K10 provides the ejecta of AGB stars in the mass range $1 \lesssim M_i/M_\odot \lesssim 6$ for four metallicities ($Z_i = 0.0001, 0.004, 0.008, 0.02$). To obtain the yields at $Z_i = 0.001$ and $Z_i = 0.006$, we interpolate in metallicity between their original tables. R18 provide the ejecta of AGB and Super-AGB stars in the mass range $1 \leq M_i/M_\odot \leq 7$ for five metallicities ($Z_i = 0.0001, 0.001, 0.006, 0.01, 0.02$).

As to the yields of massive stars, including both wind and explosion contributions, we consider three sets, namely: R18 (Ritter et al. 2018), L18 (Limongi & Chieffi 2018) with and without rotation, and TW that refers to the new ejecta from this thesis (see Sect. 2.2). Nomoto et al. (2013) also published yields for massive stars, which however do not include the wind contributions, and therefore we did not consider them in our analysis.

R18 computed the ejecta of massive stars in the mass range $12 \leq M_i/M_\odot \leq 25$, for the same initial metallicities as their AGB models, i.e. $Z_i = 0.0001, 0.001, 0.006, 0.01, 0.02$, and for two models of explosion conditions, rapid (R_r) or delayed (R_d), respectively (Fryer et al. 2006).

LC18 calculated the ejecta in the mass range $13 \leq M_i/M_\odot \leq 120$ for three different rotational velocities ($V_{\text{rot}} = 0, 150, 300$ km/s), and four metallicities ($[\text{Fe}/\text{H}] = 0, -1, -2, -3$ dex). Here we use the version of their ejecta for $Z_i = 0.0001, 0.004, 0.008, 0.02$ publicly available on Github NuPyCEE repository⁸. Both R18 and LC18 sets have the noticeable property that wind and explosion ejecta derive from homogeneous stellar evolution models.

The distinguishing feature of our TW ejecta is that they range in mass beyond the classical limit of $M_i \approx 100 M_\odot$, extending up to $M_i = 350 M_\odot$, hence opening the possibility to investigate the chemical role of VMO in terms of stellar winds, PPISN and PISN explosions, and DBH channel.

To make a meaningful comparison among the different sets of ejecta we opt to use a dimensionless quantity, defined as the ratio between the newly produced yield of a given species j and the stellar initial mass, $P_j(M_i)$:

$$P_j(M_i) = [E_j(M_i) - (M_i - M_{\text{rem}}) X_{j,0}] / M_i \quad (2.10)$$

where the total ejecta $E_j(M_i)$ is defined by Eq. 2.8, and $X_{j,0}$ is the initial stellar abundance (in mass fraction) of the element j .

The different sets are compared in Figs. 2.7 - 2.10 as a function of M_i and a few values of the initial metallicity, $Z_i = 0.0001, 0.001, 0.006, 0.02$ respectively. We note that, for comparison purposes only, the LC18 yields for $Z_i = 0.006$ are obtained through a metallicity interpolation. The various panels show the ejecta of ${}^4\text{He}$, ${}^{12}\text{C}$, ${}^{14}\text{N}$, ${}^{16}\text{O}$, ${}^{20}\text{Ne}$, ${}^{24}\text{Mg}$, ${}^{28}\text{Si}$, S, Ar, Ca, Ti and Fe.

The AGB ejecta of ${}^4\text{He}$, ${}^{12}\text{C}$, ${}^{14}\text{N}$ exhibit significant differences among different sets. At $Z_i = 0.0001$ the K10 ejecta are much larger than those of R18 and M20. In general, the production of ${}^{12}\text{C}$ and ${}^{14}\text{N}$ predicted by K10 is much higher than M20, reaching a factor of ten for ${}^{14}\text{N}$ at $Z_i = 0.006$. At increasing metallicity,

⁸<https://github.com/NuGrid/NuPyCEE>

the differences become less pronounced. At $Z_i = 0.02$ the trend reverses with K10 predicting the lowest yields, but for the most massive AGB stars with hot-bottom burning. These discrepancies are mainly the result of different input physics (e.g., molecular opacities, mixing length parameter), mass-loss prescriptions, as well as differences in the efficiency of the third dredge-up.

In the domain of massive stars, our TW ejecta agree fairly well with non-rotating LC18 at both $Z_i = 0.0001$ and $Z_i = 0.006$, while the comparison slightly worsens at $Z_i = 0.02$, likely because the effect of mass loss becomes important at higher metallicity. We note that our TW set produces slightly larger fractions of ^{16}O , ^{20}Ne and ^{24}Mg than non-rotating LC18 at any Z_i .

At $Z_i = 0.0001$ rotating LC18 models yield a larger fraction of ^{14}N and, to a much less extent, ^{16}O and ^{12}C , compared to the non-rotating set. This trend remains at increasing metallicity ($Z_i = 0.006$ and $Z_i = 0.02$) but the over-production of ^{14}N appears less pronounced. Conversely, species such as ^{20}Ne and ^{24}Mg are produced less by stars with rotation.

The comparison between TW and R18 shows that, at $Z_i = 0.0001$, there is a fairly good agreement for ^{14}N , ^{16}O , ^{28}Si , S, Ar and Ca. At the same time, our TW ejecta produce less ^{12}C , more ^{20}Ne and ^{24}Mg than R18. At $Z_i = 0.006$ the TW predictions for ^{12}C , which agree well with non-rotating LC18, are about twice the R18 ejecta. We note that at this metallicity R18 presents a notable Fe production, higher by more than a factor of three compared to TW and LC18. A less pronounced, but still large Fe yield is predicted by R18 also at lower metallicity ($Z_i = 0.0001$). Similarly, in a narrow range of masses around $M_i = 15 M_\odot$, rotating LC18 yields for Fe exceed those without rotation by a factor of ~ 3 . Possible consequences of such Fe over-production will be discussed later in the sections devoted to chemical evolution models.

We note that none of the stellar models in the LC18 grid reaches M_{HE} high enough to enter the pair-instability regime. Recalling that stars with $M_i > 30 M_\odot$ fail to explode and collapse to a BH, it follows that in the mass range, $30 \leq M_i / M_\odot \leq 120$, LC18 ejecta are only due to stellar winds and become null for $M_i > 120 M_\odot$. Since the maximum mass in the R18 grid is $M_i = 25 M_\odot$, beyond this limit all R18 ejecta are zero.

It follows that we can analyse the total ejecta of VMO, $M_i \gtrsim 100 M_\odot$, by only referring to our TW set. At $Z_i = 0.02$, the most important contributions correspond to ^4He , ^{12}C and ^{14}N . For all the other elements there is no significant production. At $Z_i = 0.006$ VMO are expected to eject appreciable amounts of newly produced ^4He and ^{12}C , while the yield of ^{14}N decreases considerably. At the same time, other species provide notable contributions, such as ^{16}O , ^{24}Mg , ^{28}Si , S, Ar, Ca, Ti and Fe. The yields of these nuclides increase at higher M_i . This is a clear effect of the occurrence of PPISN and PISN which is favoured at lower metallicities. At $Z_i = 0.001$ and $Z_i = 0.0001$ the ejecta of all models with $M_i > 100 M_\odot$ have typical signatures of these explosive events. We note that at these metallicities the yields of ^{56}Fe may reach extremely high values, up to $20 M_\odot$ and $40 M_\odot$, respectively.

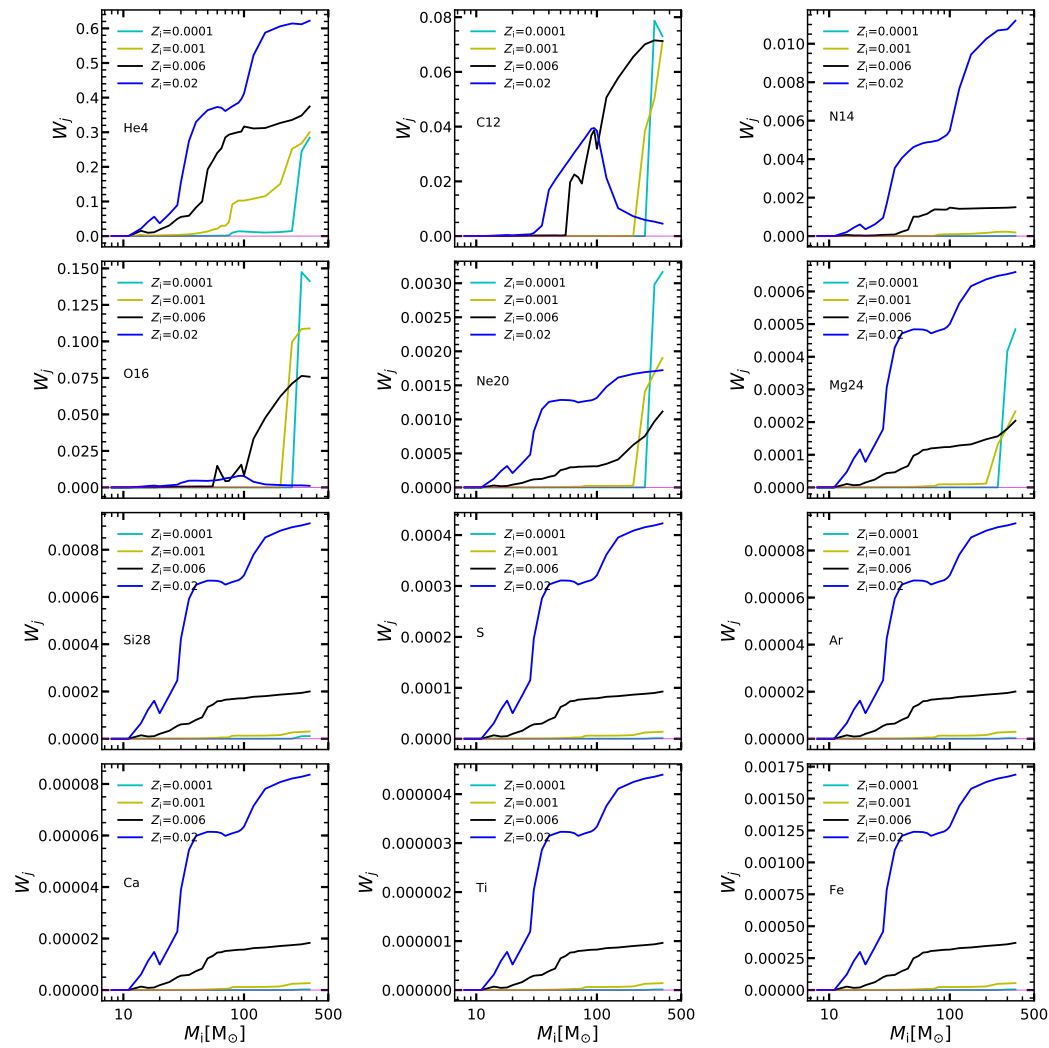


FIGURE 2.6: Fractional wind ejecta, W_j , derived from PARSEC stellar models, as a function of M_i and Z_i . The chemical species shown are ${}^4\text{He}$, ${}^{12}\text{C}$, ${}^{14}\text{N}$, ${}^{16}\text{O}$, ${}^{20}\text{Ne}$, ${}^{24}\text{Mg}$, ${}^{28}\text{Si}$, S, Ar, Ca, Ti, Fe.

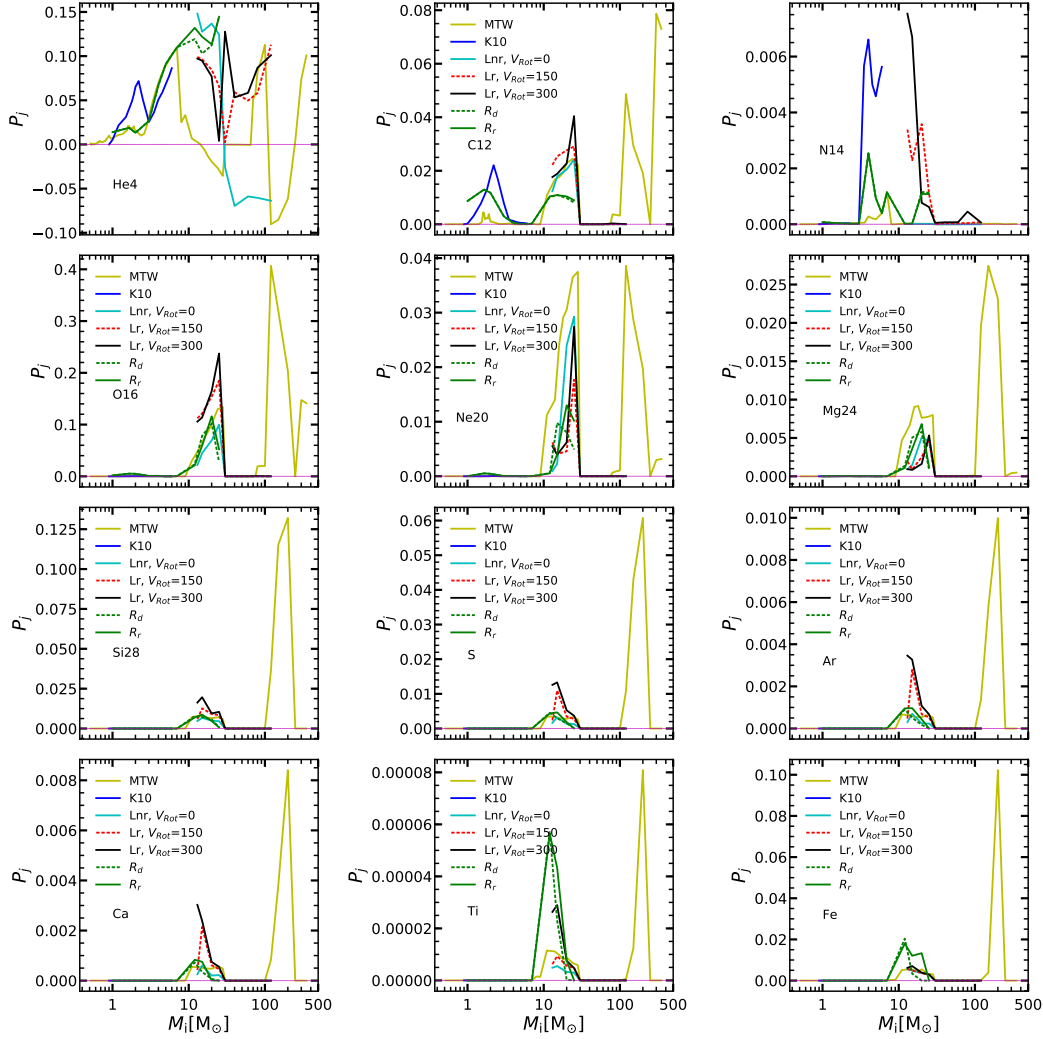
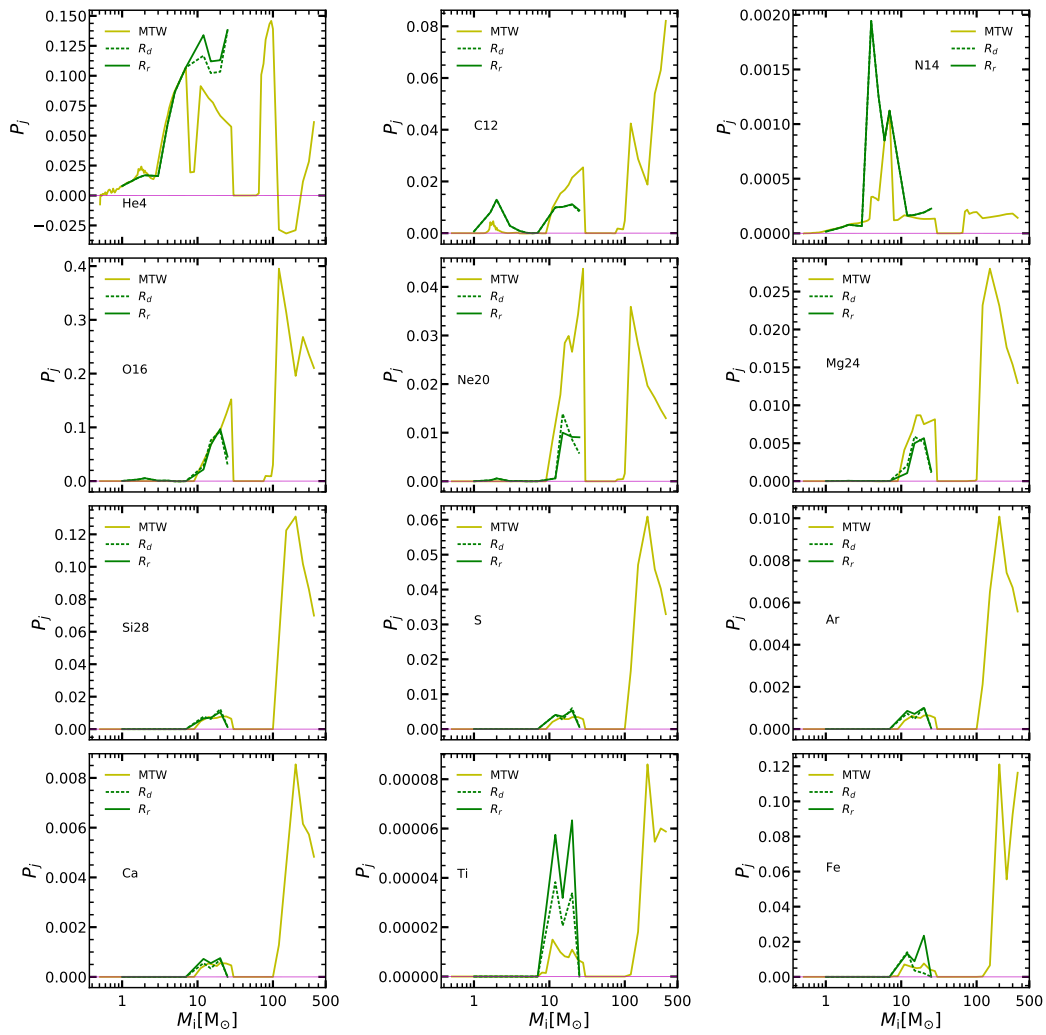


FIGURE 2.7: Fractional total ejecta (winds and explosion) of new production, P_j , for $Z_i = 0.0001$ as a function of M_i . Our MTW ejecta are compared with those of other literature works. The chemical species shown are ${}^4\text{He}$, ${}^{12}\text{C}$, ${}^{14}\text{N}$, ${}^{16}\text{O}$, ${}^{20}\text{Ne}$, ${}^{24}\text{Mg}$, ${}^{28}\text{Si}$, S, Ar, Ca, Ti, Fe.

FIGURE 2.8: The same as in Fig. 2.7 but for $Z_i = 0.001$.

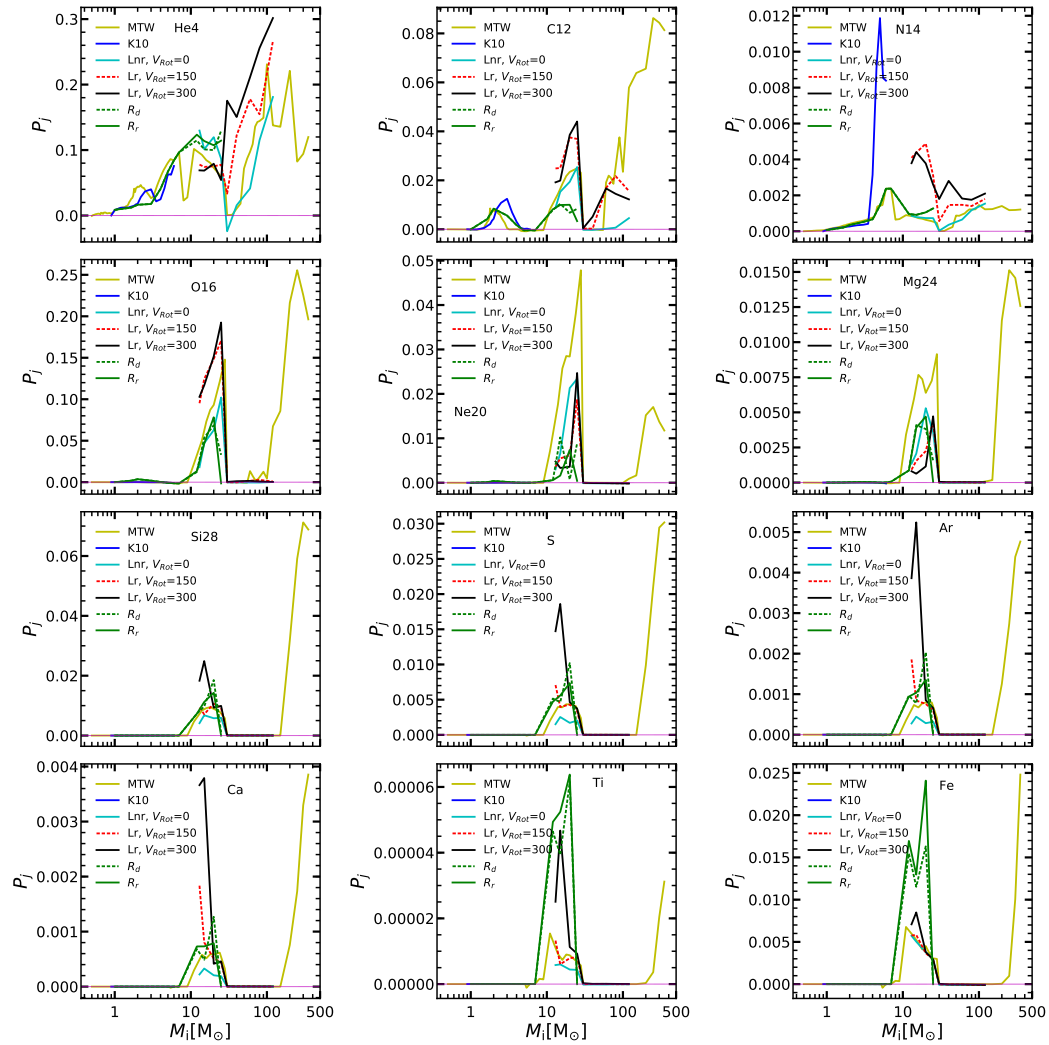
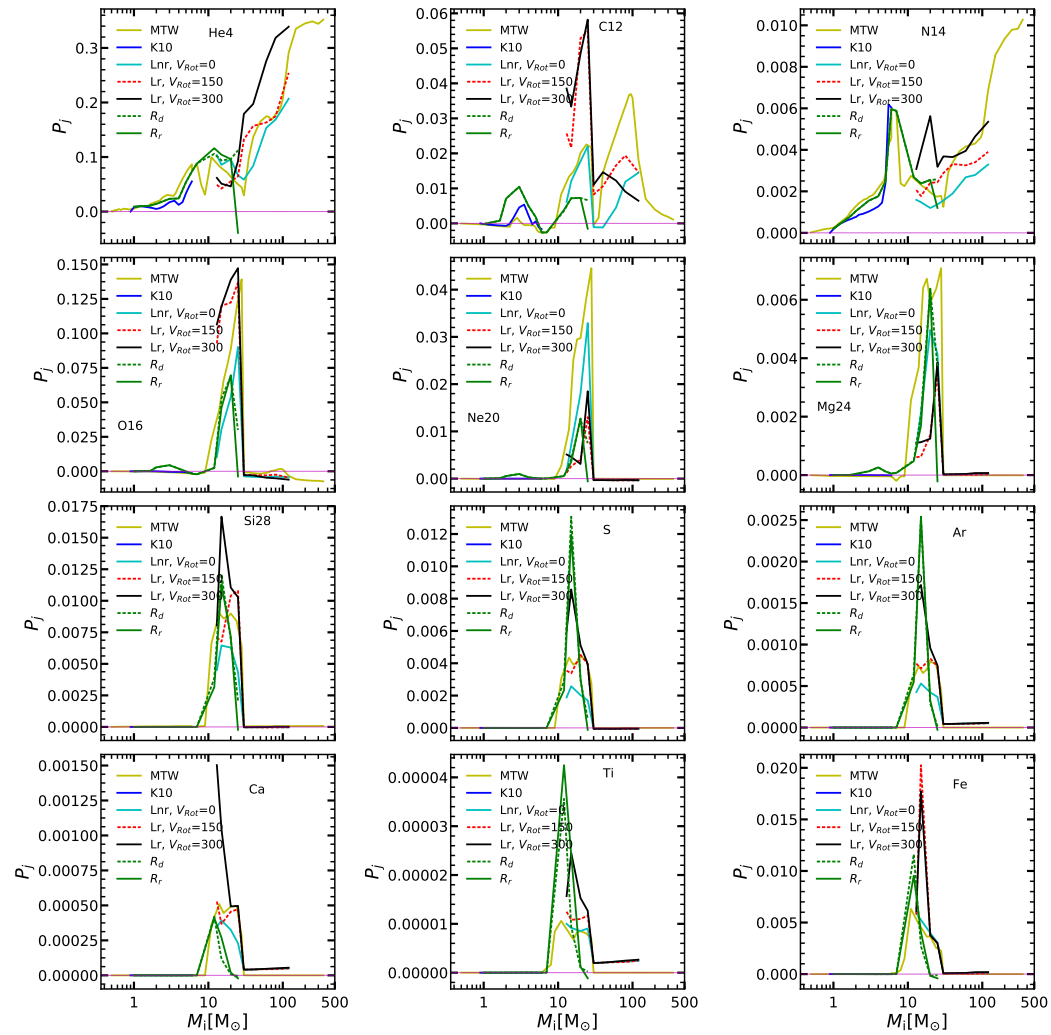


FIGURE 2.9: The same as in Fig. 2.7 but for $Z_i = 0.006$. Note that the LC18 ejecta for this metallicity are interpolated.

FIGURE 2.10: The same as in Fig. 2.7 but for $Z_i = 0.02$.

Chapter 3

Modelling chemical evolution: code, data, parameters

The chemical evolution code used in this thesis, CHE-EVO (Silva et al. 1998) describes one-zone open models including the infall of primordial gas. For simulating the chemical evolution of galaxies, we have to express the time derivative of total gas mass $M_g(t)$, and the mass of gas in the form of element i , $M_{g,i}(t) = X_i(t)M_g(t)$, in terms of computable quantities in time, t . This is shown in the following equation:

$$\dot{M}_{g,i} = \dot{M}_{g,i|SF} + \dot{M}_{g,i|FB} + \dot{M}_{g,i|Inf} \quad (3.1)$$

where the first term on the right represents the amount of gas going into star formation, the second term represents the amount of gas returned to ISM by dying stars and the last term signifies the amount of pristine gas infalling in the forming galaxy.

The rate of amount of gas going into star formation is formulated as :

$$\dot{M}_{g,i|SF} = -X_i(t)\psi(t) = -\dot{M}_{g,i}(t) \frac{\psi(t)}{M_g(t)} \quad (3.2)$$

where $\psi(t)$ is the SFR which will be described in more detail later. The rate of stellar feedback to the ISM is described as the following:

$$\dot{M}_{g,i|FB} = - \int_0^t \frac{\partial M(t-t', Z(t'))}{\partial t} \psi(t) [\phi(m)R_i(m, Z(t'))]_{m=M(t-t', Z(t'))} dt' \quad (3.3)$$

where $M(t, Z)$ is the mass of the star of metallicity Z and lifetime t , $\phi(m)$ is the IMF and $R_i(m, Z)$ the mass fraction in the form of element i ejected by the star of mass m and metallicity Z . The input parameters necessary to run the code is read from a .che file, and it is composed of a various list of parameters which dictates the outcome of the models. Out of all those, the most important parameters which are the most influential in deciding the fate of the model outcomes are described below:

- The star formation law used in this code is a Schmidt type law with the possibility to superimpose a burst:

$$\psi(t) = \nu M_g(t)^k + f(t) \quad (3.4)$$

where ν is the efficiency of star formation, M_g is the mass of the gas, and k is the exponent of star formation law. The second term $f(t)$ allows us the possibility to add a burst on the ongoing star formation, and it could be an analytical function, an exponential one, or a Schmidt-type one. The star formation law having a single episode is shown in Fig. 3.1; however, the star formation can have two episodes. Moreover, we can further choose what law does the second episode follows. It could be a constant function, as shown in Fig. 3.2, or it could Schmidt enhanced one, which is shown in Fig. 3.3. In this thesis, we have used a Schmidt-type without any burst to keep the model simple. In other words, don't consider the $f(t)$ in the Eq. 3.4

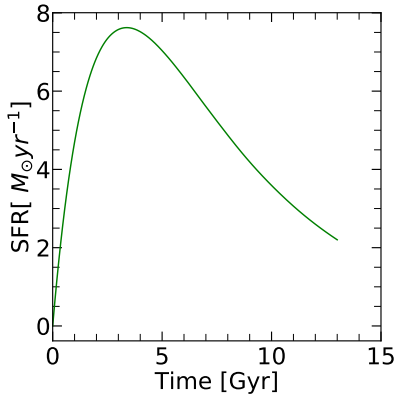


FIGURE 3.1: Simple star formation with no second episode

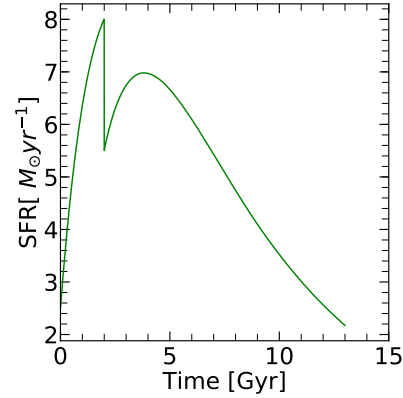


FIGURE 3.2: Complex star formation with constant second episode

- A fundamental assumption of chemical evolution models is the IMF:

$$\phi(M_i) = \frac{dn}{d\log(M_i)} \propto M_i^{-x}. \quad (3.5)$$

We use a Kroupa-like two-slope power law IMF with $x = 0.5$ for $0.1 \leq M_i/M_\odot \leq 1$, while we vary the slope for $M_i > 1 M_\odot$, as well as the upper mass limit of the IMF, M_{UP} , to search for best fitting models with different ejecta combinations used during this work. We consider IMF slopes between $x = 1.7$ (Kroupa et al. 1993) and $x = 1.3$ (Kroupa 2001), the latter being adopted also by Chabrier (2003).

- Exponential Infall timescale : It is assumed that the gas is accreted in the galaxy at an exponential rate which is given as follows:

$$\dot{M}_{g,i|Inf} = X_{i,Inf} A_{Inf} \exp(-t/\tau_{Inf}) \quad (3.6)$$

normalized in order to accrete a mass of gas M_{Inf} at time t_{Inf} . $X_{i,Inf}$ is the mass fraction of element i in the infalling gas. We can change the infall

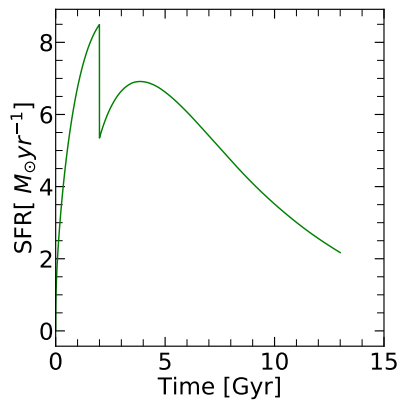


FIGURE 3.3:
Complex star
formation with
Schimdt type
second episode

timescale of the gas from very low to very high and see how it dictates the outcomes of our results.

- Type Ia supernovae are also taken into account according to the single degenerate scenario and computed following the standard formalism first introduced by [Matteucci & Greggio \(1986a\)](#). The contribution of these sources to the chemical enrichment is regulated by the parameter A_{SNIa} , which sets the fraction of the number of binary systems with a total mass in the $3 M_{\odot}$ - $16 M_{\odot}$ range, effectively contributing to the SNIa rate.

The code calculates the evolution of a large number of elements with respect to time, and from that, we are able to calculate the abundance ratios. The code also computes the evolution of rates of SNI and SNIa, the gas mass evolution, the mass of the star, the mass of the remnant and the total mass evolution with time. We take the yields of SNIa from [Iwamoto et al. \(1999\)](#), from which most of the iron in our galaxy is supposed to be produced. Here we adopt $Z_{\text{protoSUN}} = 0.017$, which is the initial metallicity of the PARSEC $1 M_{\odot}$ model that best reproduces the currently observed Sun's properties when using the [Caffau et al. \(2011\)](#) solar mixture ([Bressan et al. 2012](#)).

3.1 Method to choose the data

Once we have described the code, the next important thing before running models is to select the observed data we want our models to reproduce. With a large amount of data available currently, it's essential to choose the right dataset to work on. This subsection discusses the method used to choose the data and the data itself in more details.

3.1.1 Chemical properties of stars in the solar vicinity

The large amount of data collected over the years for stars in the solar vicinity led to the definition of different Galactic components, namely: the thin and thick discs, the halo and the α -enhanced metal-rich population (Allende Prieto et al. 2008; Gilmore et al. 2012; Zucker et al. 2012; de Laverny et al. 2013). The populations of the MW disc can be distinguished in various ways. For example, by adopting kinematic parameters, Jurić et al. (2008) pointed out that the stellar number density distribution of the MW could be well reproduced with two components with different scale heights above the Galactic plane: the thick disc with a scale height of $\simeq 900$ pc, and the thin disc with a scale height $\simeq 300$ pc.

At the same time, chemical abundances reveal the existence of clearly separate sequences of α -elements as a function of $[\text{Fe}/\text{H}]$, with thick disc stars generally belonging to a high $[\alpha/\text{Fe}]$ (α -enhanced) sequence, while thin disc stars exhibiting a lower $[\alpha/\text{Fe}]$ ratio at the same $[\text{Fe}/\text{H}]$ (e.g. Plevne et al. 2020; Grisoni et al. 2017; Kawata & Chiappini 2016; Bekki & Tsujimoto 2011; Feltzing et al. 2003; Prochaska et al. 2000).

The classification based on kinematical properties and the one based on abundance measurements provide somewhat different results so that it is not clear which is the best way to group these stars (Boeche et al. 2013). In this respect, it has often been pointed out that chemical evolution leaves a persistent imprint that hardly changes, while kinematic properties are more likely to vary as they may be affected by dynamical interactions (Schönrich & Aumer 2017; Vera-Ciro et al. 2016).

In recent years, ages of individual stars have been measured with sufficient accuracy to be used as robust population indicators, like in the case of star clusters (Fuhrmann 2011). We emphasize that age cannot be taken as a proxy for metallicity, rather it is a complementary independent parameter that concurs to define the full population box, i.e. the distribution of stars in age and abundances which, together with spatial and kinematic parameters, gives the information necessary to reconstruct the star formation history in a galaxy.

We also explore the homogeneous set of data of disc stars provided by Bensby et al. (2014), who conducted a high-resolution and high signal-to-noise spectroscopic analysis of 714 F and G dwarf and subgiant stars in the solar neighbourhood. This study is particularly suited for our purpose because, based on the analysis of their kinematic properties by Casagrande et al. (2011), each star in the sample is assigned a relative membership probability, TD/D , defined as the ratio between the thick disc probability and thin disc probability.

Bensby et al. (2014) classified stars with $TD/D > 2$ – having the probability of belonging to the thick disc of least twice that of belonging to the thin disc –, as potential thick disc stars, while those with $TD/D < 0.5$ as potential thin disc stars. Adopting the same criterion, we count 387 thin disc stars and 239 thick disc stars. We discard 88 stars with $0.5 < TD/D < 2$. The existence of at least two distinct sequences is clearly visible in the abundance patterns that define the so-called α -enhancement, as illustrated in the $[\text{O}/\text{Fe}]$, $[\text{Mg}/\text{Fe}]$, $[\text{Si}/\text{Fe}]$ and $[\text{Ca}/\text{Fe}]$ vs. $[\text{Fe}/\text{H}]$ diagrams of Fig. 3.4. Interestingly, the $[\text{O}/\text{Fe}]$ vs. $[\text{Fe}/\text{H}]$ diagram clearly shows

not only that the two disc populations draw separate sequences, but also that the slopes of two branches are different at increasing [Fe/H].

3.1.2 Selection of Data

There are a large number of observed datasets by different authors in the literature, but to choose the most accurate one suited to work is a very important task. Different authors normalize the data differently based on different initial solar abundances. For this thesis, we started with a library of data from various authors and different stars for a large number of elements. But with time and more exploration of more literature, we decided to use the homogeneous set of data provided by [Bensby et al. \(2014\)](#) who conducted a high-resolution and high signal-to-noise spectroscopic study of 714 F and G dwarf and subgiant stars in the Solar neighbourhood because some of the other surveys such as [Mikolaitis et al. \(2017\)](#) do not provide the oxygen abundances and the abundance of oxygen provided by [Bensby et al. \(2014\)](#) is more steeper than the others and we intend to investigate this feature also discussed in [Kubryk et al. \(2015\)](#). For normalizing the data, we took [Caffau et al. \(2009\)](#) as our basis of initial solar abundances and normalized the data accordingly. The formula used to do that is as follows:

$$[Ele/Fe]_{caf} = [Ele/Fe]_{orig} + \log_{10}(N_{Ele})_{orig} - \log_{10}(N_{Fe})_{orig} - \log_{10}(N_{Ele})_{caf} + \log_{10}(N_{Fe})_{caf} \quad (3.7)$$

where Ele means the element we are correcting. For example if we are correcting for oxygen the formula used is:

$$[O/Fe]_{caf} = [O/Fe]_{orig} + \log_{10}(N_O)_{orig} - \log_{10}(N_{Fe})_{orig} - \log_{10}(N_O)_{caf} + \log_{10}(N_{Fe})_{caf} \quad (3.8)$$

In the data show in Fig. 3.4, it can be noticed that there is an old and α -enhanced disc population, and a younger and less α -enhanced disc population. They selected the sample based on the kinematics and metallicities of the stars. The kinematical criteria they used to select the thick disc and thin disc stars is that the Galactic space velocities of the stellar populations follow a Gaussian distribution. The probability of a star belonging to thick disc, thin disc and halo are given as TD, D and H respectively and is dependent on the velocity distribution (assumed to be Gaussian), rotation velocities, as well as the observed fractions(X) for each stellar populations in the Solar neighbourhood. They distinguished the entire sample based on thick disc-to-thin disc probability ratio (TD/D) versus metallicity of the stars taken from [Casagrande et al. \(2011\)](#) and the probability ratio is defined as the following:

$$TD/D = \frac{X_{TD}}{X_D} \cdot \frac{f_{TD}}{f_D} \quad (3.9)$$

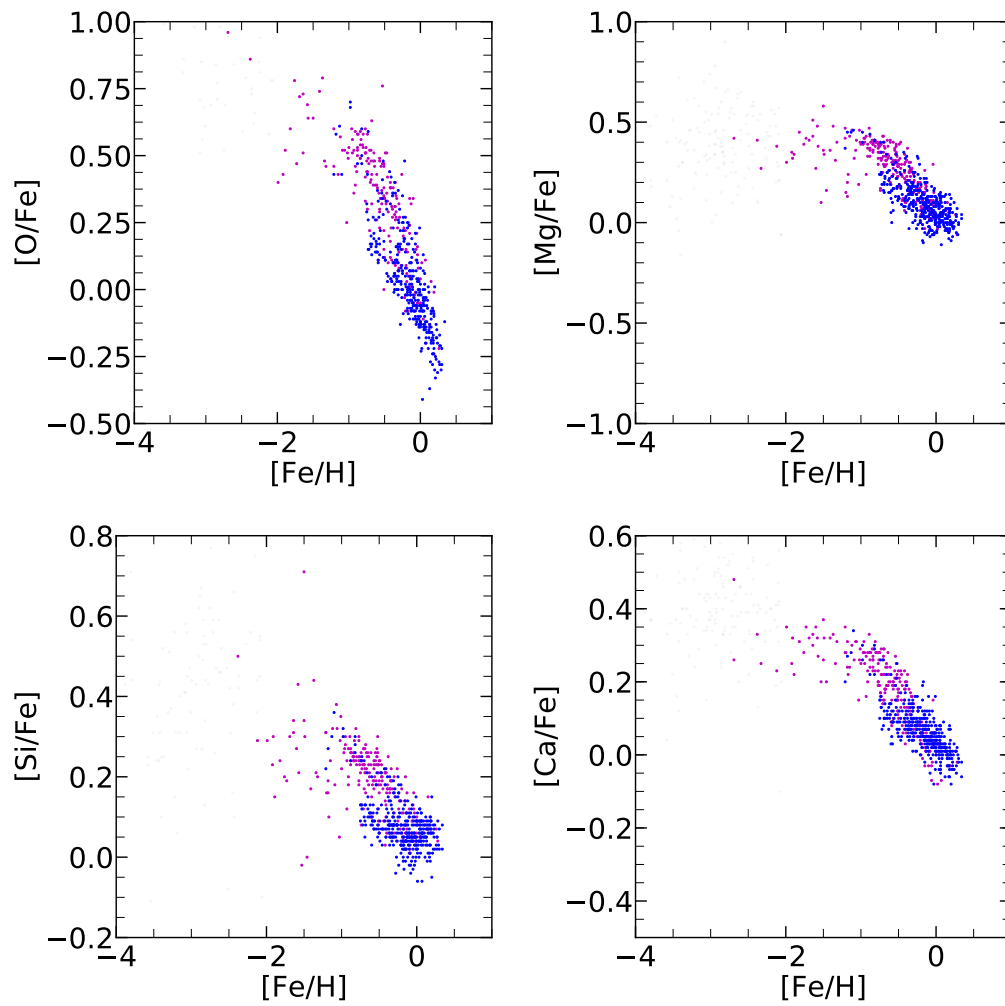


FIGURE 3.4: The $[X/Fe]$ vs. $[Fe/H]$ evolution of the four elements O, Mg, Si, Ca. The data has been taken from [Bensby et al. \(2014\)](#). The thin disc stars are shown in blue whereas the thick disc stars are shown in magenta.

where X is the observed fraction of the population and f_i is the probability for the individual population. Stars with $TD/D > 2$, which means that the probability of it being a thick disc star is twice of it being a thin disc star, are classified as potential thick disc stars, and vice versa i.e. $TD/D < 0.5$ are, to a first approximation, classified as potential thin disc stars. Adopting the same criterion, we count 387 thin disc stars and 239 thick disc stars. We discard 88 stars with $0.5 < TD/D < 2$.

After adopting the same constraints provided by [Bensby et al. \(2014\)](#) to distinguish the two populations we have plotted the individual stars in several diagrams. The existence of at least two distinct populations is clearly visible in the metallicity- α -enhancement diagram ($[O/Fe]$, $[Mg/Fe]$, $[Si/Fe]$ and $[Ca/Fe]$ vs $[Fe/H]$ diagrams plotted e.g. in Fig. 3.4). In the $[O/Fe]$ vs $[Fe/H]$ diagram of this figure not only it is evident that the thick and thin disc populations evolve separately, but also that the slopes of their evolution, at increasing $[Fe/H]$, are different. In the similar abundance diagrams constructed with other *alpha* elements, these differences are less apparent.

Since the difference in the slopes which is clearly seen in the $[O/Fe]$ vs $[Fe/H]$ diagram is challenging as it was found by [Kubryk et al. \(2015\)](#) too, in the next section we will try to see under which conditions the two sequences can be explained.

In order to simplify our analysis, we will assume in the following sections that the thin and thick disc populations evolve separately. This is clearly not the case because they are populating the same volume in the solar neighbourhoods but it will allow at least to check our models on individually well-separated populations. We could have considered the two populations together and tried to obtain a model that reproduces a sort of an average path, as done several times in the past. However, the evidence that the two population are different is so strong that reproducing their *averaged* properties is even less meaningful. Instead, we begin with reproducing the thin disc population and then we will consider the thick disc one and finally, we will compare the resulting constraints on their evolution.

In addition to the data used by [Bensby et al. \(2014\)](#) we have also incorporated the data provided by [Buder et al. \(2019\)](#) survey, where they provide data of 7066 dwarf, turn-off, and subgiant stars in the solar neighbourhood. And also this data shows the steepness of the slope in $[O/Fe]$ as in [Bensby et al. \(2014\)](#) and almost overlaps this data. The GALAH survey ([Buder et al. 2019](#)) provides data for stars with higher metallicities or till higher $[Fe/H]$ compared to [Bensby et al. \(2014\)](#) and for the purpose of this thesis we have concentrated on the latter as the modelling would change depending on the final metallicity we wish to obtain from the chemical models.

In the next chapter, we will discuss how we use our code to run models to reproduce the above discussed data and what are the methods adopted to find the best model.

ν [Gyr ⁻¹]	ASNIa	k_{sch}	τ_{inf} [Gyr]
0.3	0.05	1.0	5.0
0.3	0.03	0.5	2.0
0.6	0.05	1.0	5.0
1.0	0.09	1.5	10.0

TABLE 3.1: The values of the four parameters for our initial exploration of chemical evolution models. The first row shows the reference values that have been kept fixed when varying the other parameters.

3.2 Effect of Model parameters

In this section, a brief review is given on how the model parameters namely, ν , the star formation efficiency, *ASNIa*, the normalization of the Supernovae Type Ia, τ_{inf} , the exponential infall timescale and k_{sch} , the exponent of Schmidt law, affect the chemical evolution models. For this purpose, the following has been done:

- I select a reference value for each of these parameters, as indicated in the first row of Table. 3.1.
- I have run a series of models by changing each of the parameters at a time keeping the other parameters fixed to their reference values. These other values are shown in the other rows of Table. 3.1.

3.2.1 Effect of k-sch

Here I discuss the effect of changing the parameter k_{sch} , the exponent of the Schmidt law. In Fig. 3.5 I show three models run with three different values of $k_{sch} = 0.5, 1.0, 1.5$, keeping all the other parameters fixed. Generally k_{sch} is varied between $k_{sch} = 1.0$ and $k_{sch} = 2.0$. However a $k_{sch} < 1.0$ could be appropriate to describe a SFR less dependent on the gas density variation, as in analytical models describing burst of constant SFR. For this reason, I have also computed models with $k_{sch} = 0.5$. It can be seen that having a lower k_{sch} causes the SFR to peak at earlier ages and with a higher value. With the lower value of $k_{sch} = 0.5$, the gas is consumed more rapidly because the SFR is less dependent on the gas fraction. In turn, the gas is consumed more rapidly and hence the final gas fraction for a model with $k_{sch}=0.5$ is lower. The SNII rates follow directly the SFR, as expected, while the SNIa rate keeps a dependence on the SFR, but smoothed on the larger time scale of binary evolution to the SNIa explosion. Also, since the SFR is higher for a lower value of k_{sch} , the final metallicity reached by such a model is also higher compared to the models with higher k_{sch} . Finally, the lower panels of the figure show the run of the elemental abundances ratios [O/Fe] [Mg/Fe] against [Fe/H]. We note that, at increasing k_{sch} , the [O/Fe] [Mg/Fe] and decrease, again because of the lower SFR as in the case of the global metallicity.

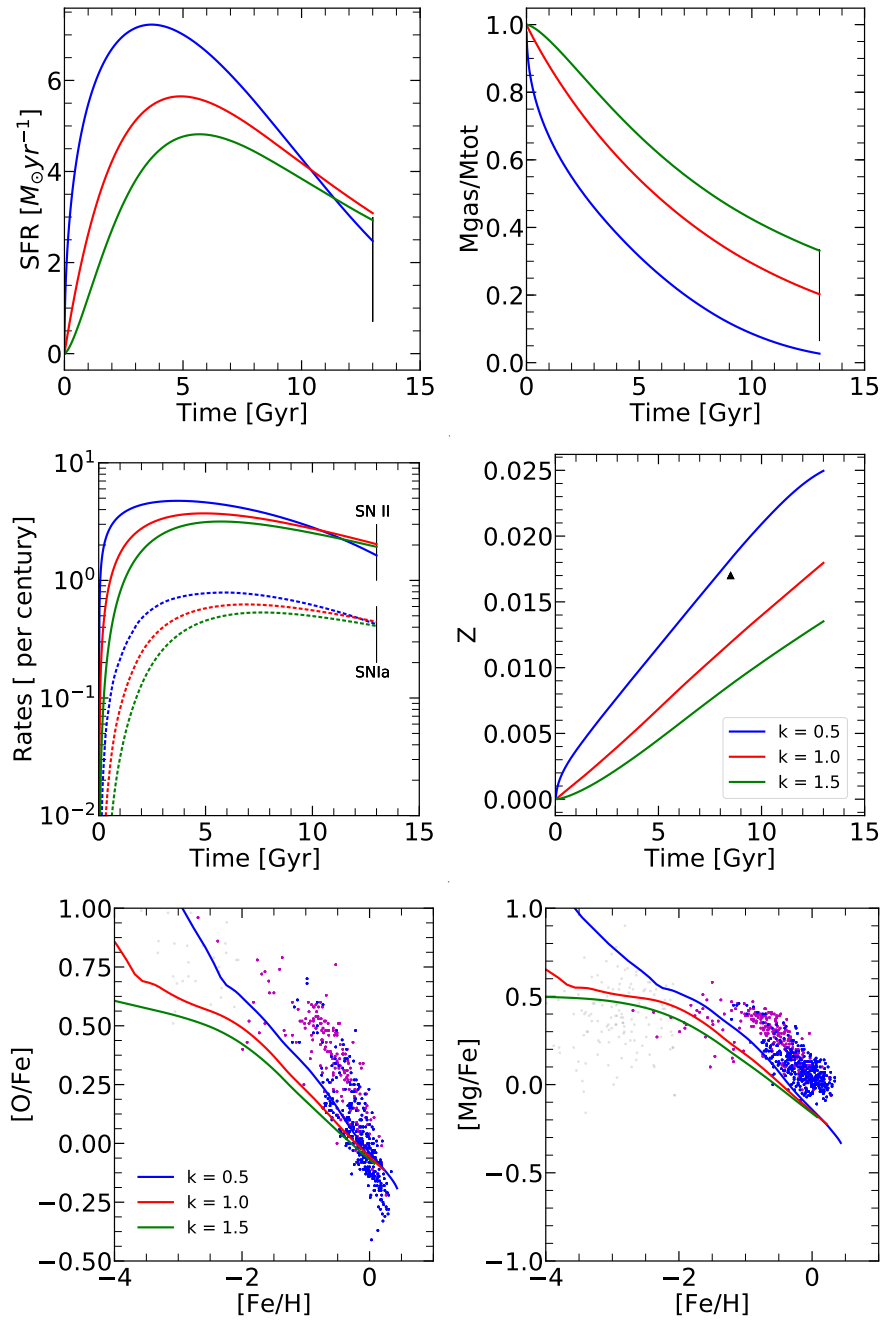


FIGURE 3.5: The effect of changing the k_{sch} on the chemical evolution. The models have been run for three values of $k_{sch} = 0.5, 1.0, 1.5$ depicted by the blue, red and green lines respectively. The other three parameters have been kept fixed to their reference values. The first four panels, from upper left to lower right show, respectively, the evolution of the SFR [M_{\odot}/yr], gas fraction, SNIi and SNIa rates per century and total gas metallicity. The vertical bars plotted at an age of 13 Gyr show their current estimated values, which will be discussed in more detail later. The solid triangle in the metallicity panel marks the initial value of the solar metallicity, resulting from the PARSEC calibration. The bottom panels show the run of the abundances ratios [O/Fe] [Mg/Fe] against [Fe/H]. In these panels, the data are the same of those plotted in Fig. 3.4.

3.2.2 Effect of the gas infall timescale, τ_{inf}

In this subsection, I discuss the effects of changing the τ_{inf} , the gas infall timescale. From Fig. 3.6 it can be seen that, as τ_{inf} increases from 2 Gyr to 10 Gyr, the SFR decreases and due to this, the metallicity, Z also gets lower as can be seen by the middle right panel. Looking to the run of the elemental abundances ratios [O/Fe] [Mg/Fe] against [Fe/H], we can see that their overall evolution is barely affected except that the models with higher final τ_{inf} are able to proceed further in the [Fe/H] evolution.

3.2.3 Effects of varying the parameter ASN_{Ia}

The parameter ASN_{Ia} is related to the production of SNIa from binary stellar evolution of intermediate and low mass stars. In Fig. 3.7, I show how changing this parameter affects the chemical evolution models. An increase of the parameter ASN_{Ia} directly increases the SNIa rate and so the amount of Iron produced by the chemical evolution models. Due to this, the overall metallicity also increases. For elemental abundances, it can be noticed that, as the SNIa value is increased, the [Fe/H] values of the models also increase. Correspondingly the [O/Fe] and [Mg/Fe] ratios decrease. Obviously, the differences become important once the SNIa begin to be efficiently produced by during the evolution. This happens above [Fe/H] ~ -1.5 , for the reference parameter adopted here.

3.2.4 Effect of varying the star formation rate efficiency, ν

In Fig. 3.8 we show the impact of varying the star formation efficiency ν . I explored values of $\nu = 0.2, 0.5, 1.0$, keeping the other parameters fixed to their reference values. As it can be expected, by increasing ν , the early SFR increases, resulting in a sharper initial peak. In turn, since the models with higher ν consume more gas, their gas fraction decrease faster, as can be seen in the top right panel. This affects the SFR at later times, that becomes lower. The SN rates follow the SFR trend, with a delay due to binary evolution in the case of SNIa. Models with high ν produce more metals which can be seen in the overall metallicity evolution. Even in this case, the final metallicity may be affected by the later evolution of the SFR. However, these trends depend on the adopted reference parameters and, with those adopted here, the models with $\nu = 0.5$ and $\nu = 1.0$ reach the same final metallicity.

Also, the [O/Fe] the [Mg/Fe] and the [Fe/H] values are affected by the variation of this parameter. Both the [O/Fe] and [Mg/Fe] curves shift at increased [Fe/H] values, but the effect is not strong.

As already said, the analysis has been made by selecting some reference parameter values that were kept fixed while changing each parameter at a time. The results just described, refer to these reference parameters and it is not easy to predict how the chemical evolution model responds when also the reference parameters are changed. For this reason, my next step is that of building a large grid of

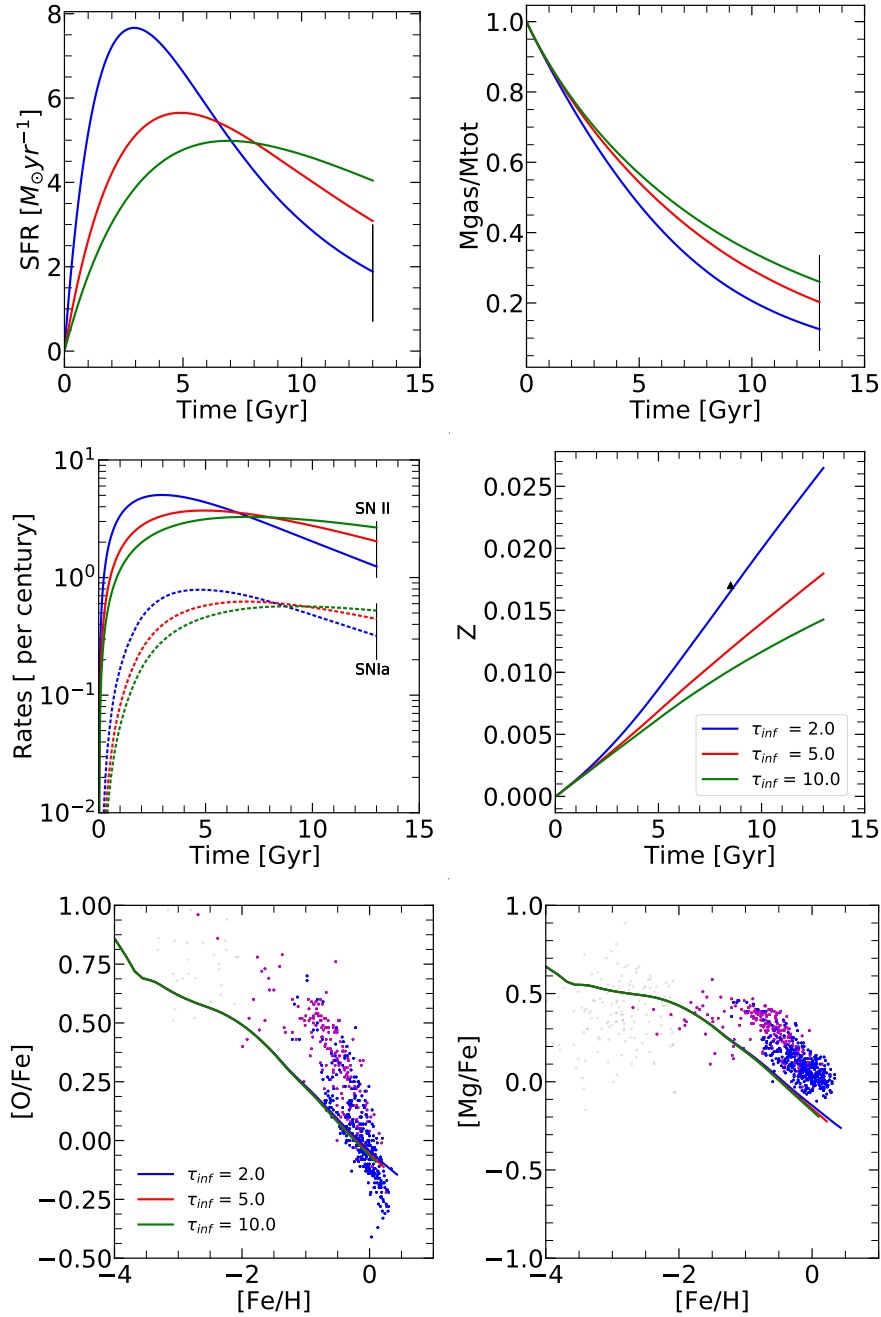


FIGURE 3.6: Same as Fig. 3.5 but changing the infall timescale here for the values $\tau_{inf} = 2.0, 5.0, 10$ Gyr and keeping the other parameters fixed to their reference values.

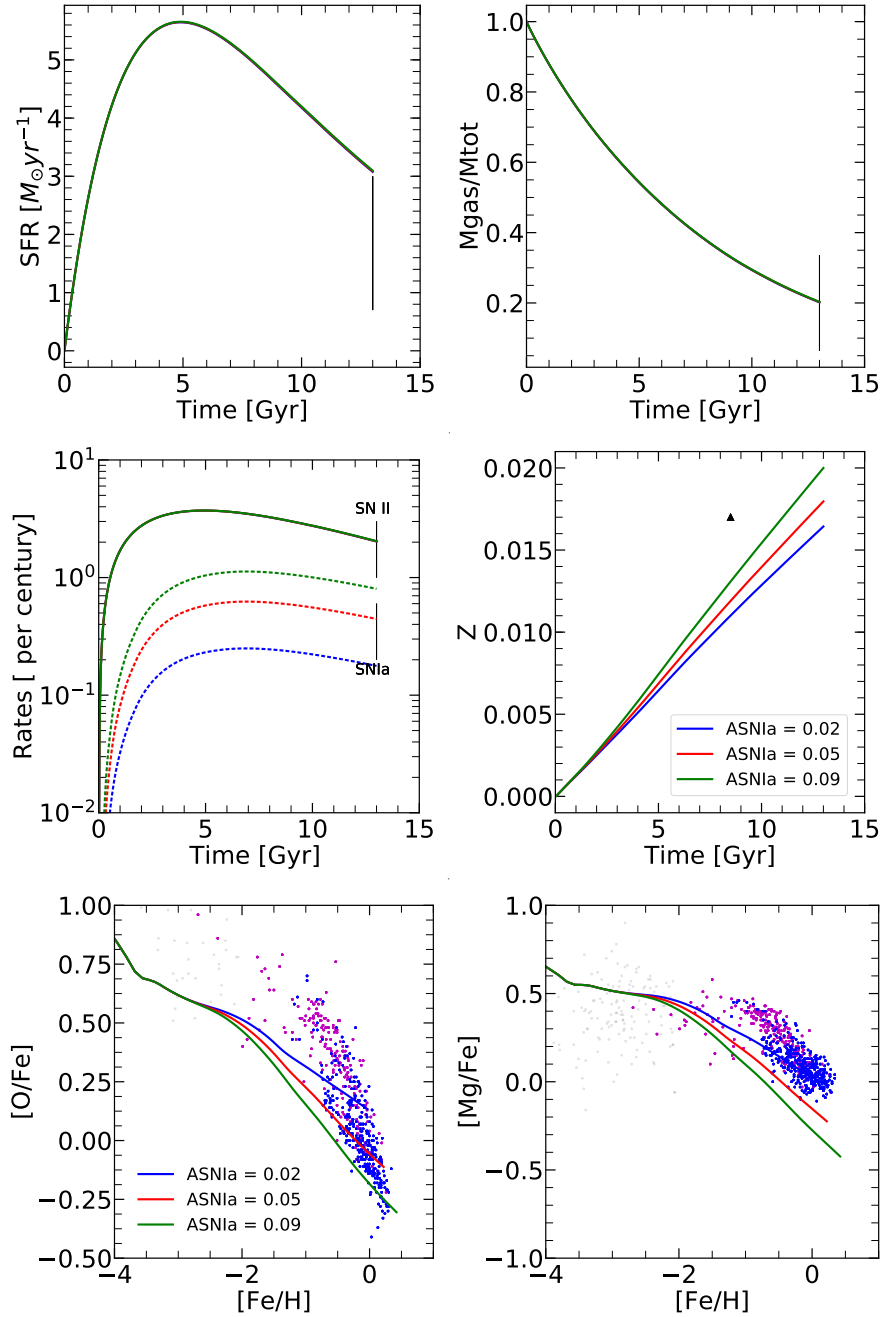


FIGURE 3.7: Same as Fig. 3.5 but varying the parameter $ASNIa$. We explore here $ASNIa=0.02, 0.05, 0.09$, keeping the other three parameters fixed to their reference values.

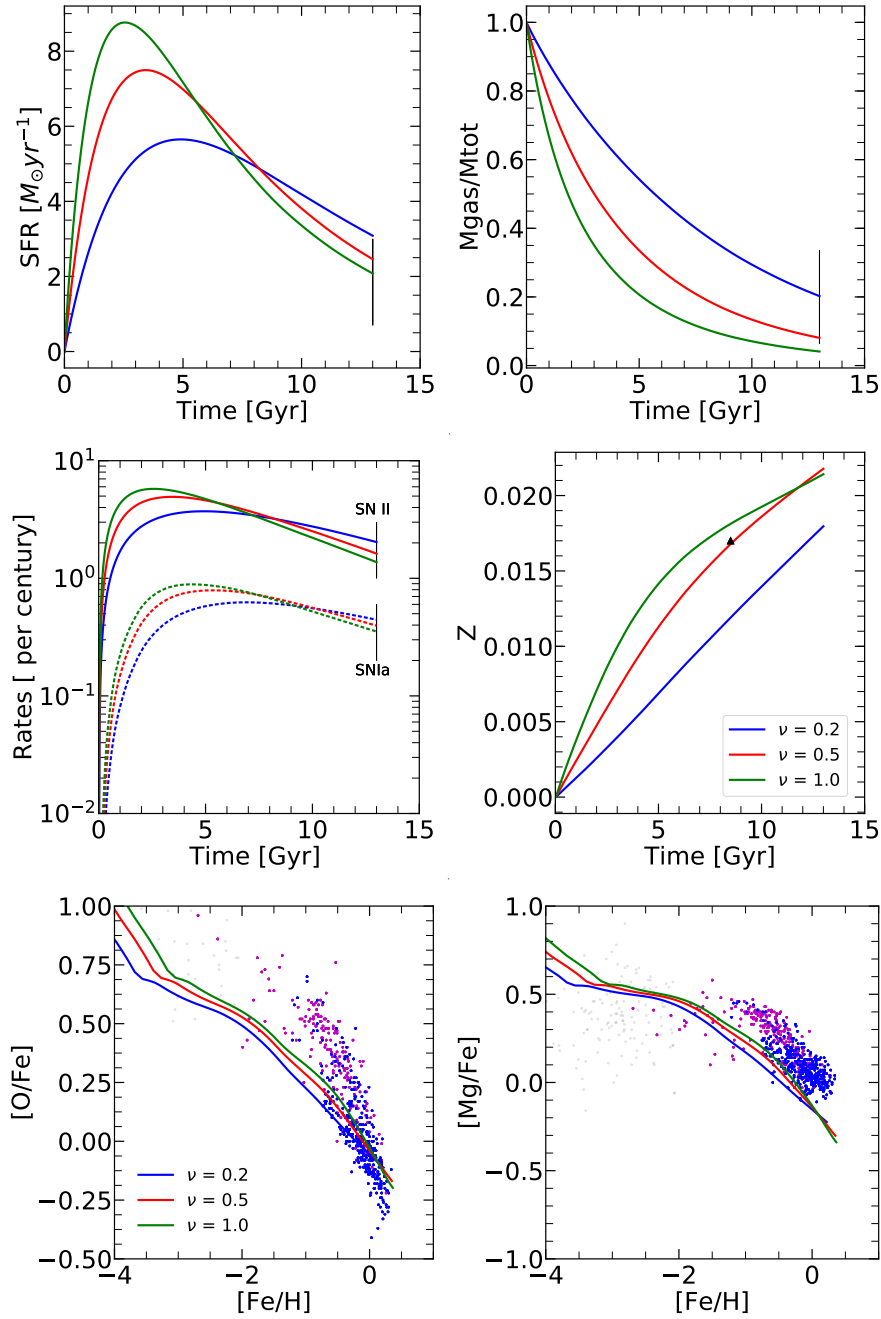


FIGURE 3.8: Same as Fig. 3.5 but changing the parameter that regulates the efficiency of star formation, ν . Values of $\nu=0.2, 0.5, 1.0$ are explored here, keeping the other parameters fixed to their reference values.

models where all the parameters are explored in suitable ranges. This grid will be used to find the model that best fit the observations discussed in Sect. 3.1.2.

3.3 The Library of Models

The library of models used in this work has been computed keeping in mind the vast range of the values of parameters of the CHE-EVO code described in the previous section. I computed a very large database of models with different combinations of these input parameters, with the following strategy. In the beginning, I adopted large parameter bin sizes, to get a broad picture of how the parameters shape the results of the chemical models. By a preliminary comparison of the results with the data, I picked up the more promising ranges of the parameters while other, that resulted in bad fits, could be neglected. This allowed me to optimize the range of parameters on which I then run new sets of models with finer parameter resolution. This search for the best fit models was then restricted to this final library of models. The list of all the values of the tested parameters is given in Table. 3.3.

As for the IMF, I considered IMF slopes between $x = 1.7$ (Kroupa et al. 1993) and $x = 1.3$ (Kroupa 2001), the latter being adopted also by Chabrier (2003). These values are those that provide the most accurate results in recent studies of the properties of the thin and thick discs (Grisoni et al. 2017, 2018).

To obtain the quantities $\dot{M}_{g,j}^{\text{FB}}$ of Eq. 3.1, I also used different the yields tables, following the discussion of Sect. 2.4. In total I tested five sets of yields, as listed in Table. 3.2:

- **MTW** combines AGB yields from M20 with yields of massive and very massive stars from TW;
- **KTW** combines AGB yields from K10 with yields of massive and very massive stars from TW;
- **R_r** adopts R18 yields for both AGB and massive stars, with explosion ejecta for the *rapid* case;

TABLE 3.2: Sets of chemical ejecta adopted in the chemical evolution models

label	AGB stars	massive stars	rotation	PPISN/PISN/DBH
MTW	M20	TW	No	Yes
KTW	K10	TW	No	Yes
R _r	R18	R18 _r	No	No
R _d	R18	R18 _d	No	No
MLr	M20	LC18	Yes	No

ν	ASNIa	k_{sch}	τ_{inf}
0.2	0.03	0.9	1.0
0.23	0.04	1.0	2.0
0.25	0.045	1.03	3.0
0.27	0.046	1.05	4.0
0.32	0.047	1.07	5.0
0.35	0.05	1.17	6.0
0.5	0.055		7.0
0.7	0.055		8.0
0.9	0.06		8.7
1.0	0.07		9.7
1.4	0.08		10.7
2.0	0.09		12.0

TABLE 3.3: The different values of the chemical evolution input parameters adopted in this work

- **R_d** adopts R18 yields for both AGB and massive stars, with explosion ejecta for the *delayed* case;
- **MLr** combines AGB yields from M20 with LC18 yields for rotating massive stars, averaged as a function of the metallicity following Prantzos et al. (2011).

At the end of the process we generated about 1300 models for each of the yield combination. In the next section I describe the method adopted to select the chemical evolution models that best reproduce the observations.

3.4 Method

Once I have obtained the whole database of models running our chemical evolution code with different input parameters and different yields, I analyse the models in the following way. I wrote a Fortran code that can read the output from CHE-EVO and the observed data, in our case taken from Bensby et al. (2014). As for the elemental abundances, the code transforms the mass abundances provided by CHE-EVO first in number abundances, both absolute and relative to the solar ones, and then into the usual abundance ratios, [Fe/H] [Mg/Fe], etc... I can also directly compare quantities like age, SFR, SN rate, gas fraction, global metallicity Z with the corresponding observations.

To evaluate the performance of a model in matching the observed abundance ratios, the code calculates a chi-square as follows:

$$\chi^2 = \sum_i (Y_{data}^i - Y_{mod}^i)^2 / N_{data} \quad (3.10)$$

where χ^2 is the variance of the data with respect to the model. Here Y_{data}^i are the median values of the data in selected bins of the abscissa, for example, [Fe/H];

Y_{mod}^i are the median values of the model data within the same abscissa bins used for the models; and N_{data} is the number of such bins.

A proper selection of the bins, allow us to follow and compare the path of the models in, e.g., the [O/Fe]vs. [Fe/H]diagram and to estimate the merit of the model.

We can use other datasets and the code can calculate the merit function according the provided data file. Furthermore, the code provides an estimate of the best model for every different element.

In our case, as I will show below, I chose the model which better reproduces the [O/Fe]vs [Fe/H]ratios. This choice is dictated by the following considerations. Oxygen is the most abundant among the metals. In general, it is about half the total metallicity. It is also mainly produced by massive stars which have short evolutionary timescales so that its production rate is strictly related to the current SNII rate and the recent SFR. An element with the same characteristics is Magnesium, which is also produced mainly in massive stars and for which there are in literature large observational databases. However, there is the long standing problem that the yields of Mg seem to be underestimated ([Timmes et al. 1995](#); [Portinari et al. 1998](#); [Prantzos et al. 2018](#)).

Finally, we note that, in the recent data of [Bensby et al. \(2014\)](#), where the thin and thick disc membership of individual stars has been derived on the basis of kinematic properties, the distinction between the two Galactic components is more evident in the [O/Fe] vs. [Fe/H] diagram, as compared to the other elements. In the following, I will investigate this feature in more detail, as discussed in the next chapters.

In the next chapter, I present the results of our models which best reproduce the Galactic thin disc and I move to the thick disc population later on.

Chapter 4

Chemical evolution of the thin disc

In this chapter I discuss the models of the Galactic thin disc.

4.1 Previous analyses of the Milky Way thin and thick discs

There have been in the past and in the more recent literature many attempts to explain the different chemical evolutionary paths of MW thin and thick discs and, in more generality, of its different components. The outcome of these studies is that the observed different chemical evolutionary paths are related to differences in the main physical processes that drive galaxy evolution, among which the most significant are the gas accretion time-scale and the star formation efficiency (Larson 1972; Lynden-Bell 1975; Pagel & Edmunds 1981; Matteucci & Greggio 1986b; Matteucci & Brocato 1990; Ferrini et al. 1994; Prantzos & Aubert 1995; Chiappini et al. 1997; Portinari & Chiosi 1999; Chiappini et al. 2001; Bekki & Tsujimoto 2011; Micali et al. 2013; Sahijpal 2014; Snaith et al. 2014; Grisoni et al. 2017; Grand et al. 2018). Other parameters, such as radial migration, may also have played an important role in generating the observed dichotomy between the thin and thick disc (Schönrich et al. 2010). Indeed, following the results of chemo-dynamical models, it has been suggested that thick disc stars may have originated in an inner region of the MW, characterized by an earlier and faster enrichment but then, they had time to migrate into the solar vicinity and become also kinematically hotter (e.g. Aumer et al. 2017; Schönrich & Aumer 2017). Under this hypothesis, these stars would be naturally characterized by chemical compositions and, in particular, levels of α -enhancement different from the native stellar populations of the solar neighbourhood.

More recently, the analysis of *Gaia* data (Gaia Collaboration et al. 2018), provided evidence that the peculiar chemical composition of the thick disc with respect to that of the thin disc, could have originated in an early merger between the MW and a satellite galaxy, the Gaia Enceladus Sausage galaxy (Belokurov et al. 2018; Helmi et al. 2018; Haywood et al. 2018).

Particularly successful in explaining the presence of distinct MW stellar components as well as the thick and thin disc dichotomy, have been the models built on the so-called *inside-out scenario* (Larson 1972; Matteucci & Francois 1989a;

Chiappini et al. 1997). Within this scheme, the formation of the different components is associated to distinct sequential main episodes of gas accretion (infall phases) that first rapidly accumulates in the central regions and then, more slowly, in the more external ones. As an example, the three-infall model, devised by Micali et al. (2013), is able to reproduce the abundance patterns of the MW halo, thick and thin disc at once. In this model, the gas accretion history is the sum of three main infall episodes of primordial gas, whose efficiencies peak at three different epochs and have different durations. The halo forms in the first episode which has the shorter timescale (0.2 Gyr) and lasts for about 0.4 Gyr and a star formation efficiency $\nu=2\text{Gyr}^{-1}$. The thick disc forms in a second episode characterized by a somewhat longer infall timescale (1.2 Gyr) and by the duration of about 2 Gyr with a star formation efficiency $\nu=10\text{Gyr}^{-1}$. Finally, the star formation continues in the thin disc with a longer infall timescale (6 Gyr in the solar vicinity) and is still continuing nowadays, with star formation efficiency $\nu=1\text{Gyr}^{-1}$. The [O/Fe] vs [Fe/H] the path is thus continuous across the regions populated by halo, thick and thin disc stars, as shown in Figure 5.

While in Micali et al. (2013) the chemical enrichment is continuous across the three different infall stages, Grisoni et al. (2017) devised also an alternative scheme where the thin and thick disc components evolve separately, in a parallel approach. In the parallel approach, the disc populations are assumed to form in parallel but to proceed at different rates. This alternative approach better reproduces the presence of the metal-rich α -enhanced stars in the [Mg/Fe] vs [Fe/H] diagram obtained with the recent AMBRE data (Mikolaitis et al. 2017; de Laverny et al. 2013). With their two-infall model, Grisoni et al. (2017) could not reproduce this population, unless assuming that these stars are the result of stellar migration (see their Figure 4). In their parallel approach, the gas infall exponentially decreases with a timescale that is 0.1 Gyr and 7 Gyr, for the thick and thin disc, respectively.

Following Grisoni et al. (2017), I will adopt a parallel scheme to discuss the observations of the MW thin and thick discs. However, I recall that our code is not as sophisticated as the one used by Grisoni et al. (2017). Effects of gas outflows are not yet taken into account and we do not consider the effects of a star formation threshold. These effects may affect both the predicted abundances and the duration of the star formation process. For example, in our case, the star formation process can be interrupted only by invoking the occurrence of a galactic wind at a certain time. Last but not least, we are using different yields. Thus, I expect that the parameters describing the gas infall and the star formation efficiency will not be identical to those used by Grisoni et al. (2017). I will thus perform a preliminary calibration of the code parameters on a few observed constraints of the Milky Way, as discussed below. Since these constraints are more obvious for the thin disc, because it is still an active component (i.e. it does not evolve passively), I begin the discussion with the thin disc, letting that of the thick disc to the next chapter.

4.2 Model constraints for the thin disc

The observed thin disc constraints that must be reproduced by our models are the following.

- *The current SFR of the MW.* To a large degree it corresponds to that the thin disc, and is estimated as $\text{SFR} = 0.65 - 3.0 M_{\odot} \text{yr}^{-1}$ (Robitaille & Whitney 2010).
- *The current gas fraction.* It is assumed to be $M_g / (M_g + M_s) \sim 0.2$ (Kubryk et al. 2015).
- *The current SNII rate.* We set $R_{\text{SNII}} = 2 \pm 1$ SNII event per century (Prantzos et al. 2011).
- *The current SNIa rate.* We set $R_{\text{SNIa}} = 0.4 \pm 0.2$ SNIa event per century (Prantzos et al. 2011).
- *The protosolar metallicity Z_{protoSUN} .* It represents the bulk metallicity of the molecular cloud out of which the Sun was born. It does not coincide with the current photospheric solar metallicity ($Z_{\odot} \simeq 0.014 - 0.015$), which is the result of chemical sedimentation effects over a time of about 4.6 Gyr (the present Sun's age). Here we adopt $Z_{\text{protoSUN}} = 0.017$, which is the initial metallicity of the PARSEC $1 M_{\odot}$ model that best reproduces the currently observed Sun's properties when using the Caffau et al. (2011) solar mixture (Bressan et al. 2012). Assuming an age of 13 Gyr for the formation of the Galaxy (e.g. Savino et al. 2020), it follows that the Galactic age at the birth of the proto-Sun is $t_{\text{protoSUN}} = 8.4$ Gyr. At this epoch, the metallicity in the solar vicinity is Z_{protoSUN} .

In addition to the constraints just mentioned above, we also require models to reproduce the observed [Fe/H] metallicity distribution function (MDF) of thin disc stars derived from the Bensby et al. (2014) data.

The evolution of the SFR, the gas mass fraction, the SNII and SNIa rates and the gas metallicity (Z) of the best models for the adopted yields sets are shown in Fig. 4.1. The corresponding MDFs are compared with that of the thin disc in Fig. 4.2. We now consider in more detail the results obtained with the individual yield combinations.

4.2.1 MTW yields

The selected model obtained with the MTW yield combination is shown in dark yellow in Fig. 4.1. The adopted parameters of this model, together with those of the other models, are shown in Table. 4.1. As seen in Fig. 4.1, this model reproduces fairly well all the aforementioned observational constraints, though the solar metallicity falls a bit below. However the gas fraction has been reproduced good with this model as shown in the upper right panel of Fig. 4.1. The comparison of the predicted MDF of the models with the observed one of thin disc stars

is shown in Fig. ???. In this figure we also plot the observed MDF of the thick disc to highlight its differences with that of the thin disc. The vertical bars in the figure mark the location of the median values of the distributions. The MTW model predicts a MDF that is slightly more metal-rich than the observed one but the median value, shown by the corresponding vertical bar, is very close to that of the observed distribution and significantly different than that of the thick disc. The IMF used to reproduce the observed constraints is a [Kroupa et al. \(1993\)](#) one with a slope of $x=1.5$ in the higher mass range and the upper mass limit of $120M_{\odot}$.

4.2.2 KTW yields

The model obtained with the KTW yields is shown in blue in Fig. 4.1. We have used the same parameters for chemical evolution as used in the MTW. The IMF used in this case is identical to that used in the MTW model. The differences which exist between the two model is due to the AGB yields and the different metallicities of yields used for the chemical evolution. Also, this model reproduces fairly well the above observational constraints; however, it should be noted that this model is not intended to replicate the observable constraints best, but the idea is to use the same parameters as MTW to highlight the differences between the two AGB yields if any, used in the two cases. In particular, this model very well replicates the median value of the observed MDF.

4.2.3 Rr and Rd yields

Similar good fits are also provided by models that use rapid or delayed [Ritter et al. \(2018\)](#) yields. [Ritter et al. \(2018\)](#) provides both AGB and massive stars yields in the mass range $1M_{\odot}$ - $25M_{\odot}$ for the metallicities $Z=0.0001, 0.001, 0.006, 0.02$. However, the model parameters are quite different from the other cases, as shown in Table 4.1. First, the upper mass limit, in this case, is $25M_{\odot}$. Second, since the Fe production by CCSN in these models is significantly higher than that of the other yield sets, in order to reproduce the observed $[Fe/H]$ MDF distribution and at the same time the initial metallicity of the Sun, we had to decrease the SNIa efficiency factor to $A_{SNIa}=0.025$ and to adopt a flatter IMF in the massive star regime. The models so obtained reproduce fairly well the observed constraints of Fig. 4.1, but their MDFs are about 0.1 dex more metal-rich than the observed one.

4.2.4 MLr yields

This set makes use of the yields from massive stars with rotation. The models with three different rotational velocities of LC18 are averaged as a function of the metallicity, as suggested by [Prantzos et al. \(2018\)](#). We have used the metallicities $Z=0.001, 0.006, 0.02$ in this case. The model is shown in dark green in Figs. 4.1 and ??. Even in this case, the adopted IMF of the best model is identical to that used in the MTW case. With $A_{SNIa}=0.06$ and $\tau_{inf}=3.4$ Gyr this model reproduces

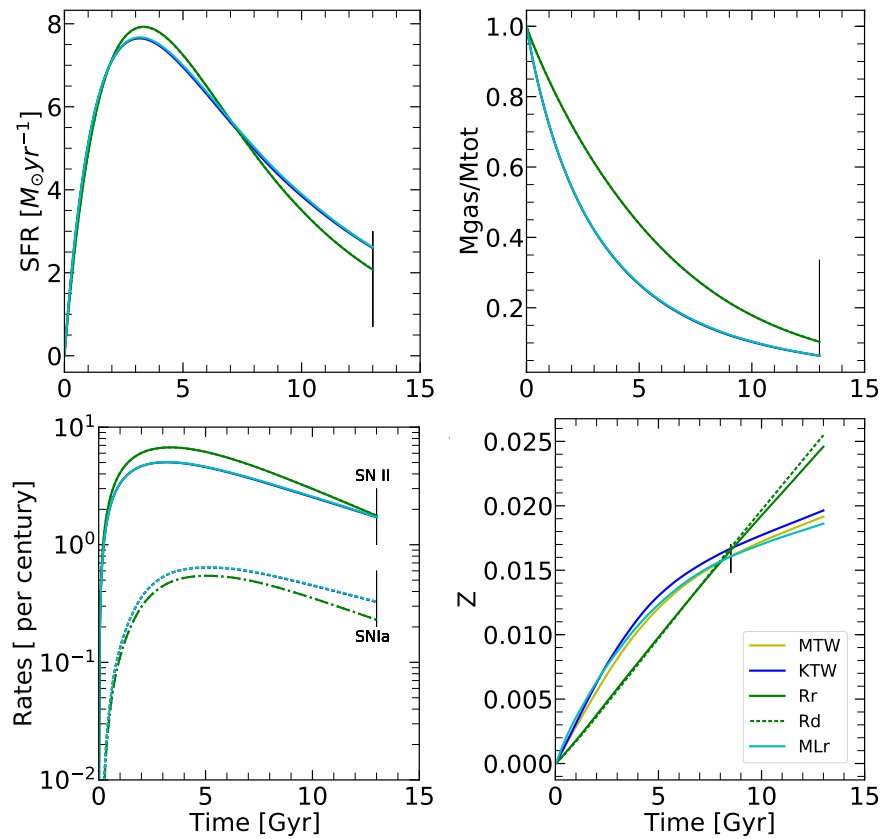


FIGURE 4.1: From upper left to lower right we show the evolution of the SFR [M_{\odot}/yr], gas fraction, SNII and SNIA rates per century and total gas metallicity of the best models computed using the MTW, KTW, Rr, Rd and MLr sets of yields. Vertical bars at an age of 13Gyr show their current estimated values. The solid triangle in the lower right panel marks the initial value of the solar metallicity resulting from the PARSEC calibration. The chemical evolution parameters of the models are listed in Table. 4.1

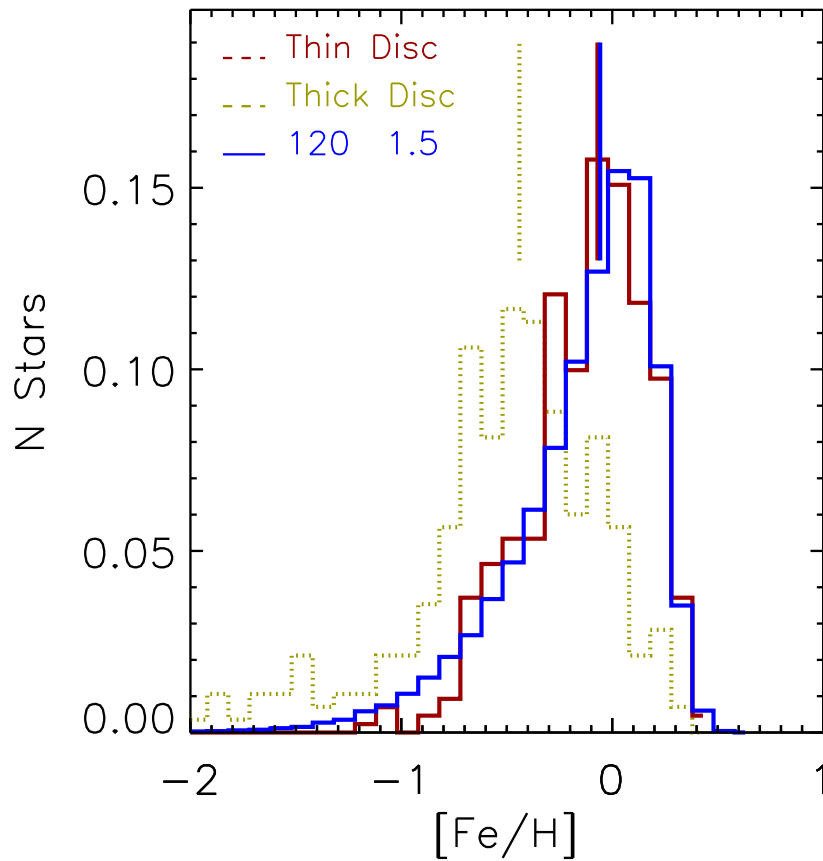


FIGURE 4.2: Observed $[\text{Fe}/\text{H}]$ distribution of thin disc stars (solid brown) and thick disc stars (dotted yellow). Superimposed are selected model of the thin disc for the cases MTW (blue). Vertical lines mark the median values of the distributions

very well the median value of the MDF of thin disc stars. Also the other constraints are fairly well reproduced including the solar metallicity at 8.5 Gyr.

In general, we may conclude from the previous discussion that with all the selected yield combinations, it is possible to find models that reproduce fairly well the observed constraints for the thin disc component of the MW as observed in the solar vicinity. Concerning the $[\text{Fe}/\text{H}]$ values, there is a tendency to slightly over-predict the number distribution at low metallicities (the so-called G-dwarf problem) and to reach slightly larger values than observed. The two effects certainly combine to reproduce quite well the observed median value, and better models could be obtained by pushing on the fine-tuning of the parameters. However, we note the discrepancies between the predicted and observed distributions of the thin disc component are much less than the differences between the thin and thick disc observed distributions. We thus accept our models as fair models for the thin disc and continue the exploration of the predicted abundance ratios.

4.3 Predicted Elemental abundances

In Fig. 4.3, we compare the elemental abundances predicted by the above models with those of individual stars of the thin disc. We show here only a few selected elements O, Mg, Si, and Ca and plot their $[\text{X}/\text{Fe}]$ vs. $[\text{Fe}/\text{H}]$ diagrams, from the top left panel to bottom right one, respectively. The observed thin disc stars (Bensby et al. 2014) are shown in blue in these figures. For comparison, we also show in the figure the data of thick disc stars (magenta) (Bensby et al. 2014) and low metallicity halo stars collected in literature (grey) (Gratton & Sneden 1988; McWilliam et al. 1995; Fulbright 2000; Carretta et al. 2002; Cayrel et al. 2003). We recall that all the data have been normalized according to the initial solar elemental abundances given by Caffau et al. (2011) which has been adopted in PARSEC.

4.3.1 MTW yields

This model is able to reproduce fairly well the observed trend in the $[\text{O}/\text{Fe}]$ diagram, going through the thin disc stars. Such small discrepancy should be attributed to the chemical yields from massive stars. In fact, in the COLIBRI models used here (M20 yields), TP-AGB stars produce a negligible amount of primary oxygen, as the chemical composition of the intershell is the standard one and it contains no more than 1% – 2% of ^{16}O (see, e.g. Herwig 2000, models without overshooting).

Taking the MTW model as representative of the main thin disc branch, we see that at decreasing $[\text{Fe}/\text{H}]$ the difference in $[\text{O}/\text{Fe}]$ between thin and thick disc stars increases. At $[\text{Fe}/\text{H}] \leq -1$ the thin disc branch disappears, and the MTW model approaches the lower boundary of the halo population.

Following the probability TD/D -criterion (Bensby et al. 2014), we note that a second, less populated, thin disc branch overlaps with the sequence of thick disc

stars in the same abundance diagram. Clearly, The MTW model is not able to reproduce this secondary branch.

Concerning the [Mg/Fe] ratio, the MTW model runs through the lower border of the thin disc data, showing a well-known difficulty likely related with the ^{24}Mg yields (Timmes et al. 1995; Portinari et al. 1998; Romano et al. 2010; Prantzos et al. 2018). The [Si/Fe] ratio is fairly well recovered by this model, while the [Ca/Fe] is under-produced.

4.3.2 KTW yields

This model behaves similarly to the MTW model for all the four abundance ratios. We recall that KTW and MTW models only differ for the AGB yields in use. Small differences appear at the lowest [Fe/H] values where the increase of KTW metallicity with time takes place somewhat faster than predicted by the MTW model (see Fig. 4.1 and the discussion in Sect 4.2). Since MTW and KTW models share the same chemical evolution parameters and massive star yields, differences in the trends of chemical species should be likely ascribed to reaching somewhat different metallicities at the same evolutionary time.

4.3.3 Rr and Rd yields

While successfully reproducing basic constraints of the MW thin disc, these models fail to recover the evolution of the selected abundance ratios (see Fig. 4.3). Even adopting a low SNIa efficiency parameter, models exhibit a substantial deficit in ^{16}O , ^{24}Mg , ^{28}Si and Ca relative to Fe. In the attempt to solve the discrepancy we explored a wide range of chemical evolution parameters, but we were unable to find better models than those shown in Figs. 4.1 and 4.3. The results worsen for the rapid case and, since the ratios $[\alpha/\text{Fe}]$ run much flatter than observed, we argue that the issue may be linked to the iron yields of CCSN. In fact, we find that at $Z_i < 0.02$, iron production by CCSNs predicted by R18 is significantly higher than in L18 explosive models (used in MTW, KTW and MLr), by a factor from two to four.

4.3.4 MLr yields

The MLr model reproduces fairly well the [O/Fe] data of the thin disc. The abundance of Mg is clearly under-predicted as already found by Prantzos et al. (2018) using the same yields for massive stars, while predictions for Si and Ca are able to populate the regions of both thin- and thick disc components. We note the MLr model shows a general tendency to produce abundance ratios running with slightly steeper slopes than observed.

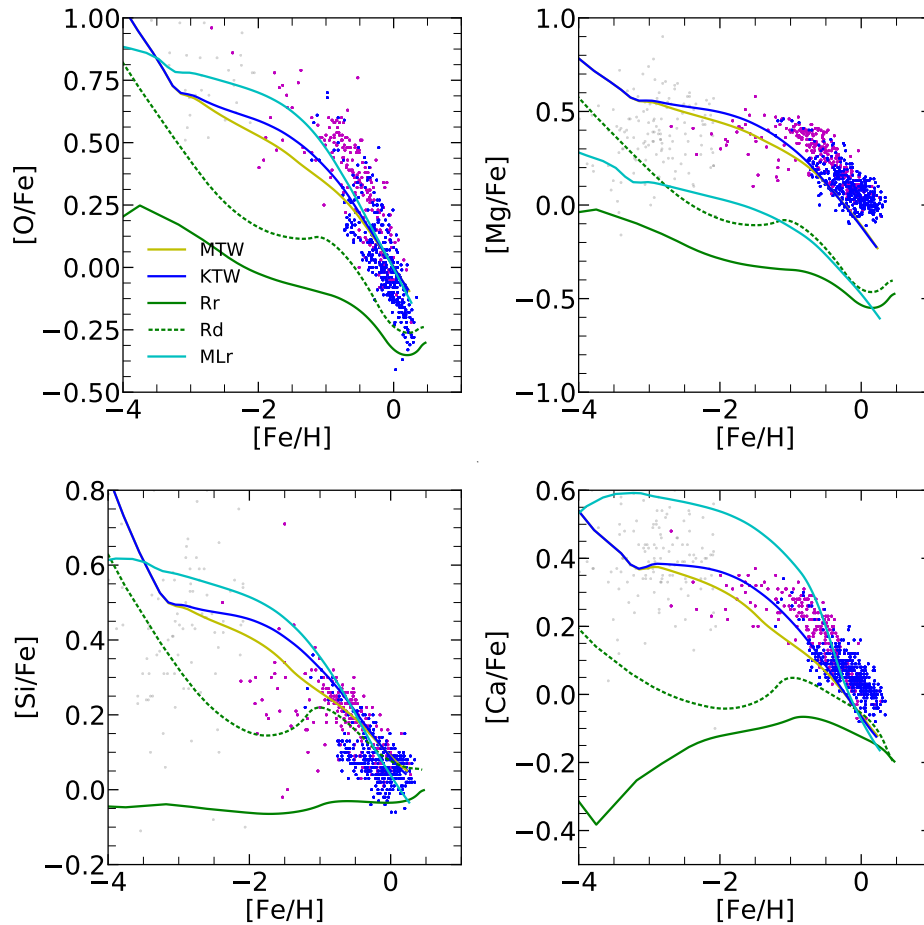


FIGURE 4.3: Comparison of the best models of Fig. 4.1 with selected observations of stars of the thin disc in the solar neighbourhood [Bensby et al. \(2014\)](#) (blue points). Also plotted are data of thick disc stars from the same author (magenta points). Grey dots represent a sample of metal-poor halo stars ([Gratton & Sneden 1988](#); [McWilliam et al. 1995](#); [Fulbright 2000](#); [Carretta et al. 2002](#); [Cayrel et al. 2003](#)).

TABLE 4.1: Parameters for the best model for each ejecta combination as given in Table. 3.2 and defined in Sect. 3.3.

Ejecta	Chemical param.				IMF	
	$\nu[\text{Gyr}^{-1}]$	k	$\tau_{inf}[\text{Gyr}]$	A_{SNIa}	$M_{UP}[M_{\odot}]$	x
MTW	0.8	1.0	6.0	0.04	120	1.5
KTW	0.8	1.0	6.0	0.04	120	1.5
R _r	0.4	1.0	3.0	0.025	25	1.3
R _d	0.4	1.0	3.0	0.025	25	1.3
MLr	0.8	1.0	6.0	0.04	120	1.5

4.4 Conclusions

From all the tests carried out with different combinations of chemical yields, we can draw a few conclusions. First, the chemical species discussed here are marginally dependent on the chemical yields of AGB stars, and therefore cannot be considered useful diagnostics for testing the goodness of low- and intermediate-mass evolutionary models. This is not surprising since we do not expect that AGB stars synthesize Fe and Ca, while they may be contributors of Mg isotopes, which are present both in the dredged material and involved in the Mg-Al cycle when hot-bottom burning is active in AGB stars with $M_i > 3\text{-}4 M_{\odot}$ (Slemer et al. 2017; Marigo et al. 2013; Ventura & D’Antona 2009). As discussed above, the production of some primary oxygen by AGB stars depends on the inclusion of convective overshoot at the boundaries of the pulse-driven convective zone (Herwig 2000), which applies to R18, but not to M20 and K10 yields. In the context of this work, the role of AGB stars as oxygen producers is not critical irrespective of the selected yield set. This reinforces the conclusion that we need to consider other more suitable elements, such as carbon and nitrogen, to compare and check different sets of AGB yields. An in-depth analysis of AGB yields is postponed to a dedicated future work.

It follows that the abundance trends investigated in this work are critically dependent on the chemical yields from massive stars. Therefore, the reader should keep in mind that, even when not explicitly stated, the discussion that follows mainly deals with the effects produced by chemical yields of stars with $M_i > 8M_{\odot}$.

Once the chemical evolution models are calibrated on a few basic observables of thin disc stars, it is possible to reproduce fairly well the enrichment paths of [O/Fe] and [Si/Fe] with most of the yield sets. As to the [Mg/Fe] ratio, we meet the long-lasting problem of underproduction found in most of the yield calculations (Timmes et al. 1995; Portinari et al. 1998; Romano et al. 2010; Prantzos et al. 2018), which appears somewhat less pronounced with the MTW yields. It is worth mentioning here that, among the recent yield calculations, only those by Nomoto et al. (2013) do not suffer of this problem.

As to the [Ca/Fe] the observations are better reproduced by massive star models with rotation. Using the R18 yields, none of the elemental ratios is well reproduced. The discrepancy is likely due to the high Fe yields in some of the [Ritter et al. \(2018\)](#) explosion models, which makes it hard to recover the observed [α /Fe] ratios at a given [Fe/H].

We finally note that there are stars belonging to the thin disc, according to the kinematical criterion, that have high [O/Fe] values and fall in the region of the thick disc stars. Our thin disc models do not reproduce such stars. However, it is not clear whether this behaviour is real or, rather, the kinematical parameters of these stars varied in such a way that they are now classified as thin disc members. Indeed, these trends could be explained by the stellar migration process ([Schönrich et al. 2010](#)).

Chapter 5

Chemical evolution of thick disc

In this chapter, we discuss the chemical evolution of the Galactic thick disc. We recall that the difference between the thick and the thin disc populations is quite evident in the [O/Fe] vs. [Fe/H] evolution, taken from the data provided by [Bensby et al. \(2014\)](#). Here, taking the oxygen as our reference element, we will discuss possible explanations of these important differences in the chemical evolution.

5.1 Introduction

From the individual stellar ages provided by [Bensby et al. \(2014\)](#) we have already seen that the thick disc is on average older than the thin disc. At the same time in the [O/Fe] vs. [Fe/H] diagram of Fig. 5.3 we can see that the stars of the thick disc (plotted in magenta colour) are more α -enhanced than those of the thin disc (plotted in blue color).

The models adopted for the thin disc stars are clearly not able to account for the [O/Fe] enrichment history of thick disc stars. In particular successful models for the Galactic thick disc should be able to produce a larger oxygen enrichment at a given iron abundance.

As already discussed in Chapter 4 the dichotomy between thick and thin discs has been the subject of many previous studies. Among others, we have illustrated the three infall model developed by [Micali et al. \(2013\)](#) and the parallel model developed by [Grisoni et al. \(2017\)](#). I will use here their results as a guide to search for chemical evolution models that are able to reproduce the observations of the thick disc.

In the three infall model of [Micali et al. \(2013\)](#), the thick disc formation, in the second infall, the episode is simulated adopting an infall timescale $\tau_{inf}=1.2$ Gyr and a star formation efficiency $\nu=10\text{Gyr}^{-1}$. The peak epoch of the gas accretion, roughly corresponding to the end of the thick-disc phase, is set at $t_{max_T}=2$ Gyr. The star formation then continued in the third infall episode that was responsible for the thin disc formation. Instead, in the parallel model, [Grisoni et al. \(2017\)](#) adopted a very short infall timescale $\tau_{inf}=0.1$ Gyr and a star formation efficiency $\nu=2\text{Gyr}^{-1}$.

By adopting such a short τ_{inf} in my models the gas fraction left after 2 Gyr is about 10% but, the resulting MDF distribution shows a clear excess below [Fe/H] ~ -1 , with respect to the observed one. On the other hand, adopting a larger

TABLE 5.1: Adopted parameters for the thick disc models

Model	Yields	Chemical param.				IMF	
		$\nu[\text{Gyr}^{-1}]$	k	$\tau_{inf}[\text{Gyr}]$	A_{SNIa}	$M_{UP}[M_{\odot}]$	x
TD1	MTW	1.4	1.0	0.5	0.04	120	1.5
TD2	MTW	1.4	1.0	0.5	0.04	120	1.7
TD2	MTW	1.4	1.0	0.5	0.04	200	1.7
TD3	MTW	1.4	1.0	0.5	0.04	200	1.4

$\tau_{inf}=0.5$ Gyr and $\nu=1.4\text{Gyr}^{-1}$ the excess becomes acceptable, but the residual gas fraction rises to about 20%. The parameters of this model, named TD1 are listed in Table 5.1. In order to fit the high $[\text{Fe}/\text{H}]$ tail of the observed MDF, shown in Figure 5.1, I had to include a sort of galactic wind to expel this residual gas from the thick disc, at an epoch of $t_{GW}=2.5$ Gyr. While this assumption is introduced to cope with the simplicity of our chemical evolution code, we note that t_{GW} corresponds to the epoch of the end of the second infall episode in the [Micali et al. \(2013\)](#) model.

The $[\text{O}/\text{Fe}]$ vs. $[\text{Fe}/\text{H}]$ and $[\text{Mg}/\text{Fe}]$ vs. $[\text{Fe}/\text{H}]$ abundance patterns obtained with model TD1, are shown in Figure 5.2. We note that model TD1 is able to fit the observed region occupied by thick disc stars but, the slope is different from the observed one. In the $[\text{O}/\text{Fe}]$ vs. $[\text{Fe}/\text{H}]$ diagram, it underestimates the high $[\text{O}/\text{Fe}]$ values at low $[\text{Fe}/\text{H}]$ and, it overestimates the low $[\text{O}/\text{Fe}]$ values at high $[\text{Fe}/\text{H}]$. This model is, however, able to reproduce the region occupied by the most metal poor stars, likely belonging to the halo population, that is not discussed here. In the $[\text{Mg}/\text{Fe}]$ vs. $[\text{Fe}/\text{H}]$ diagram, the predicted slope is similar to the observed one, but the bulk of the data with $-1 \leq [\text{Fe}/\text{H}] \leq -0.5$ are not well reproduced. Furthermore, in this panel, almost all the halo stars fall below the model.

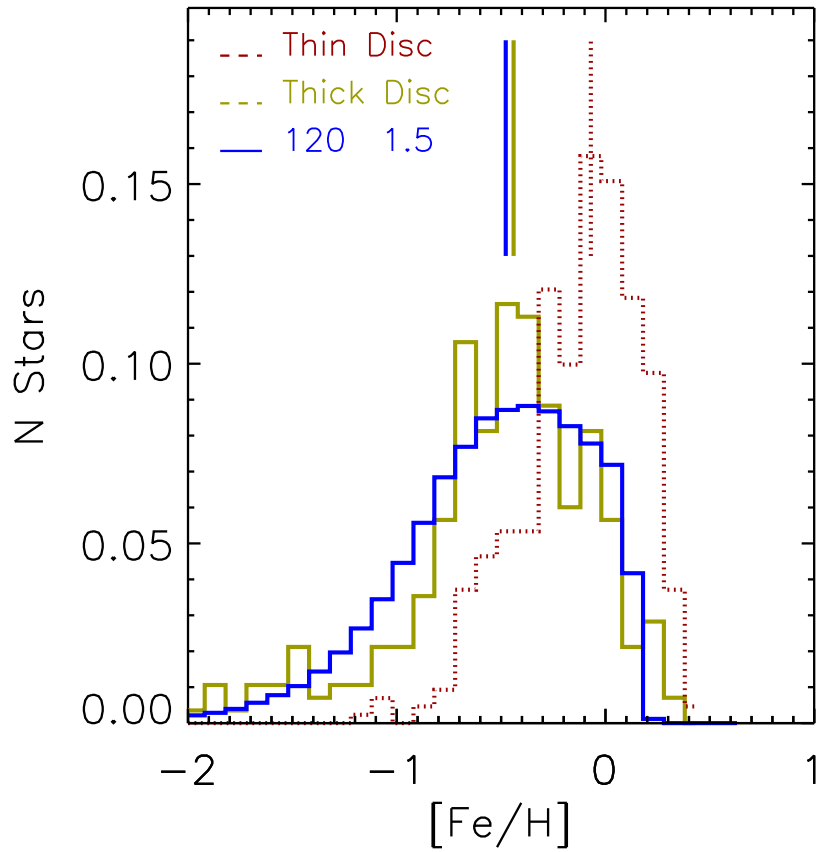


FIGURE 5.1: Observed $[\text{Fe}/\text{H}]$ distribution of thin disc stars (solid yellow) and thick disc stars (dotted brown). Superimposed is a selected model of the thick disc for the case MTW with $M_{\text{UP}} = 120 M_{\odot}$ and $x = 1.5$ (blue). Vertical lines mark the median values of the corresponding distributions.

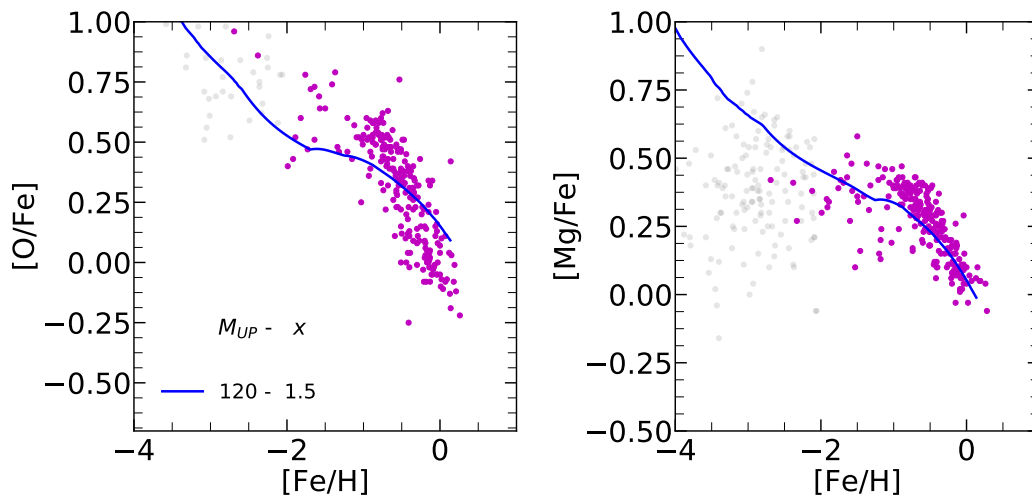


FIGURE 5.2: Comparison of the observed $[\text{O}/\text{Fe}]$ and $[\text{Mg}/\text{Fe}]$ and vs. $[\text{Fe}/\text{H}]$ ratios of the thick disc (magenta dots) with those predicted model TD1.

5.2 Effects of Rotation

Recent stellar evolution model calculations have shown that the chemical mixing induced by rotation is one of the mechanism that may increase the yields of oxygen, and other heavy elements, in massive stars [Limongi & Chieffi \(2018\)](#). Thus a plausible possibility could be related to the yields themselves and their dependence on stellar rotation, as recently suggested by [Romano et al. \(2019, 2020\)](#). In support of this indication, we recall that we have already seen that yields including stellar rotation, used e.g. in model MLr and Klr are able to produce steeper slopes in the $[\text{O}/\text{Fe}]$ vs. $[\text{Fe}/\text{H}]$ diagram, similar to the ones observed for the thick disc stars.

In our previous investigation of the thin disc stars, we have used a model that adopts average yields from sets of different rotation rates, the MLr and Klr model. To investigate the effects of rotation we thus start from this model and calculate new chemical evolution models by changing only the [Limongi & Chieffi \(2018\)](#) yields. We use their yields for the three different initial rotational velocities separately, $V_{\text{rot}} = 0$, $V_{\text{rot}} = 150$ and $V_{\text{rot}} = 300 \text{ km s}^{-1}$. This allows us to highlight the effects of rotation alone since in all simulations we adopt the same chemical evolution and IMF parameters of the MLr model. The results of these calculations are plotted in Fig. 5.3, limited to the $[\text{O}/\text{Fe}]$ ratio. We see that using yields from stars with higher rotational velocity we obtain higher $[\text{O}/\text{Fe}]$ ratios. This simply reflects the fact that, at increasing V_{rot} , massive stars produce larger amount of oxygen (see Figs. 2.7-2.9), while iron, being mainly contributed by SNIa, is barely changed.

Fig. 5.3 shows that enhancing the fraction of stars with high rotational velocity may explain the observed higher $[\text{O}/\text{Fe}]$, especially at metallicities $[\text{Fe}/\text{H}] \lesssim -1$. A similar experiment has also been done by [Prantzos et al. \(2018\)](#) who invoked the

existence of a correlation between metallicity and rotation. Looking at Fig. 5.3, we may see that the non rotating model computed with [Limongi & Chieffi \(2018\)](#) yields fits the lower envelope of the thin disc stars, of some thick disc outliers at $[\text{Fe}/\text{H}] \sim -2$ and of the few halo stars with $[\text{Fe}/\text{H}] < -2$. By increasing the rotational velocity the models shifts toward higher $[\text{Fe}/\text{H}]$ values. In particular using the model computed adopting the averaged yields obtained from the three different rotational velocity values (cyan line, [Prantzos et al. \(2018\)](#)), our model fits the border between thin and thick disc stars. Then, by further increasing the rotational velocity, all the thick disc stars can be fitted. These models are also able to reproduce the observed $[\text{O}/\text{Fe}]$ of the halo stars. In this experiment we used a model computed to fit the disc stars, i.e. model MLr, with a canonical IMF and an extended gas infall phase with $\tau_{inf} = 6 \text{ Gyr}$ $v = 0.8 \text{ Gyr}^{-1}$. It is thus clear that it seems possible to reproduce also the other MW components, by adopting yields computed for suitable rotational velocities. The fact that to reproduce the MW thick disc stars requires higher than average rotational velocities, is in very good agreement with recent $\text{H}\alpha$ or CO detection of highly star forming fast rotating massive thick discs in high redshift ($z \sim 0.67 - 2.6$) galaxies ([Wisnioski et al. 2015](#); [Wuyts et al. 2016](#); [Genzel et al. 2017](#)). Observations further indicate that discs are gravitationally unstable and thus they could be feeding the growth of the central massive bulges ([Genzel et al. 2020](#)), thus contributing to the gas exhaustion.

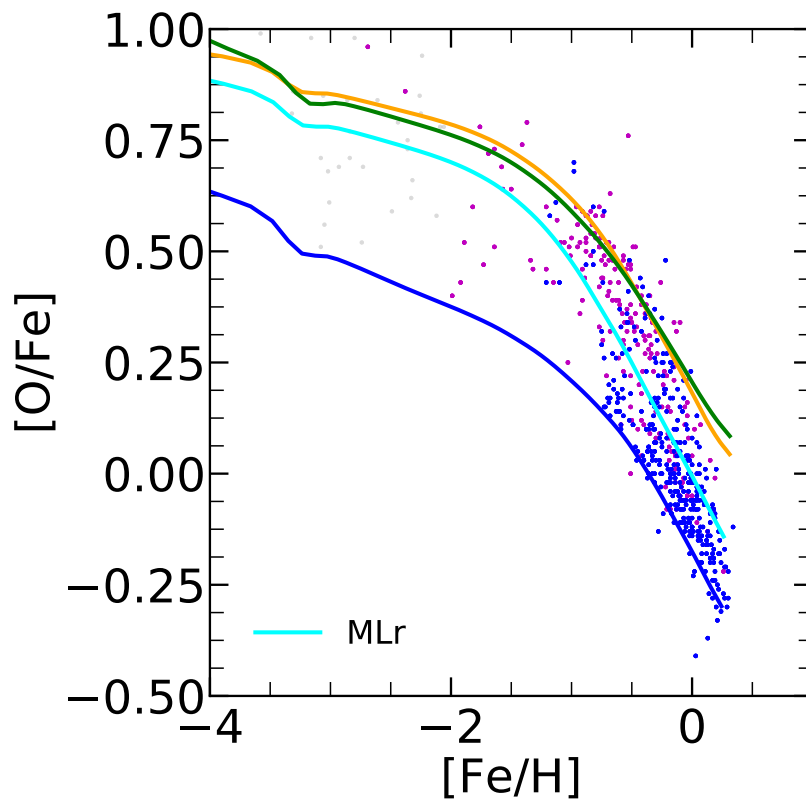


FIGURE 5.3: $[O/Fe]$ vs. $[Fe/H]$ abundances predicted by massive star models without and with rotation. The blue, orange and green lines refer to Limongi & Chieffi (2018) yields for initial rotational velocities $V_{\text{rot}}=0$, $V_{\text{rot}}=150$ and $V_{\text{rot}}=300$ km/s, respectively. The cyan line represents the MLr model with rotation-averaged yields.

5.3 Effects of a top heavy IMF

In the above sections we have been using a canonical IMF, i.e. an IMF with a slope in the massive star range between the typical values of $\alpha=1.7$ (Kroupa et al. 1993) and $\alpha=1.3$ (Kroupa 2001; Chabrier 2003). In the recent years, however, there was mounting evidence that the IMF could change, being different in different environments. There have been claims that local ellipticals, thought to be the descendants of high $z \geq 2$ star-forming systems, are characterized by a bottom-heavy IMF, as supported by observations of the strengths of gravity sensitive narrow band integrated indices (van Dokkum & Conroy 2012; van Dokkum et al. 2017). On the contrary, recent investigations of the isotopic abundances of CNO elements in starburst galaxies find strong evidence that the low O^{16}/O^{18} abundance ratios observed in starburst galaxies cannot be produced without assuming a top heavy IMF (Romano et al. 2017). Additional evidence for a top heavy IMF comes from studies focussed on young super star clusters (Evans et al. 2010; Walborn et al. 2014; Schneider et al. 2018; Crowther 2019; Crowther et al. 2016) and on the identification of massive stellar black holes hosted in binary systems (Abbott et al. 2016; Abbott et al. 2020; Spera & Mapelli 2017; Spera et al. 2015). This piece of evidence points to an IMF that extends up to VMO either as an original top-heavy IMF or by virtue of early efficient merging in binary systems (Senchyna et al. 2020). Furthermore, if massive young star clusters possess a top heavy IMF, while less massive cluster have a steeper IMF then, because the star cluster mass distribution gives more weight to the low mass ones, the integrated IMF in galaxies (IGIMF), could be steeper than the stellar IMF within each single star cluster (Kroupa & Weidner 2003; Weidner & Kroupa 2005). More recent studies have also found evidence for a flattening of the IMF (Kroupa 2008; Marks et al. 2012; Hosek et al. 2019) at decreasing metallicity and increasing star formation rate. Using all the above information, Jeřábková et al. (2018) performed a thorough analysis of the impact of metallicity and star formation rate on the time-dependent IGIMF. According to this analysis, galaxies with metallicity $[Fe/H] < 0$ and $SFR > 1$ /yr possess a top heavy and bottom light IGIMF, as compared to the canonical one. Instead, regardless of the metallicity, in galaxies with lower SFR the IGIMF becomes top light, i.e. steeper than the canonical one. When $[Fe/H] > 0$, the IGIMF can become bottom heavy regardless of the SFR. This kind of IMF well explains all the observational evidence discussed before.

Based on all the above considerations, I suggest that another viable explanation for the different $[O/Fe]$ evolution of thin- and thick disc stars could be linked to different IMFs of the two populations. In particular, we have already noted that the most massive stars that end their life as PISN may produce large amounts of oxygen. At the same time, they may produce also large amounts of iron and, the relative proportions between the ejecta of these two elements depend significantly on the initial stellar mass.

To investigate this aspect, we make use of our new MTW set of yields, which includes also the chemical contributions of VMO, from both stellar winds and PPISN/PISN explosions. This gives us the possibility to explore the effects of

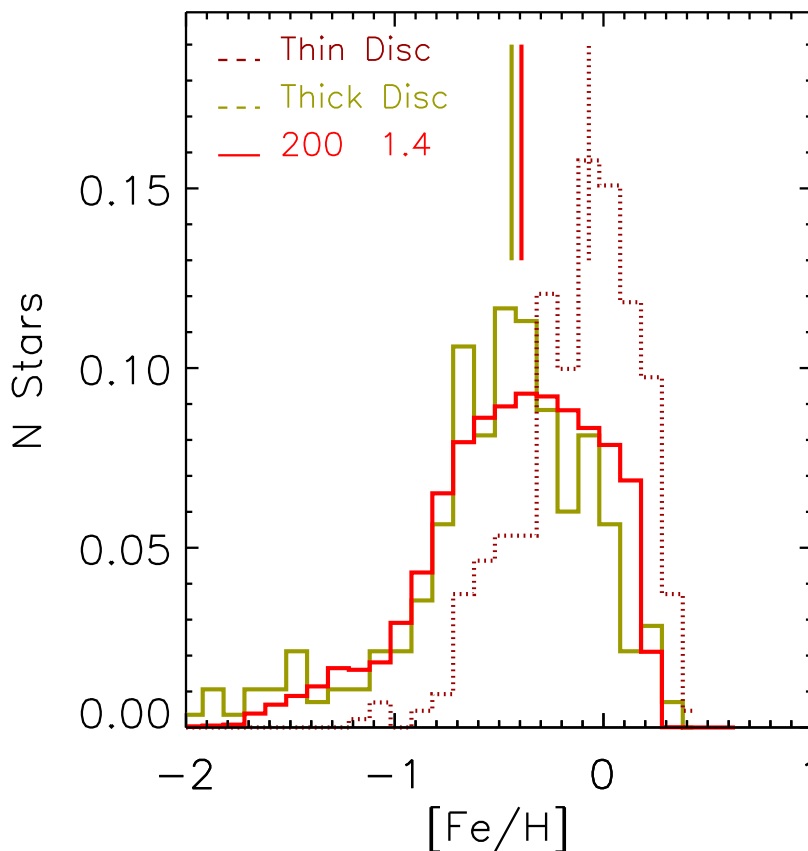


FIGURE 5.4: Observed $[\text{Fe}/\text{H}]$ distribution of thin disc stars (dotted brown) and thick disc stars (solid yellow). Superimposed are the model of the thick disc with MTW yields computed with $M_{\text{UP}} = 200 M_{\odot}$ and $x = 1.4$ (red). Vertical lines mark the median values of the distributions

changing both the IMF exponent x (for $M_i > 1 M_{\odot}$), and the upper mass limit M_{UP} , that can be pushed up to $350 M_{\odot}$.

As for the chemical evolution parameters I adopt models similar to model TD1 and I change only the IMF parameters. A new model, TD2, is calculated with a (Kroupa et al. 1993) IMF. This model is meant to see the effects of steepening the IMF. Other two models are constructed with $M_{\text{UP}} = 200 M_{\odot}$ and an upper mass range slope of $x = 1.5$ (model TD3) and $x = 1.4$ (model TD4), respectively. The MDF of model TD4, which is the one with the top heavier IMF, is shown in Figure 5.4. As in the case of model TD1, in order to fit the high $[\text{Fe}/\text{H}]$ tail of the observed MDF, I had to include a galactic wind to expel this residual gas from the thick disc, at an epoch of $t_{\text{GW}} = 2.5$ Gyr.

The predicted MDF distribution is very similar to the one of the model TD1, shown in figure 5.1. However, we note here that, with a faster enrichment produced by a top heavier IMF, the discrepancy of the excess of stars at low metallicity has

now disappeared.

The abundance patterns of thick disc stars predicted by these new models are compared with observations in the $[O/Fe]$ and $[Mg/Fe]$ vs. $[Fe/H]$ diagrams shown in Figs. 5.5 and 5.6, respectively. We note that, in the $[O/Fe]$ vs. $[Fe/H]$ diagram, model TD2, with $x=1.7$, runs below model TD1, eventually being able to reproduce the branch with low $[O/Fe]$ ratios at $[Fe/H] = 0$. Models TD1 and TD2 are able to reproduce the observed halo stars. Instead models TD3 and, especially TD4, run almost above the bulk of α rich thick disc stars, indicating that VMO may significantly contribute to the α enrichment. These two models, instead, are not able to reproduce the observed location of halo stars, because at these low metallicities VMO become an important source of Fe through the explosion of the most massive PISNe (Fig. 2.7).

Concerning the evolution of the $[Mg/Fe]$ vs. $[Fe/H]$ ratios we note that the only model that is able to reproduce well the observations of the thick disc stars is model TD4. In contrast, Model TD1, TD2 and TD3 run along the lower envelope of the thick disc data, for $[Fe/H] > -1$. For $[Fe/H] \leq -1$, the magnesium data show a significant dispersion that increases at decreasing metallicity. It is interesting that, in this diagram, the models that account for PISNe could well explain the observed presence of low $[Mg/Fe]$ stars while, models that do not include PISNe, run just over the high $[Mg/Fe]$ ratio stars. In these very early stages of the thick disc chemical evolution, the models are able to reproduce the observed α -poor (Mg) stars, for instance, those with $[Mg/Fe] \sim 0.2$ at $[Fe/H] \lesssim -2$ (see Fig. 5.6).

In this respect, I note that PISNe can contribute significantly to the α -elements up to a metallicity $Z_i \sim 0.006$, provided that a suitable IMF is selected. At this metallicity, only low mass PISNe are produced, because the mass loss rates are becoming significant. These PISNe are not important contributors to Fe. Indeed, models TD3 and TD4 show an abrupt rise of the $[O/Fe]$ and $[Mg/Fe]$ ratios at $[Fe/H] \approx -1.5 - -2$, depending on the IMF exponent. This is where the Fe contribution of PISNe ceases.

Finally we note that PISNe may also help in solving the issue of Mg underprediction present in most of the published yields tables (Timmes et al. 1995; Portinari et al. 1998; Prantzos et al. 2018).

In conclusion, our analysis shows that IMF variations, not only in terms of slope but, more importantly, of M_{UP} , may significantly affect the predictions of chemical evolution models.

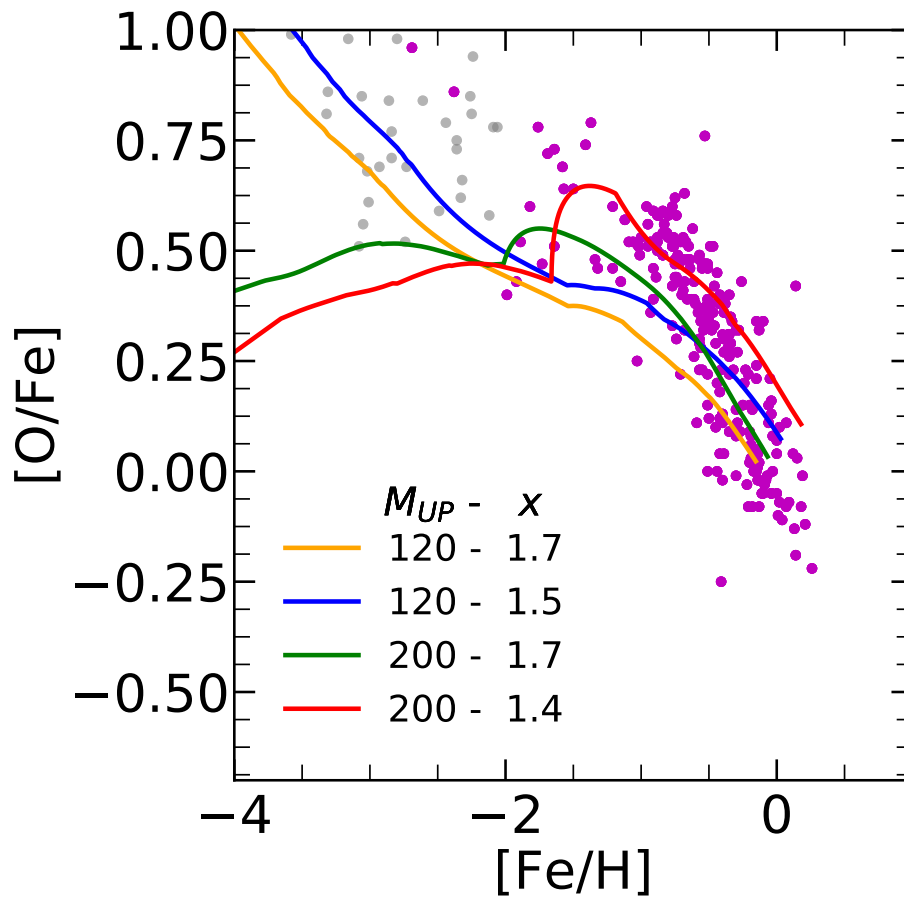
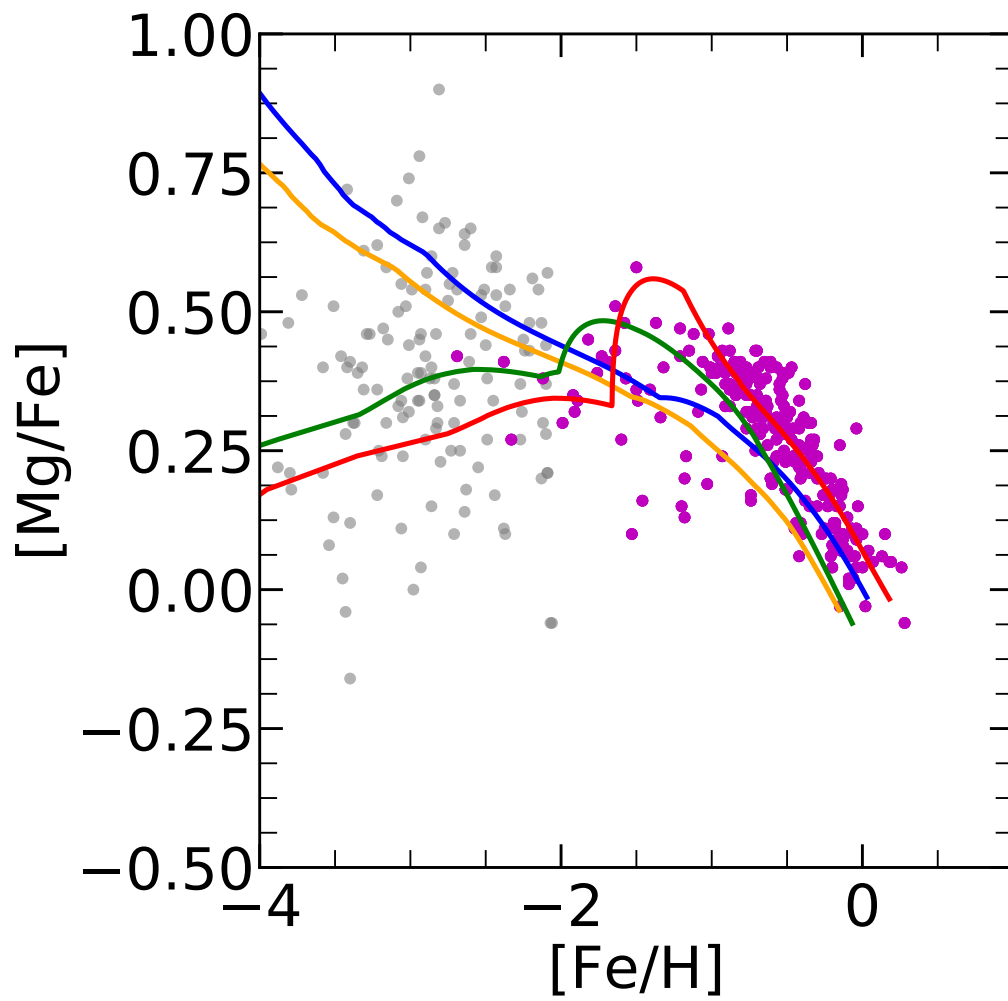


FIGURE 5.5: Comparison of the observed [O/Fe] vs. [Fe/H] ratios of the thick disc (magenta dots) with those predicted by models with different IMF parameters of Table ???. We see that increasing M_{UP} , so as to include the contributions of VMO (winds, PPISN and PISN), thick disc stars can be reproduced pretty well. Moreover, changing both the IMF slope and M_{UP} , different populations can be recovered.

FIGURE 5.6: Same as in Fig. 5.5, but for $[Mg/Fe]$.

5.4 Conclusions

Thick disc stars exhibit a $[O/Fe]$ vs. $[Fe/H]$ pattern different from that of the thin disc stars, characterised by a steeper slope and a larger degree of α -enhancement, with higher $[O/Fe]$ ratios. This feature is much less evident in the $[Mg/Fe]$ diagram. None of the chemical evolution models calibrated on the thin disc is able to reproduce the $[O/Fe]$ trend of the thick disc. All predicted trends remain below the observations. As already discussed in Chapter 4 the dichotomy between thick and thin discs has been the subject of many previous studies that identified its origin in the difference of two main physical processes that drive galaxy evolution, the gas accretion time-scale and the star formation efficiency (Larson 1972; Lynden-Bell 1975; Pagel & Edmunds 1981; Matteucci & Greggio 1986b; Matteucci & Brocato 1990; Ferrini et al. 1994; Prantzos & Aubert 1995; Chiappini et al. 1997; Portinari & Chiosi 1999; Chiappini et al. 2001; Bekki & Tsujimoto 2011; Micali et al. 2013; Sahijpal 2014; Snaith et al. 2014; Grisoni et al. 2017; Grand et al. 2018). Particularly illuminating in this respect are the works by Micali et al. (2013) and Grisoni et al. (2017). In the three-infall model by Micali et al. (2013) the gas accretion history is the sum of three main infall episodes of primordial gas, whose efficiencies peak at three different epochs and have different durations. In particular, the halo forms in the first episode in a very short timescale of about 0.4 Gyr and a star mild formation efficiency $\nu=2\text{Gyr}^{-1}$. The thick disc forms in a second rapid infall episode characterized by a somewhat longer timescale (2 Gyr) with a significantly higher star formation efficiency $\nu=10\text{Gyr}^{-1}$. Finally the thin disc has the longer infall timescale (6 Gyr in the solar vicinity) and its SF activity is still continuing nowadays, with a relatively lower star formation efficiency $\nu=1\text{Gyr}^{-1}$. The model by Grisoni et al. (2017) adopt a parallel approach, in which thick and thin disc populations are assumed to form in parallel but to proceed at different rates. The gas infall timescale is similar to the ones used by Micali et al. (2013). Both models were successful in explaining the formation of the MW stellar components, and I have used the suggested timescales in my parallel model to reproduce the thick disc.

I have thus shown that, adopting a mild star formation efficiency $\nu=1.4$ and a relatively short infall timescale $\tau_{inf}=0.5$ with a canonical IMF $M_{UP}=120$ and $x=1.5$ (Modell TD1) I can also obtain, with the MTW yields, a fairly good model for the thick disc. The MDF is well reproduced provided the gas is expelled from the thick disc at a galactic time of about 2.5 Gyr. Another way to reproduce the observed abundances of the thick disc is to consider yields from fast rotating stars (Limongi & Chieffi 2018; Romano et al. 2019). In this regard, our analysis shows that, using the yields from fast rotating massive stars, the chemical evolution models enter the region populated by thick disc stars. Furthermore, we note that, by using yields with initial rotational velocity above 150 km/s, does not produce a significant variation in the chemical evolution models. Conversely, using averaged rotation yields (Prantzos et al. 2018) the calibrated model places in between thin and thick disc stars and models that use yields for zero rotational velocity run on the lower envelope delimited by thin disc stars. An interesting property of these

models is that, by adopting the model parameters of the thin disc, one can reproduce all the other components (halo stars included) by increasing only the fraction of rotating stars. This in fact may give rise to a degeneracy between some chemical evolution parameters (τ_{inf} and ν) and the stellar rotational velocities. Finally, motivated by the fact that, in recent years, there has been growing evidence for a top heavy IMF, in particular in metal poor and highly star forming systems (Marks et al. 2012; Jeřábková et al. 2018) I tried thick disc models with a higher M_{UP} . This allows me to check the effects of analysing the effects of a top heavy IMF where, consistently with observations, M_{UP} may be significantly larger than the value usually adopted. With the MTW yields I can check the possible effect of very massive objects, in particular of PISNe. To my knowledge, this has never been done before. Using the same chemical evolution parameters of model TD1, I computed other three models, one with a steeper IMF ($x=1.7$) and other two with $M_{UP} = 200$ and $x=1.7$ and 1.4 respectively. The latter two models better reproduce the thick disc observations of in the $[O/Fe]$ vs. $[Fe/H]$ diagram. However, they fail to reproduce the low metallicity halo stars, because PISNe produce also large amount of Fe. The situation significantly improves when we consider the $[Mg/Fe]$ vs. $[Fe/H]$ diagram. In this case the Mg produced by PISN drives the models into the region populated by the data of thick disk stars. At the same time the Fe contribution at lower metallicities ($[Fe/H] \leq -2$), allow the models to reproduce the observations of halo star in this region of the diagram. Halo stars in the $[Mg/Fe]$ vs $[Fe/H]$ diagram show a large dispersion that is reproduced by our models, if we allow different kinds of IMF.

The models show that PISNe affects more the low metallicity stars than the more metal rich ones. Thus they should affect the halo component, that has not been directly analysed here, even if some hints have been discussed in relation to the early evolution of the thick disc models. However, the different results obtained when considering the data concerning the two different element ratios, $[O/Fe]$ or $[Mg/Fe]$, do not allow us to draw firm conclusions on the effects of PISNe at very low metallicity. Moreover MTW yields show that the effects of PISNe on oxygen and magnesium can be seen up to $Z_i = 0.006$, i.e. the metallicity of the Large Magellanic Cloud. We confirm that the comparison with the thick disc data show that their effect could be significant.

In conclusion we have seen that, though the main driver for the chemical evolution of the thick disc are the timescale and the efficiency of star formation, as already outlined in many previous analyses, from the point of view of stellar yields we confirm that rotation may play a significant role and we also show that PISNe may have a non negligible effect.

In the light of these results, we may reasonably expect that data at very low metallicity, which actually exist for nearby extremely metal-poor galaxies (Kojima et al. 2020a), might host the chemical signature of very massive stars, and that would witness if they played a key role in the early phases of galaxy evolution. This is the subject of the following chapter.

Chapter 6

The impact of PISNe in the chemical evolution of extremely metal-poor galaxies

6.1 Introduction

The study of metal-poor galaxies is of great interest because it can help in shedding light on early galaxy evolution since metal-poor galaxies are expected to be a significant baryon component of the early universe.

Extremely metal-poor galaxies (EMPGs) are defined to have metallicities less than $12+\log(\text{O}/\text{H})=7.69$ (Kunth & Östlin 2000; Izotov et al. 2012; Isobe et al. 2020), being $12+\log(\text{O}/\text{H})=8.69$ the solar metallicity (Asplund et al. 2009). Even if EMPGs are rarer at lower redshifts, EMPGs have been discovered and studied also in the local universe (Izotov & Thuan 1998; Thuan & Izotov 2005; Pustilnik et al. 2005; Izotov et al. 2009, 2018b, 2019; Skillman et al. 2013; Hirschauer et al. 2016; Hsyu et al. 2017). Local EMPGs have low stellar masses ($\log(M_{\star}/M_{\odot}) \sim 6-9$) and high specific star formation rates (sSFR $\sim 10-100 \text{ Gyr}^{-1}$). Thus, they are considered as local analogs of high- z galaxies, because they have low metallicities and low stellar masses, similarly to low-mass galaxies with $\log(M_{\star}/M_{\odot}) \sim 6-9$ at redshift $z \sim 2-3$ (Christensen et al. 2012a,b; Vanzella et al. 2017) and $z \sim 6-7$ (Stark et al. 2017; Mainali et al. 2017).

Recently, a new EMPG survey called "Extremely Metal-Poor Representatives Explored by the Subaru Survey" (EMPRESS, Kojima et al. 2020b) has been initiated with wide-field optical imaging data obtained in Subaru/Hyper Suprime-Cam (HSC; Miyazaki et al. 2018) and Subaru Strategic Program (HSC/SSP; Aihara et al. 2018). In particular, Kojima et al. (2020a) presented element abundance ratios of local EMPGs from EMPRESS and from literature works. They found that neon- and argon-to-oxygen abundance ratios (Ne/O, Ar/O) are similar to those of known local dwarf galaxies and that the nitrogen-to-oxygen abundance ratios (N/O) are lower than 20% of the solar N/O value, in agreement with the low oxygen abundance. Regarding the iron-to-oxygen abundance ratios (Fe/O), they found that their metal-poor galaxies show a decreasing trend in Fe/O ratio as metallicity increases, similarly, as in the star-forming-sample of Izotov et al. (2006), but beginning with two representative EMPGs with exceptionally high Fe/O ratios.

In [Kojima et al. \(2020a\)](#), three scenarios that might explain the observed Fe/O ratios of their EMPGs are described and they can be summarized as follows: i) the preferential dust depletion of iron, ii) a mix of metal enrichment and gas dilution caused by inflow, and iii) the contribution of very massive objects (VMOs) beyond $300 M_{\odot}$.

The first scenario is based on the preferential dust depletion of iron ([Rodríguez & Rubin \(2005\)](#); [Izotov et al. \(2006\)](#)). In this case, it is assumed that the gas-phase Fe/O abundance ratios of the EMPGs decrease with metallicity, due to the fact that Fe is depleted into dust more efficiently than O; this depletion becomes important at higher metallicities, where dust production is more efficient. However, [Kojima et al. \(2020a\)](#) do not find evidence that galaxies with a larger metallicity have a larger color excess, i.e. dustier. Hence, the Fe/O decrease of their sample might not be due to dust depletion, and thus they exclude this scenario.

The second scenario invokes the presence of metal enrichment and gas dilution due to inflow. In this case, it is assumed that these metal-poor galaxies have been formed from metal-enriched gas having solar metallicity and solar Fe/O value. Then, if primordial gas falls onto metal-enriched galaxies, the metallicity (O/H) decreases, whereas the Fe/O ratio does not change. This scenario might explain the almost solar Fe/O ratios, but it would expect an almost solar N/O ratio as well; the two peculiar EMPGs, which show high Fe/O ratios, show low N/O ratios (lower than 20% of the solar value), at variance with what would have been expected by this second scenario. Thus, also this second scenario should be ruled out.

Finally, the third scenario refers to the contribution of super massive stars. In fact, [Ohkubo et al. \(2006\)](#) have shown that stars with masses beyond $300 M_{\odot}$ can produce a large amount of iron during supernova (SN) explosion, and hence [Kojima et al. \(2020a\)](#) suggested that this contribution of iron could result in the high Fe/O ratios of the two EMPGs. This scheme also works well with the N/O ratio, since SN explosion from super massive stars do not change the N/O ([Iwamoto et al. 1999](#); [Ohkubo et al. 2006](#)). In conclusion, [Kojima et al. \(2020a\)](#) favoured this scenario and suggested that the high Fe/O ratios of the two peculiar EMPGs should be attributed to the contribution of super massive stars beyond $300 M_{\odot}$.

In the meantime, I provided yields of massive and very massive stars up to $350 M_{\odot}$ (MTW, Chapter 2), and tested them against observations of Galactic thin and thick disc stars, finding that the latter component could be fairly well reproduced using chemical evolution models that include the ejecta from PISNe. A peculiarity of these models is that they possess an early phase with a low [O/Fe] and then rapidly evolve into the domain of the α -enhanced thick disc stars.

Based on these findings, I wish to test if the high iron-to-oxygen abundance ratios (Fe/O) of the EMPGs can be explained by means of yields that account for the contribution of very massive stars. For this purpose, I make use of detailed chemical evolution models with the inclusion of stellar yields from massive stars described in Chapter 3. Having yields from massive stars up to $350 M_{\odot}$, we have the possibility to consistently change the slope of the IMF in the high mass domain and its upper mass limit.

6.2 Chemical evolution model and stellar ejecta

The chemical evolution code used for the analysis of EMPG data has been already discussed in Sect. 3. As far as the stellar yields are concerned, we will make use here only of the MTW yields, described in Chapter 2. We briefly remind here how these yields have been constructed. For low- and intermediate-mass stars ($< 8 M_{\odot}$), we distinguish between single stars and binary systems that give rise to SNe Ia. For single stars with initial masses $< 6 M_{\odot}$ we have considered yields from Asymptotic Giant Branch (AGB), calculated using the COLIBRI code (Marigo et al. 2013). For $6 M_{\odot} < M < 8 M_{\odot}$, we have taken Super-AGB yields from Ritter et al. (2018). For SNe Ia which are considered to originate from carbon deflagration in CO WDs in binary systems, we have used the yields provided by Iwamoto et al. (1999). The chemical yields of massive stars and VMOs include the stellar wind ejecta, based on the PARSEC models (Bressan et al. 2012), and carefully adapted to explosive yields for electron capture SN (ECSN) (Wanajo et al. 2009), core collapse supernova (CCSN) (Chieffi & Limongi 2004), pulsational pair instability SN (PPISN) (Woosley et al. 2002; Chen et al. 2014; Yoshida et al. 2016; Woosley 2017), and of pair instability SN (PISN) (Heger & Woosley 2002; Heger et al. 2003b). The yields have been calculated for the mass range $M_i = 8 - 350 M_{\odot}$ and for $Z_i = 0.0001, 0.001, 0.006, 0.02$.

The effect of PISNe is evident at $Z_i = 0.0001$ and 0.001 , where there is substantial production of ^{16}O , ^{24}Mg , ^{28}Si , S, Ar, Ca, Ti and Fe due to C and O ignition within a collapsing core. To clarify this point, the original PISN ejecta of selected elements, in M_{\odot} , have been plotted against M_{HE} in Fig. 2.3, for two works in literature. The Heger & Woosley (2002) models (blue lines) have been computed for zero metallicity and pure He stars. The two models computed by Kozyreva et al. (2014b) (red dots) are instead fully evolved models from the main sequence but for $Z_i = 0.001$. We first note that we did not plot ejecta for ^{14}N because they are negligible. In the Heger & Woosley (2002), pure He models with $Z_i = 0$ the ejected mass are below $0.0001 M_{\odot}$. In the Kozyreva et al. (2014b) models instead the ejecta are a fraction of a solar mass, but the N/O mass ratio is at maximum 0.001.

The latter models by Kozyreva et al. (2014b) are particularly interesting because they investigate stars with their full H-rich envelopes. We first note that for ^{16}O , and ^{28}Si , S and Fe the ejecta, at the same M_{HE} values, are very similar. This indicates that PISN ejecta do not depend strongly on the metallicity of the models (at least at those low metallicities) and are mainly unaffected by the surrounding H-rich envelopes. We are thus quite confident that, by using the older Heger & Woosley (2002) models, that are computed for a much finer grid of initial masses but only for zero metallicity pure He stars, the results of this investigation is not significantly affected. It is expected that full models with $Z_i \leq 0.001$ are not significantly different from those used here. We first note from Fig. 2.3 that, stars explode as PISN when their $65 M_{\odot} \leq M_{\text{HE}} \leq 130 M_{\odot}$. Then we also can appreciate the odd behaviour of the oxygen and iron ejecta at increasing M_{HE} . Models with M_{HE} near the lower limit for PISN explosion do not produce iron while near the

TABLE 6.1: Input parameters of the selected models.

Name	Chemical evolution				IMF		Yields
	ν [Gyr ⁻¹]	k	τ_{inf} [Gyr]	A_{SNIa}	$M_{\text{UP}} [M_{\odot}]$	x_{UP}	
M1	0.8	1.0	6.0	0.04	120	1.5	MTW
M2	1.4	1.0	0.5	0.04	200	1.4	MTW
M3	0.3	1.0	3.0	0.05	300	0.6	MTW
M4	0.1	1.0	1.0	0.05	300	0.6	MTW _{mod}
M5	0.3	1.0	3.0	0.05	350	0.6	MTW _{mod}

upper limit, the iron ejecta are even larger than those of oxygen.

The relation between M_{HE} and M_i , the initial mass, is thus a fundamental ingredient to understand the contribution of PISNe to O and Fe enrichment. This relation has been shown in Fig. 2.4 for the full range of massive stars computed with PARSEC and for the metallicities used in this thesis. As already discussed, this relation is affected by uncertainties arising from different assumptions that must be performed in stellar evolution models. Among the most important ones, we recall here those concerned with the efficiency of the $^{12}\text{C}(\alpha, \gamma)^{16}\text{O}$ nuclear reaction rate (Costa et al. 2020a; Farmer et al. 2019) and those concerned with the adopted formulations for the mass loss rates and their dependence on the stellar chemical composition and on the enhancement due to evolution in proximity of the Eddington luminosity (e.g. Vink et al. 2011). As we discuss below, these uncertainties in turn affect the predictions for the contribution by these VMOs.

In the chemical evolution models I assume that EMPGs galaxies are formed by means of a primordial gas infall (as also suggested by Kojima et al. 2020a), and we end the evolution after a fraction of a Gyr (in agreement with the young stellar ages of EMPGs, $\lesssim 50$ Myr, Kojima et al. (2020a,b)). In this scenario, I thus consider an ongoing burst of star formation, superimposed to a quenched chemical evolution, which could have well produced a very low metallicity gas.

As for the IMF, I use a Kroupa-like two-slope power-law IMF (e.g. Kroupa et al. 1993; Kroupa 2001), with $x = 0.5$ for $M < 1M_{\odot}$, and we change both M_{UP} and the slope of the upper IMF (x_{UP}) in the high mass domain, to explore the importance of very massive stars in the chemical evolution of EMPGs.

6.3 Observational data

The observational data considered here are taken from the "Extremely Metal-Poor Representatives Explored by the Subaru Survey" (EMPRESS, Kojima et al. (2020b)) that provides a database of source samples based on the deep, wide field, HSC-SSP data. From this survey, Kojima et al. (2020a,b) provided elemental abundance ratios and other quantities of 9 (extremely) metal-poor galaxies (hereafter named EMPGs, even if O/H may reach half solar), with low-mass ($\sim 10^5 M_{\odot}$ - $10^7 M_{\odot}$), high specific star formation rates (sSFR ~ 300 Gyr⁻¹) and young stellar

ages (~ 50 Myr). Another EMPG J0811+4730 (Izotov et al. 2018a) from the literature, which has the second lowest metallicity (0.0019 Z) reported, is also included in this study. A sample of Galactic stars is also used for comparison (Bensby et al. 2014; Cayrel et al. 2004).

6.4 Results

The first goal is to search which chemical evolution scenario is able to produce the high Fe/O ratios observed in EMPGs 3 and 10. Their peculiar Fe and O abundances, with respect to other EMPGs of the sample and Galactic disc stars, is illustrated in Fig. 6.1. Kojima et al. (2020a) suggested that super massive stars with $M_i \geq 300 M_\odot$ could have the required Fe rich ejecta to explain their peculiarities. In the meantime, I have shown, in the previous section, that PISN could have a non negligible impact on the evolution of MW stars. In particular, I clearly showed that PISN could give rise to an early galactic chemical evolution characterized by high Fe/O ratios (low O/Fe in Fig. 5.5).

Motivated by these considerations, I have investigated different scenarios of chemical enrichment, using these recent yields (MTW) and varying the IMF parameters.

Here, I focus on five chemical evolution models, whose input parameters are summarized in Table 6.1. Two models use the parameters representative of the MW thin and thick disc chemical evolution and serve as comparison models, and other three focus on possible solutions to the EMPG peculiarities. Because of our assumptions on the nature of EMPGs, treated here as starburst galaxies, only the first Gyr of the evolution of the models is shown (Fig. 6.1). However, for the models computed with the parameters typical of the MW thin and thick discs, we show also the full evolution, as underlying dashed lines. We discuss below the five models.

Model M1 has a Kroupa et al. (1993) type IMF with a slope $x_{UP} = 1.5$ in the high mass range and an upper mass limit of $120 M_\odot$. These parameters are the same of model MTW used in Chapter 4 to reproduce the stars of the MW thin disc (dashed line). The evolutionary timescales of the early chemical enrichment are marked by the five filled squares over-plotted at ages of 30 Myr, 60 Myr, 0.1 Gyr, 0.3 Gyr and 0.6 Gyr, from left to right respectively. This model runs almost orthogonal to the sequence of the EMPGs and it cannot explain the high Fe/O ratios of EMPGs 3 and 10. Using other models calculated with the same IMF but with other sets of reasonable chemical evolution parameters, it is still not possible to reproduce the highest observed Fe/O ratios; even by increasing the SNIa fraction to the maximum allowed value, it is not possible to fit the EMPGs 3 and 10. This is because model M1 reaches the O/H values observed for these galaxies in about 100 Myr, a timescale that is too short to allow the evolution of bulk of intermediate and low mass binary systems. I thus confirm that, by using an IMF with a canonical M_{UP} , like the Kroupa et al. (1993), I cannot reproduce the two EMPGs

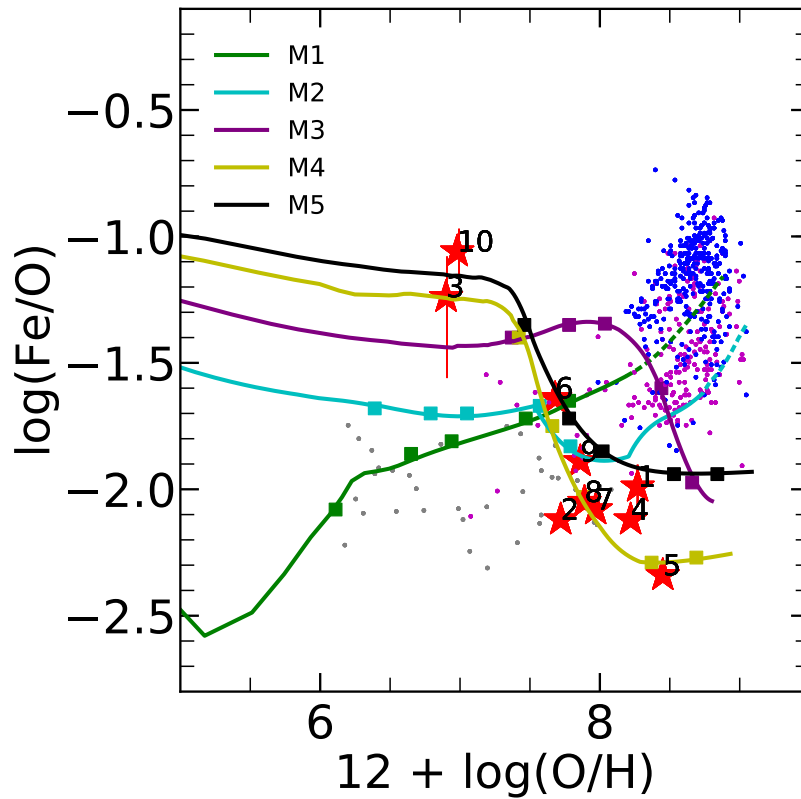


FIGURE 6.1: Evolution of Fe/O as a function of metallicity, (O/H) for the models of Table 6.1. EMPGs from Kojima et al. (2020a) are shown numbered from 1-9, Object 10 an EMPG from Izotov et al. (2018a). Blue and magenta dots represent thin and thick disc stars from Bensby et al. (2014), respectively. Gray dots are low metallicity stars from Cayrel et al. (2004). The dotted lines in M1 and M2 correspond to the fits to thin and thick discs obtained previous chapters. The five squares on the models from left to right are the ages at 30 Myr, 60 Myr, 0.1 Gyr, 0.3 Gyr and 0.6 Gyr respectively.

with the highest Fe/O ratios.

Model M2 corresponds to the fit to the thick disk stars, presented in Chapter 5. This model has an early overall larger Fe/O production, but, as for the M1 model, it is not able to reach the highest observed Fe/O ratios and evolves almost orthogonal to the sequence occupied by the EMGs.

Since PISNe with large initial masses are important producers of Fe, as shown in Fig. 2.3, we consider a model, M3, that enhances the PISN contribution of the MTW ejecta. To this aim, we adopt $x_{\text{UP}} = 0.6$ and $M_{\text{UP}} = 300 M_{\odot}$. Such a flat slope is close to the lowest value determined for the Arches star cluster, as shown by Marks et al. (2012). We note that, although model M3 is able to reach a region of relatively large Fe/O values, not reachable by standard IMF assumptions, it falls too short to explain the large Fe/O observed for EMPG 10. It is however compatible with EMPG 3, considering the large error bar for this object.

Moreover, we note that, as the evolution proceeds, model M3 shows a decreasing Fe/O trend at increasing metallicity, reminding that of the observed EMPGs. Indeed many of the other EMPGs, fall in a region of the diagram that is well populated by other stars and that can be reached by chemical evolution models M1 and M2. Other chemical evolution models could be constructed that fit these galaxies, with perhaps the exceptional case of EMPG 5. In this case however the estimate of the Fe/O ratios could be affected by selective dust depletion (Rodríguez & Rubin 2005; Izotov et al. 2006), that has not been considered here.

This said, model M3 shows that, a continuous burst of star formation actually evolves in a natural way toward such a decreasing sequence, which happens when its metallicity reach the threshold for the PISNe production. Since all the selected galaxies have high specific star formation rates and low total stellar masses and estimated young ages, it could also well be that, some of them, form an aging sequence of the starburst.

This second possibility suggests that, in building the MTW yields we could have overestimated the metallicity were we expect PISNe explosions. As we anticipated above, the modelling of the PISN phase is affected by quite large uncertainties inherited by the uncertain M_i - M_{HE} core relation. This hampers, from stellar modelling alone, a precise prediction of the correct mass-metallicity range for producing the PISN phase, with its peculiar effects in terms of chemical signatures.

In the following, I wish tentatively explore the possible uncertainties in stellar modelling, by exploiting the observed Fe/O abundances of these galaxies as a constraint for the maximum metallicity at which the PISN phase can be observed. Clearly, this possibility rests on the assumption that, at least some of the sample galaxies, are representative of an evolutionary path of homogeneous objects in terms of high specific SFR, stellar masses and young ages. In this way, the reproduction of the high to low Fe/O sequence allows setting a constraint on the metallicity at which the effect of PISN disappears.

To this aim, I build a new yield set (GW20) where, for the VMOs with $M_i \geq 120 M_\odot$, we assume that

- the fading of the PISN phase takes place at a specific unknown metallicity Z_{PISN} , to be determined from the comparison with observations.
- Due to the uncertainties in stellar modelling, we take as reference ejecta for the PISNe at $Z < Z_{PISN}$ those of MTW at $Z = 0.001$. In fact, as shown in Figs. 6.2 and 6.3 for the MTW ejecta, these are better sampled, as a function of M_i , at $Z = 0.001$.
- For $Z_{PISN} \leq Z_i \leq 0.006$, we adopt the VMOs MTW ejecta calculated for $Z_i = 0.006$, while for $Z_i > 0.006$ we adopt the usual MTW yields. Note that for For $Z_{PISN} \leq Z_i \leq 0.006$, we have PISNe that produce α elements but not Fe.

We have therefore run models with top-heavy IMFs, modifying Z_{PISN} to reproduce data. Models M4 and M5, shown in Fig 6.1, are obtained with $Z_{PISN} \sim 0.0005$.

The x_{UP} and M_{UP} values for M4 and M5 are, respectively, $x_{UP} = 0.6$ and $M_{UP} = 300$ and $x_{UP} = 0.6$ and $M_{UP} = 350$. This choice of parameters is selected only because it allows us to reproduce a lower and an upper envelope to the decreasing Fe/O path covered by the data.

Starting with a $\log(\text{Fe}/\text{O}) \sim -1.1$ dex, there is about 1 dex of decrease of the Fe/O ratio with 1 dex of increase in the O/H ratio: in summary, Fe is not more produced by VMOs when $12 + \log(\text{O}/\text{H}) \geq 7.2$, corresponding to about $Z_i = 0.0005$, while O continues to be copiously produced. The reason why models M4 and M5 are able to reproduce the highest Fe/O values of EMPGs is that with $M_{UP} = 300 M_\odot$, we capture the large PISN contribution to Fe, but only at a very low metallicity, $Z \lesssim 5e-4$. In the old MTW ejecta, the PISNe contribution ceases when the metallicity becomes larger than $Z_i \sim 0.001$. With a single model, by appropriately constraining the uncertain PISN phase, it could thus be possible to obtain the entire sequence of the observed EMPGs. As a caveat, we remind that, at the highest metallicity, the estimate of the Fe/O ratios is generally more uncertain because of selective dust depletion (Rodríguez & Rubin 2005; Izotov et al. 2006), that has not been considered here.

Concerning the evolutionary timescales of the chemical enrichment, we observe, from Fig. 6.1, that the highest value of the Fe/O is reached by models M4 and M5 in less than 30 Myr while, the bulk of the low Fe/O values, are reached after about 100 Myr. Exploding PISNe would be only visible in the very early evolutionary stages near or before the observed peak because the self enrichment produced by these stars precludes the explosion of the next stellar generations into PISNe.

In Figs. 6.4 and 6.5, we compare the predicted values of the star formation rates and galaxy stellar masses of the models with the observed ones, respectively. We

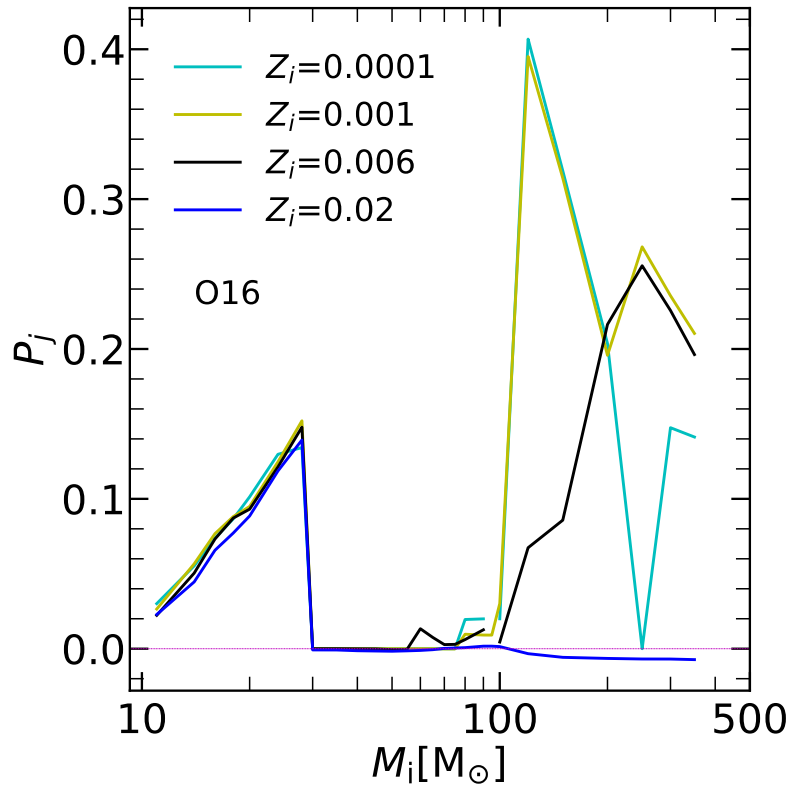


FIGURE 6.2: Normalized O yields, P_O , for massive and very massive stars from MTW yield combination.

$P_j = [E_j(M_i) - (M_i - M_{\text{rem}}) X_{j,0}] / M_i$ where M_i , M_{rem} , $E_j(M_i)$ and, $X_{j,0}$ are, respectively, the initial and the remnant masses, the total ejecta and the initial stellar abundance (in mass fraction) of the element j .

did not try to reproduce the individual objects, as this will require a deeper investigation. Here, we only wish to show that the adopted chemical evolution models are able to reproduce not only the observed chemical enrichment of EMPGs but also the observed relation between metallicity and SFR and that between metallicity and stellar mass. Concerning the latter relation, we note that most of the EMPGs are fairly well reproduced with only three objects being significantly out from the models in SFR.

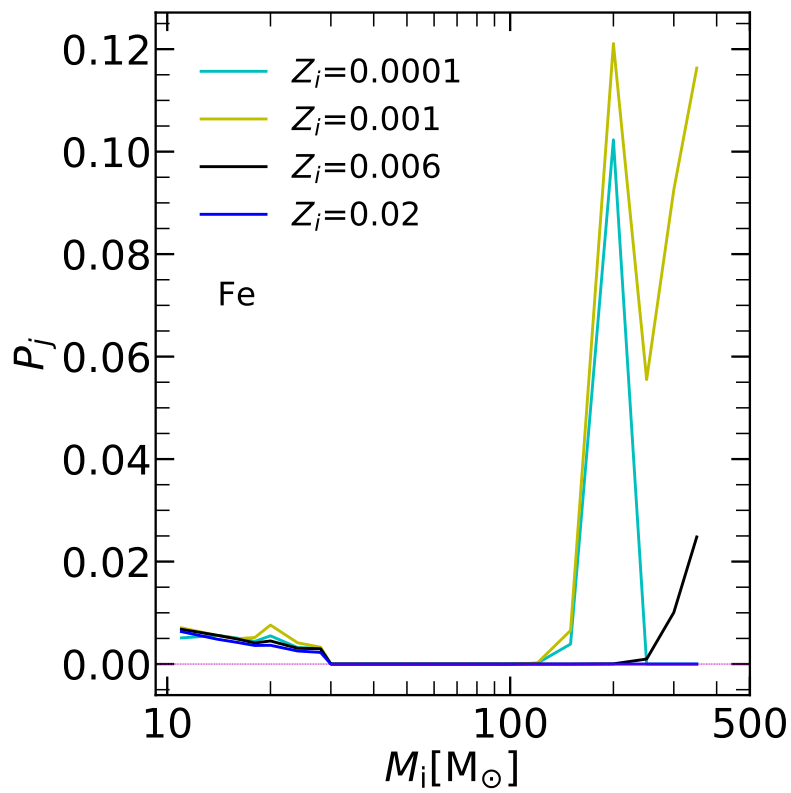


FIGURE 6.3: Same as Figure 6.2, but for Fe .

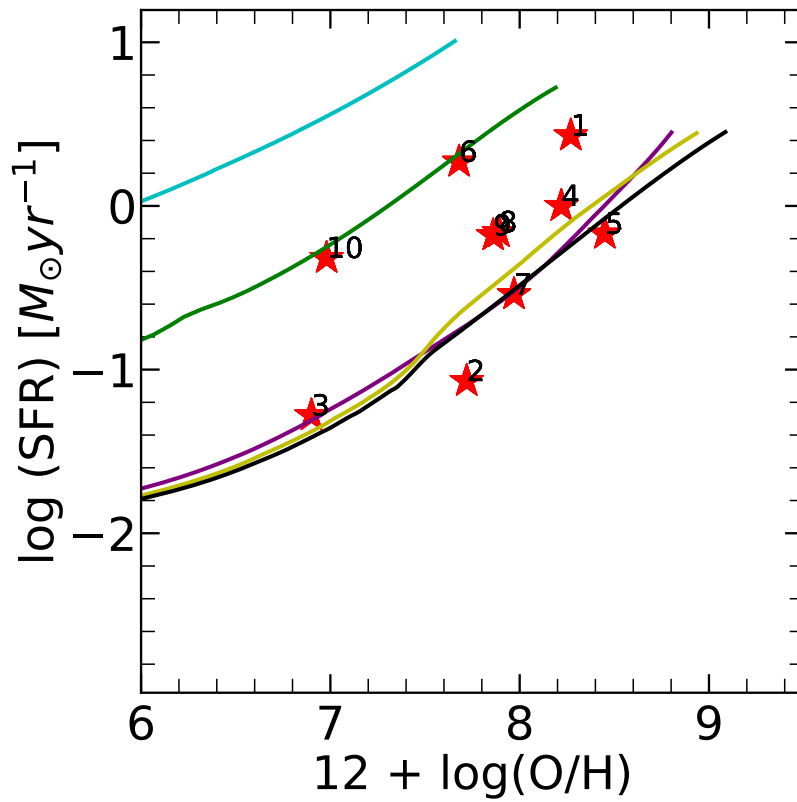


FIGURE 6.4: The evolution of EMPGs star formation rates as a function the metallicity, (O/H). Symbols and models are the same of Fig. 6.1.

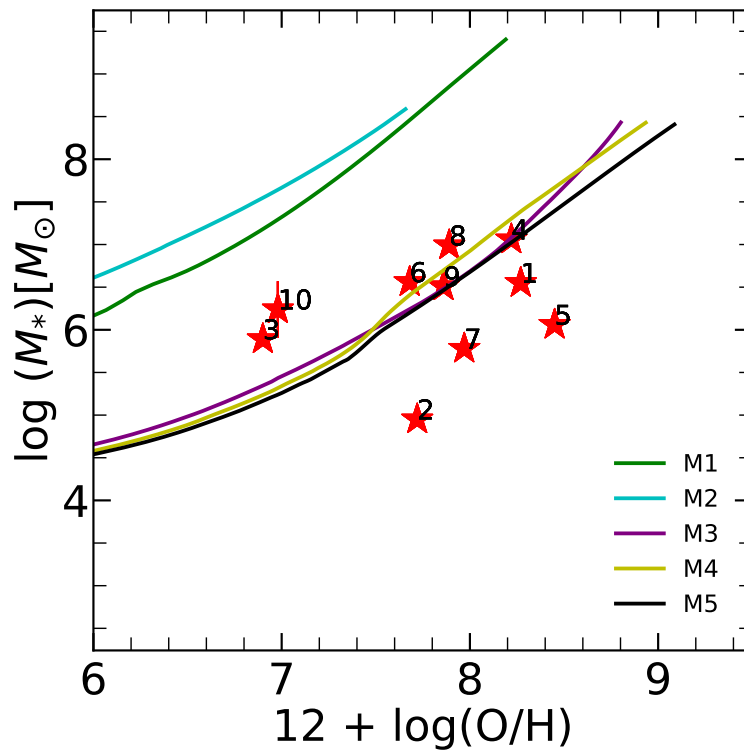


FIGURE 6.5: The evolution of the EMPGs stellar masses as a function the metallicity, (O/H). Symbols and models are the same of Fig. 6.1.

6.5 Conclusions

In this chapter, we analyzed the recent observations from [Kojima et al. \(2020a\)](#), where they provide observational data for metal-poor galaxies and found out two EMPGs having peculiarly high Fe/O ratios at lower metallicities. [Kojima et al. \(2020a\)](#) suggested that these high values can be attributed to the contribution of massive stars with initial mass above $300 M_{\odot}$.

We investigated this peculiarity by means of a chemical evolution code using the recent yields from this thesis (MTW), which include the contribution from massive and very massive stars, till $350 M_{\odot}$. These yields take into account the later stages of evolution of massive stars, such as PISN and PPISN. We run different chemical evolution models with different upper mass limit and slope of the IMF.

I have shown that, to reproduce the high Fe/O ratios observed at $12+\log(\text{O}/\text{H}) \sim 7$ in EMPGs 3 and, in particular, in EMPG 10, we need to include the effects of the later evolutionary stages of VMOs that end as PISNe. This can be obtained only if we assume a top heavy IMF.

This result is interesting because, while such a top heavy IMF could be predicted on the basis of the low observed metallicity [Marks et al. \(2012\)](#), this should be not the case, if the absolute SFR is considered. EMPG 3 and EMPG 10 have a SFR which is lower than 0.1 and $1 M_{\odot}/\text{yr}$, respectively. Thus recent models of the IGIMF do not leave room for such a top heavy IMF [Jeřábková et al. \(2018\)](#). One obvious solution could be that the IGIMF model cannot be applied to such galaxies, that are dominated by a starburst.

Though the other EMPGs could be reproduced by standard chemical evolution models, another striking peculiarity, could be the observed fast decrease of the (Fe/O) at increasing (O/H) abundance, despite these galaxies having similar low masses, high specific star formation rates, and young ages.

Thus if we assume that, at least a few of the observed EMPGs form a homogeneous evolutionary sequence of metal poor starbursts, the observed decreasing sequence can be used to empirically determine the threshold metallicity at which the PISNe Fe contribution fade away, Z_{PISN} . We found that with $Z_{\text{PISN}} \sim 0.0005$, we are able to well reproduce the full excursion of EMPGs of the sample. In the original MTW models, the transition metallicity for PISNe Fe production, occurs at $Z_i \sim 0.001$.

Concerning the nature of the EMPGs, this analysis shows that, with their high specific SFR, they should undergo a fast self enrichment that quickly drives them in a domain where PISNe are not more produced by single stellar evolution. Thus, if PISNe arises only in high specific SFR objects, this fast evolution could really challenge their detection in the local universe ([Takahashi 2018](#)). In this respect, we note that the imprinting left by very massive stars, not only in terms of chemical composition ([Takahashi et al. 2018](#)) but also of chemical evolutionary timescales, could be another important signature to establish the nature of the upper tail of the IMF and its deviations from the universality ([Elmegreen & Shadmehri 2003](#); [Kroupa 2008](#); [Marks et al. 2012](#); [Hosek et al. 2019](#); [Romano et al. 2020](#)).

Finally, we recall that recent gravitational waves detection ([Abbott et al. 2016](#); [Abbott et al. 2020](#)) has drawn the attention on a large variety of phenomena that could affect the estimate of the initial masses and metallicities of PISNe progenitors and their yields, arising both from current uncertainties in single stellar evolution theory (e.g. [Costa et al. 2020b](#)), possible effects of rotation (e.g. [Takahashi et al. 2018](#)), not yet included here, and also binary interaction (e.g. [Han et al. 2020](#); [Spera et al. 2019](#); [Stanway & Eldridge 2018](#); [Hurley et al. 2002](#)).

In summary, a variation of the mass and metallicity domain from where PISNe might arise will immediately impact on the choice of the IMF parameters needed to reproduce EMPGs observations. By converse, the study of these galaxies could have a great impact on our understanding of the uncertainties still affecting stellar evolution models.

Chapter 7

Effect of IMF on the evolution of CNO elements

7.1 Introduction

To complete my work on the effect of the IMF in the chemical evolution of galaxies, I briefly discuss in this chapter the evolution of carbon, nitrogen and oxygen, the so called CNO elements. The CNO elements are one of the most abundant and essential elements. Carbon and oxygen are the two most abundant elements after H and He, and the evolution of these elements are of great importance to understand the chemical evolution of galaxies. Carbon is mostly produced during He burning in the stars of roughly all masses, and oxygen, on the other hand, is generally produced by massive stars. Instead, Nitrogen is thought to be produced mostly by low- and intermediate-mass stars (LIMS) but it has been recently shown that massive stars with rotation could be an important contributor to this element. Mass loss and SN explosion eventually eject them into the ISM. There is an important difference between nitrogen and the other two C/O elements ([Matteucci 1986](#)). Carbon and oxygen are directly produced during central He burning of a star's life (3α process and α capture) and beyond. Instead, nitrogen is mainly produced by conversion of carbon and eventually oxygen during the CNO H-burning cycles. For this reason, N-production requires a previous stellar generation that produced C and O rich material. The N produced in this way is thus named a *secondary* element. However, there are also sites where new N is produced in parallel with C and O. The first one is the hot-bottom burning process that follows the III dredge-UP injection of C into the envelopes of the most massive AGB stars. After a flash of the internal He shell, where mainly the 3α process is at work, the newly generated carbon is brought into the external convective envelope. It is then burned by the CNO cycle at the bottom of the convective envelope during the inter-pulse phase. This process provides newly generated N within the same star and, for this reason, this N is named a *primary* element. Mixing by stellar rotation can also bring newly formed C into the H-rich envelopes of massive stars, where it may be also converted into N, by the CNO cycle. Thus also rotation can be a source of primary N.

Observations from [Tomkin et al. \(1992\)](#) show that, at decreasing metallicity, the (C/O) ratio initially becomes sub-solar and then, at even lower metallicities,

it remains flat. However, the study of [Akerman et al. \(2004\)](#), showed that in the regime of extremely metal-poor stars, below $\log(\text{O}/\text{H}) \sim -5$, the (C/O) ratio has a rising trend, almost reaching again solar values. Similar data at very low metallicity, available from high-redshift observations of damped Lyman- α objects which are believed to be galaxies in the early stages of chemical evolution, confirmed this trend ([Wolfe et al. 2005](#)). The increase of the (C/O) ratio at low metallicities has been explained till now using two different scenarios. In the first scenario, adopted by [Akerman et al. \(2004\)](#), the excess carbon at early stages is due to the ejecta of Pop III massive stars ([Limongi & Chieffi 2003](#)). In a more recent scenario ([Chiappini et al. 2006](#)), the carbon excess is contributed even at non zero metallicity if rotation is taken into account. Indeed, shear by rotation can bring elements that have been generated in deep stellar interiors right to the surface where they are ejected into the ISM by stellar winds or in the final explosion. Thus some of the carbon that has been produced during the central helium burning phase may be ejected instead of being converted into nitrogen (by CNO burning) or even into oxygen (by an α capture). Rotation also decreases slightly the internal temperature and, due to lower core temperature, the conversion of C into O becomes less efficient.

It has been observed that also the (N/O) ratio, after an initial decrease at decreasing metallicity, flattens at the lower metallicities ([Pettini et al. 2008](#); [Esteban et al. 2009](#)). The flat behaviour at the lower metallicities is interpreted as due to the production of primary nitrogen while the increasing slope at higher metallicities can be obtained as a result of the formation of secondary nitrogen. However when a detailed analysis with chemical evolution models is performed, generally one finds a strong dip in the N/O behaviour, which is absent in the observed data.

For this reason, there has been, in recent years, a strong interest in stellar models that may provide primary nitrogen at low metallicities. In this respect, we recall that the AGB models by [Karakas \(2010\)](#) are characterized by a large production of primary N. The peak of this primary N production from massive AGB stars can be appreciated by looking to K10 yields in Figs. 2.7 and 2.9. The N-production in [Karakas \(2010\)](#) is from 3 to 6 times the one predicted by the other models considered in this work ([Ritter et al. 2018](#); [Marigo et al. 2020](#)). The origin of this large N production is likely the large III-Dredge-up efficiency assumed in the K10 AGB models (e.g. through overshooting). This stops the growth of the core and, if it is not accompanied by an efficient mass-loss, it also slows down the evolution along the AGB, allowing a larger N enrichment of the ISM. Recent models, fully calibrated on AGB stars in the Large and Small Magellanic Clouds, show that the observed luminosity functions are consistent with much shorter evolutionary times, as well as with stronger mass-loss rates ([Pastorelli et al. 2020](#)). Hence the lower primary N production in AGB models by M20.

Other possibilities have thus been invoked to explain the absence of the dip. Among others, we recall the analysis by [Vincenzo et al. \(2016\)](#) where it was concluded that adopting a high star formation efficiency (SFE), the (N/O) plateau could be extended with the contribution of primary N from massive stars becoming significant to reproduce the (N/O) ratio.

TABLE 7.1: Chemical evolution parameters of the test model.

ν [Gyr ⁻¹]	k	τ_{inf} [Gyr]	A_{SNIa}
0.5	1.0	4.0	0.063

In the following section, we analyze the chemical evolution of the (C/O) and (N/O) ratios with the help of our new yields that include also very massive stars. In particular, we wish to see how the IMF parameters affect the evolution of the (C/O) and (N/O) ratios.

7.2 Effect of IMF on (C/O) and (N/O) ratios

Here we show the prediction for the CNO abundances in chemical evolution models where we change the upper mass limit and the slope in the high mass IMF. The remaining parameters of the test model are kept fixed because here we aim only at testing the effects of the IMF variation. They are shown in Table 7.1 and they are the same of the parameters adopted to reproduce the Galactic thin disk. Also, the yield table is the MTW one, a part in one specific case where we perform a test with the yields with rotation.

The models are compared with data for metal-rich disk stars ($[\text{O}/\text{H}] > -0.5$) and metal-poor halo stars ($-2.2 < [\text{O}/\text{H}] < -0.5$) from [Akerman et al. \(2004\)](#) and from [Spite et al. \(2005\)](#) for C/O. For the N/O ratio the data is compared to the dataset provided by [Israelian et al. \(2004\)](#); [Roederer et al. \(2014\)](#); [Suárez-Andrés et al. \(2016\)](#); [Spite et al. \(2005\)](#).

7.2.1 Slope $x=1.7$

The results of the models computed with a massive star slope of $x=1.7$ ([Kroupa et al. 1993](#)), are shown in Fig. 7.1. The final (C/O) ratio of the data is reproduced quite well with this slope. The effect of increasing the M_{UP} is to increase the O abundance at early times and so to decrease the (C/O) ratio. In the (N/O) plot, we do not note appreciable differences at very low metallicity. This is because PISNe do not contribute to N enrichment, as already discussed in Sect. 6.2. In fact, the corresponding O increase worsens the comparison. The O overproduction is not apparent at $\log(O/H) < -6$ because O appears in both axes and the models with flatter slope shift down and rightward in the same proportions.

7.2.2 Slope $x=1.5$

In Fig. 7.2 we show the results of the models with $x = 1.5$. The effect of a larger fraction of PISNe begins to show up in the (C/O) ratio, but the problem of the (N/O) under-prediction persists for the reason already explained.

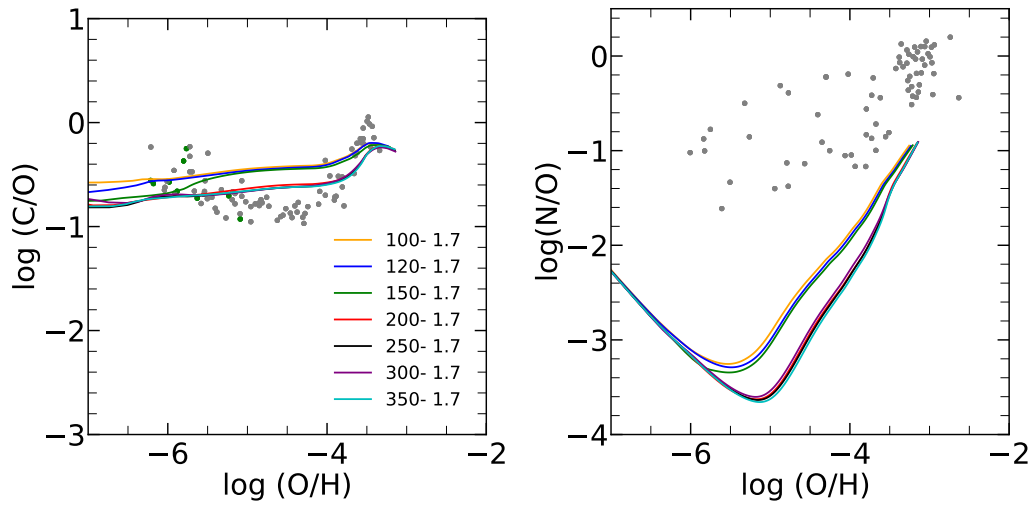


FIGURE 7.1: (C/O) evolution (left panel) and (N/O) evolution (right panel). Data are taken from Akerman et al. (2004); Spite et al. (2005) for (C/O) ratio, the N/O ratio the data is taken from Israelian et al. (2004); Roederer et al. (2014); Suárez-Andrés et al. (2016); Spite et al. (2005) as detailed in the text. The slope of the IMF is $x = 1.7$, and the different models show the effect of varying the upper mass limit of the IMF.

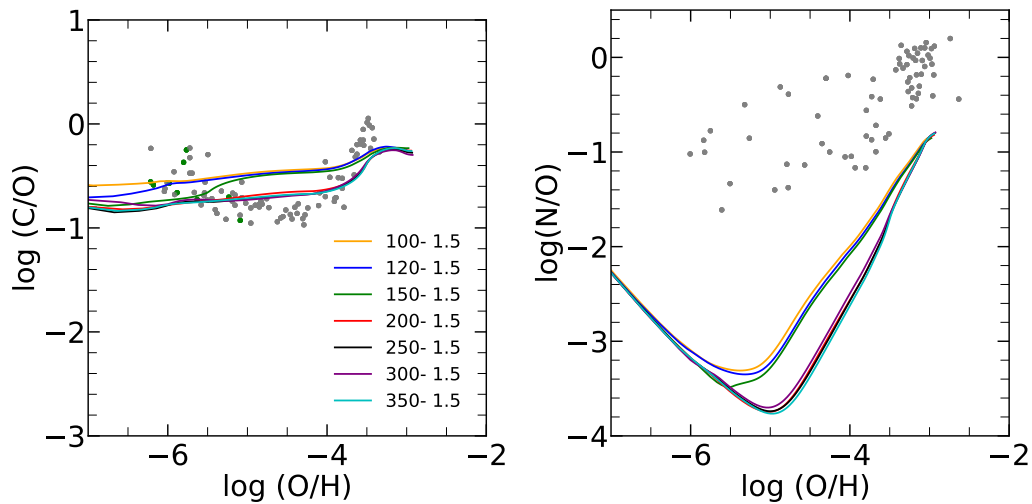


FIGURE 7.2: Same as Fig. 7.1 but with the slope of IMF of $x=1.5$.

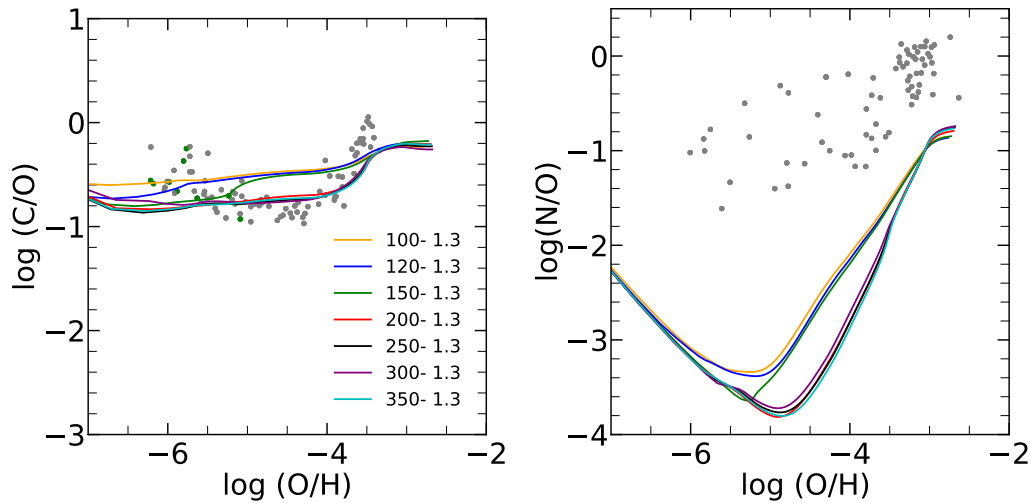


FIGURE 7.3: Same as Fig. 7.1 but with the slope of IMF of $x=1.3$.

7.2.3 Slope $x=1.3$

With a slope of $x=1.3$, similar to a Chabrier IMF, the final (C/O) and (N/O) ratio decreases but with this IMF, and keeping all other parameters unchanged, we over-predict the final (O/H) ratio (Fig. 7.3). This discrepancy could be likely cured by using different chemical evolution parameters. We note that, by increasing the upper mass limit, the (C/O) data at low metallicity are better reproduced but there remains the problem of a higher (C/O) abundance at very low metallicity.

However, with this slope, the models do not start to increase in the (C/O) ratio at lower metallicities and this is due to a more steeper slope than the previous case because of which the number of massive stars drops and so does the contribution of carbon from PPISN/PISN. Therefore, as the slope of the IMF gets more steeper, this effect dies out and only visible where we adopt a top-heavy IMF.

7.2.4 Slope $x=0.8$

Finally an extreme slope $x = 0.8$ (Fig. 7.4) the model can fit the intermediate plateau and the rise toward solar values but, keeping this IMF up to high metallicities, obviously over-predict the actual (O/H) metallicity and, at the same time, it does not solve the problem of the upturn at very low metallicity. The same is true for the (N/O) ratios i.e. both the final values of the metallicity and the dip are too large.

7.2.5 N/O ratio

In the previous sections, we showed that variations of the upper mass limit and the slope alone, cannot explain the observed evolution of the (N/O) ratio with the metallicity. As already discussed in literature, rotation is a crucial feature to

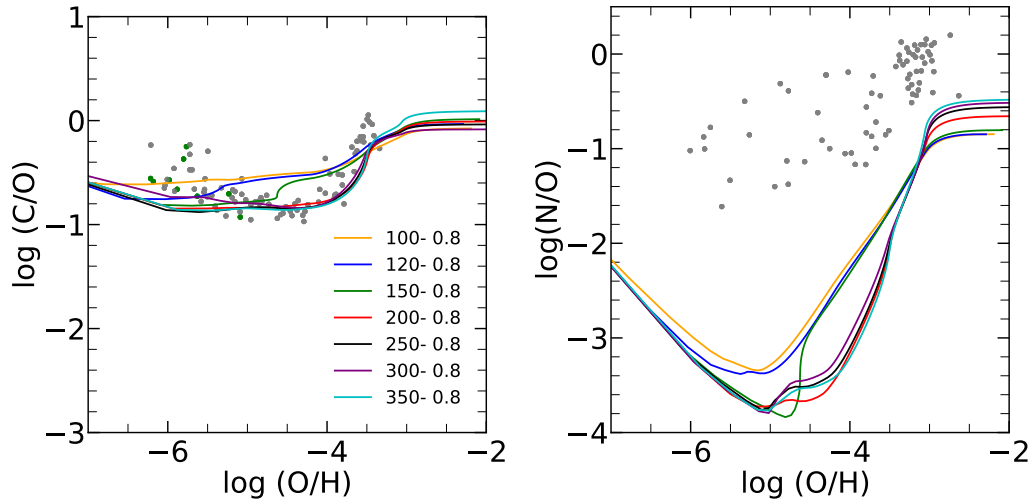


FIGURE 7.4: Same as Fig. 7.1 but with the slope of IMF of $x = 0.8$.

reproduce the abundance of nitrogen at low metallicity (Chiappini et al. 2005; Prantzos et al. 2018; Romano et al. 2019). Here we test the effect of rotations with a model that makes use of the recent yields by Limongi & Chieffi (2018). The model, calculated with the same chemical evolution parameters of the test model used before (Table 7.1) and the IMF we used for the thin disc, model MTW with $x = 1.5$ and $M_{\text{UP}} = 120M_{\odot}$, is shown in Fig. 7.5. We see that this model is able to go through the lower limit of the data. However it is reminded to the reader that the model has not been calibrated or fine tuned to reproduce the (N/O) ratio perfectly. It is just to show the importance of rotation for elements such as N. However, it will be calibrated in the near future.

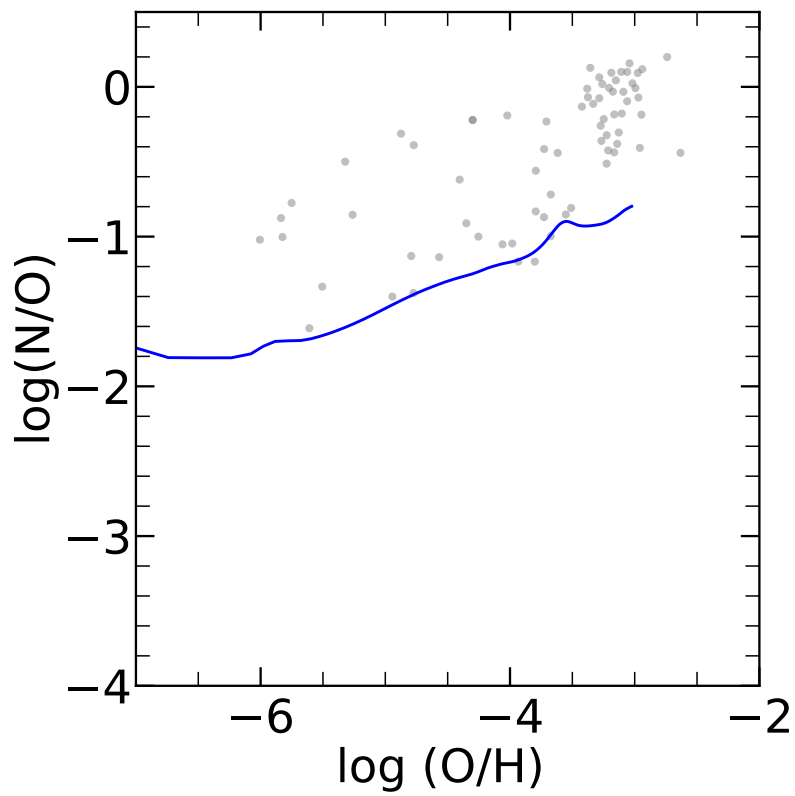


FIGURE 7.5: The N/O ratio predicted by a model with yields from [Limongi & Chieffi \(2018\)](#), which include rotation. The data are the same as in Fig. 7.1.

7.3 Conclusions

In this chapter, I have analyzed the effects of changing the upper mass limit and the slope in the high mass domain of the IMF, on the evolution of the (C/O) and (N/O) ratio. For this purpose, I used the MTW yields computed in this thesis, that extend till $350 M_{\odot}$. We took the (C/O) data from [Akerman et al. \(2004\)](#) and [Spite et al. \(2005\)](#). For the (N/O) ratio the data used was from [Israelian et al. \(2004\)](#); [Roederer et al. \(2014\)](#); [Suárez-Andrés et al. \(2016\)](#); [Spite et al. \(2005\)](#).

While for the (N/O) one has definitely to find another solution, that is likely to consider the effects of rotation at low metallicity, we note that the models with a top-heavy IMF are those that better reproduce the C/O data in the range $-5.5 \leq (O/H) \leq -2$. On the other hand, there are hints that such an IMF, if realistic, cannot be sustained indefinitely. For example, [Marks et al. \(2012\)](#) provide evidence for a significant flattening of the IMF at low metallicities. In contrast, there is evidence that the centres of massive early-type galaxies have a bottom-heavy IMF ([van Dokkum et al. 2017](#)); in order to reach their observed high central metallicities and α -enhancement the IMF should have been different in the past, likely top-heavy ([Chiosi et al. 1998](#); [Chiappini et al. 2000](#)). Thus, I suggest that the observed C/O ratios should be analysed also with models that allow a variation of the IMF during the evolution. If the IMF begins top-heavy and then turns bottom-heavy while reaching a fraction of the solar metallicity, then the model could well reproduce the run of the (C/O) and at intermediate O/H values and, at the same time, it will not overproduce the final metallicity (O/H). More work needs to be done to know if there could be any contribution of VMOs in the evolution of (C/O) ratio at earlier times and if PISN could have played a role in their evolution, and how simultaneously the (N/O) ratio can be reproduced.

It is likely that using yields that include rotation and also the PISN contribution, one may reproduce both the (C/O) and the (N/O) observations at once. Of course one should also take into account the possibility of a variation of the IMF during the evolution, for example due to the metal enrichment itself. I plan to do this work in the next future.

Chapter 8

Summary and Future prospects

8.1 Summary

In the first part of the thesis, I investigated the impact of the ejecta of massive and very massive stars on the predictions of chemical evolution models. I constructed different sets of chemical yields that include both stellar winds and explosion contributions. To this aim, I collected various explosive yields available in the literature and combine them with the wind ejecta computed with our code PARSEC or other authors. A novelty of this thesis is that we investigate the effect of increasing the IMF upper mass limit up to $M_{\text{UP}} = 350 M_{\odot}$, which is well beyond the canonical value of $M_{\text{UP}} \sim 100 M_{\odot}$, typically used in most studies. This allows to explore the impact of VMOs, which are expected to eject significant amounts of newly produced elements through both powerful stellar winds and PPISN/PISN explosions. For completeness, we also include the chemical yields of AGB stars computed with the COLIBRI (Marigo et al. 2013) and from other studies.

The different sets of chemical yields were then incorporated in the chemical evolution code CHE-EVO (Silva et al. 1998), to analyse the chemical evolution of the MW thin- and thick disc stars in the solar vicinity. For the corresponding observational data, we rely on the accurate abundance measurements and kinematical classification by Bensby et al. (2014).

For each set of chemical yields, I ran large grids of chemical evolution models to single out the parameters that best fit the main observational constraints of the above MW components.

Guided by recent models that fully reproduce the different MW components Micali et al. (2013); Grisoni et al. (2017), I ran large grids of chemical evolution models to single out the parameters that best fit the main observational constraints of the above MW components, adopting different yields tables. For the thin disc, these are: the present-day star formation rate, the gas fraction, the rates of CCSN and SNIa, the metallicity of the Sun at its birth epoch ≈ 4.6 Gyr ago, and the observed MDF. For all sets of chemical yields, we were able to find suitable combinations of input parameters that match all the constraints reasonably well (see Table. 3.2). In the best-fit models the Schmidt star formation law, has a typical efficiency in the range $0.4 < \nu < 0.8$ and an exponent $k = 1$. The gas infall time-scale generally varies in the range $3 < \tau/\text{Gyr} < 8$. The higher values are obtained with the MTW, KTW and MLr yields. The lower ones refers to the Rr and Rd yields.

Once the chemical evolution model is calibrated for each set of yields, we focus on the trends of the abundance ratios of α -elements ($[\text{O}/\text{Fe}]$, $[\text{Mg}/\text{Fe}]$, $[\text{Si}/\text{Fe}]$, $[\text{Ca}/\text{Fe}]$), as a function of the metallicity, as traced by $[\text{Fe}/\text{H}]$. The main conclusions are as follows:

- A general agreement is found for $[\text{O}/\text{Fe}]$ and $[\text{Si}/\text{Fe}]$, while the predictions for $[\text{Mg}/\text{Fe}]$ and $[\text{Ca}/\text{Fe}]$ run below the observed data. The best results are obtained when including the yields from rotating massive stars (Limongi & Chieffi 2018) and those based on our PARSEC models for the hydrostatic phases. With the Ritter et al. (2018) yields, all abundance ratios turn out significantly under-predicted, even though the corresponding calibrated chemical evolution model reproduces the thin disc constraints. After carefully examining the problem, we conclude that a possible cause is the large iron production of these sets of yields for some values of the initial mass.
- Most best-fit models are able to recover reasonably well the slope of the bulk of the thin disc stars. With our MTW set of yields, the calibrated IMF exponent is $x = 1.5$, which is intermediate between the results of Kroupa et al. (1993, $x = 1.7$) and the top-heavier IMFs of Kroupa (2001, $x = 1.3$) and Chabrier (2003, $x = 1.3$).
- In the study we did not find evidence that the IMF exponent is degenerate with other chemical evolution parameters, e.g. ν or k , but we cannot exclude that more complex chemical evolution models may provide a different indication. Recently Valentini et al. (2019) pointed out that hydrodynamical models support either of the Kroupa IMF slopes, depending on the set of observational data adopted for comparison. In this respect, we note that a steeper slope of the IMF could be more suitable to reproduce thin disc stars, as suggested by various other investigations (Matteucci & Francois 1989b; Matteucci 2001; Grisoni et al. 2018; Matteucci et al. 2019, 2020).

In the next part of my work, I focused on the thick disc population of the MW. Thick disc stars exhibit an $[\text{O}/\text{Fe}]$ vs. $[\text{Fe}/\text{H}]$ pattern different from that of the thin disc stars, characterised by a steeper slope and a larger degree of α -enhancement, i.e. with higher $[\text{O}/\text{Fe}]$ ratios. This feature is much less evident in the $[\text{Mg}/\text{Fe}]$ diagram.

In this respect, we note that there are stars, likely belonging to the thin disc according to the kinematical classification, that have higher $[\text{O}/\text{Fe}]$ values and fall in the region populated by the thick disc stars. Our thin disc models do not reproduce such stars. However, it is not clear whether this *anomalous* behaviour is real or, rather, the kinematical parameters of these stars varied in such a way that they are now classified as thin disc members. This effect could be due to stellar migration that is not considered here.

None of the chemical evolution models calibrated on the thin disc is able to reproduce the $[\text{O}/\text{Fe}]$ trend of the thick disc. Indeed there are many evidences that the thick disc formed in a much shorter timescale than that of the thin disc and with a larger star formation efficiency. Using parameters similar to those proposed

by Micali et al. (2013) and Grisoni et al. (2017) we were able to reproduce the observed trends of $[O/Fe]$ vs. $[Fe/H]$ and $[Mg/Fe]$ vs. $[Fe/H]$ of the thick disc.

It has also been recently suggested that a higher α -enhancement could be produced by considering yields from fast rotating stars (Limongi & Chieffi 2018; Romano et al. 2019). In this regard, our analysis shows that, using the yields from fast rotating massive stars, the chemical evolution models populate the upper envelope of thick disc stars. Furthermore, I note that, by using yields with initial rotational velocity above 150 km/s, does not produce a significant variation in the chemical evolution models. Conversely, using averaged rotation yields (Prantzos et al. 2018) the calibrated model places in between thin and thick disc stars while, models that use yields for zero rotational velocity, run on the lower envelope delimited by thin disc stars. An interesting properties of these models is that, even by adopting model parameters characteristic of the thin disc, one can reproduce all the other components (halo stars included) by increasing only the fraction of rotating stars. This in fact may give rise to a degeneracy between the some chemical evolution parameters (τ_{inf} and ν) and the stellar rotational velocities.

Motivated by the fact that, in recent years, there has been growing evidence for a top heavy IMF, in particular in metal poor and highly star forming systems (Marks et al. 2012; Jeřábková et al. 2018) I tried to compute thick disc models with a higher M_{UP} . This allows me to check the effects of analysing the effects of a top heavy IMF where, consistently with observations, M_{UP} may be significantly larger than the value usually adopted. With the MTW yields I can check the possible effect of very massive objects, in particular of PISNe. To my knowledge, this has never been done before. Using the same chemical evolution parameters of model TD1, I computed other three models, one with a steeper IMF ($x=1.7$) and other two with $M_{UP}=200$ and $x=1.7$ and 1.4 respectively. The latter two models better reproduce the thick disc observations of in the $[O/Fe]$ vs. $[Fe/H]$ diagram. However they fail to reproduce the low metallicity halo stars, because PISNe produce also large amount of Fe. The situation significantly improves when we consider the $[Mg/Fe]$ vs. $[Fe/H]$ diagram. In this case the Mg produced by PISN drive the models into the region populated by the data of thick disk stars. At the same time the Fe contribution at lower metallicities ($[Fe/H] \leq -2$), allow the models to reproduce the observations of halo star in this region of the diagram. Halo stars in the $[Mg/Fe]$ vs $[Fe/H]$ diagram show a large dispersion that is reproduced by our models, if we allow different kinds of IMF.

The models show that PISNe affect more the low metallicity stars than the more metal rich ones. Thus they should affect the halo component, that has not been directly analysed here, even if some hints have been discussed in relation to the early evolution of the thick disc models. However the different results obtained when considering the data concerning the two different element ratios, $[O/Fe]$ or $[Mg/Fe]$, do not allow us to draw firm conclusions on the effects of PISNe at very low metallicity. Moreover MTW yields show that the effects of PISNe on oxygen and magnesium can be seen up to $Z_1 = 0.006$, i.e. the metallicity of the Large Magellanic Cloud. We confirm that the comparison with the thick disc data show that their effect could be significant.

In the light of these results, we may reasonably expect that similar data, which actually exist for nearby extremely metal-poor galaxies (Kojima et al. 2020a), might show even more the chemical signatures of very massive stars, and that would witness their possible role in the early phases of galaxy evolution.

The analysis of these data constitutes another important application of our modelling of massive stars with different IMFs, that I have investigated in this thesis.

Kojima et al. (2020a) provide observational data for metal-poor galaxies and found two peculiar EMPGs with near solar Fe/O ratios, at lower metallicities. These values are much higher than those of other galactic stars' data at the same metallicity and of other metal-poor galaxies in the same study. Kojima et al. (2020a) suggested that the high Fe/O ratios can be attributed to the contribution of super massive stars above $300 M_{\odot}$. Since massive PISNe are known to be powerful sources of Fe, I investigated on the origin of this high (Fe/O) ratios employing our chemical evolution code with the MTW yields. I run different chemical evolution models with different upper mass range and slope of the IMF and got the following conclusions.

I found that we cannot reproduce the two peculiar EMPGs (object 3 and 10) if we use a standard IMF with the upper mass limit of 100-120 M_{\odot} . By adopting yields that include the contribution of PISNe and a flatter slope in the high mass domain, I find that the Fe/O ratio increases but not yet at the required level. In order to reproduce EMPG 3 but especially EMPG 10 (because of the smaller error bar) a top heavy IMF is needed.

This result is interesting because, while such a top heavy IMF could be predicted on the basis of the low observed metallicity Marks et al. (2012), this should be not the case, if the absolute SFR is considered. EMPG 3 and EMPG 10 have a SFR which is lower than 0.1 and 1 M_{\odot}/yr , respectively. Thus recent models of the IGIMF do not leave room for such a top heavy IMF Jeřábková et al. (2018). One obvious solution could be that the IGIMF model cannot be applied to such galaxies, that are dominated by a starburst.

Though the other EMPGs could be reproduced by standard chemical evolution models, another striking peculiarity, could be the observed fast decrease of the (Fe/O) at increasing (O/H) abundance, despite these galaxies having similar low masses, high specific star formation rates, and young ages. Thus if we assume that, at least a few of the observed EMPGs form a homogeneous evolutionary sequence of metal poor starbursts, the observed decreasing sequence can be used to empirically determine the threshold metallicity at which the PISNe Fe contribution fade away, Z_{PISN} . We found that with $Z_{PISN} \sim 0.0005$, we are able to well reproduce the full excursion of EMPGs of the sample. In the original MTW models, the transition metallicity for PISNe Fe production, occurs at $Z_i \sim 0.001$.

The EMPGs 3 and 10 are characterized by a top-heavy IMF and with their high specific SFR, undergo a fast self enrichment that quickly should drive them in a domain where PISNe are not more produced by single stellar evolution. We note that the low metallicity window, $Z_i \leq Z_{PISN} \sim 0.0005$, coupled with the fast evolution of EMPGs could really challenge the detection of massive PISNe in the local

universe (Takahashi 2018). Indeed the imprinting left by very massive stars, not only in terms of chemical composition (Takahashi et al. 2018) but also of chemical evolutionary timescales, could be another important signature to establish the nature of the upper tail of the IMF and its deviations from the universality.

Given the difference of these new yields at low and very low metallicity with respect to the other ones found in literature, I turned my attention to another important problem, the evolution of the CNO elements in metal-poor systems.

Thus in the next chapter, I focused on the impact of changing the upper mass limit and the slope in the high mass IMF, on the evolution of the (C/O) and N/O ratio. For this purpose, I analysed the (C/O) and (N/O) data by Pettini et al. (2008), Akerman et al. (2004) and Esteban et al. (2009), using the MTW yields of this work.

I have found that our new yields cannot reproduce the observed trend of (N/O) with (O/H). This is expected because i) the contribution of PISN to N is negligible, and ii) the contribution to N of VMO winds increases with increasing metallicity, which is the opposite trend. By adopting other yields, I confirmed that the more likely solution is to consider the effects of rotation at low metallicity.

I could neither reproduce the full (C/O) evolution with the MTW yields. However, in this respect, I note that MTW models with a top-heavy IMF are those that better reproduce the C/O data in the range $-5.5 \leq (O/H) \leq -2$. Thus, given the existing suggestion in literature in favour of a varying IMF, I suggest that the observed (C/O) and (N/O) ratios should be analysed also with models that allow a variation of the IMF during the evolution, and yields that include rotation and also the PISN contribution.

8.2 Future Prospects

In this era, a great deal of spectroscopic data have been already accumulated by current Galactic surveys such as GAIA (Gaia Collaboration et al. 2018), AMBRE (de Laverny et al. 2013), APOGEE (Majewski et al. 2017), GALAH (Buder et al. 2019), LAMOST (Cui et al. 2012), and there is a vast scope to get more high-resolution spectroscopic data in the future, which will provide us with a much more detailed picture of the formation and evolution of the MW.

Here I list some of the prospects related to this thesis:

- Working on the upcoming data-sets will help us to improve the identification of the different populations in the MW. The new data will provide 3D spatial distribution and velocities, interstellar extinction, chemical compositions. At the same time, we will have stellar ages and masses for a large number of stars. All these new data should be analyzed with suitable chemical evolution models to get information on the evolution of individual stars and/or galaxies.
- In this thesis, I have presented the possible effects of PISNe in chemical evolution studies and their possible impact on metal-poor populations. An interesting research line would be to look for more of such peculiar cases of galaxies or stars, as shown in Chapter 6, related to the elements which are produced predominantly by PISNe, which till now might be explained in a different way or are yet unexplained. If the role of the PISNe was that dominant in the early universe, more such data should be found in the metallicity domain and for the elements for which PISNe contribute.
- I confirmed that, at low metallicity, rotation must be included to reproduce nitrogen and, at the same time, I showed that new AGB yields do not reproduce the high nitrogen ejecta of previous models. Yields that are able to account for both PISNe and rotation are thus highly favourite.
- Having clarified the role played by the IMF in chemical evolution models, and especially what kind of IMF could be preferred at different metallicities, my current analysis suggests that we need to perform a thorough study using the previously suggested yields, including rotation and VMOs, within a scheme of variable IMF, that could be, for example, metallicity dependent.

I plan to pursue these aims in my further career.

Appendix A

Tables of chemical ejecta

Here we present the ejecta tables (set TW) for massive and very massive stars used in this thesis that will be available on-line, for 4 values of the initial metallicity ($Z_i = 0.0001, 0.001, 0.006, 0.02$) and 30 values of the initial mass ($8 \leq M_i/M_\odot \leq 350$). Each table corresponds to one selected value of Z_i . The row labelled $X_{j,0}$ gives the initial abundances (in mass fraction) corresponding to a scaled-solar composition for elements heavier than He (Caffau et al. 2011). The initial abundances of H and He as a function of Z_i are derived from the enrichment law calibrated with PARSEC models (Bressan et al. 2012). The complete ejecta tables include the following chemical species: ^1H , ^3He , ^4He , ^7Li , ^7Be , ^{12}C , ^{13}C , ^{14}N , ^{15}N , ^{16}O , ^{17}O , ^{18}O , ^{19}F , ^{20}Ne , ^{21}Ne , ^{22}Ne , ^{23}Na , ^{24}Mg , ^{25}Mg , ^{26}Mg , ^{26}Al , ^{27}Al , ^{28}Si , ^{29}Si , P, S, Cl, Ar, K, Ca, Sc, Ti, V, Cr, Mn, Fe, Co, Ni, Cu, Zn. For elements without the indication of the atomic mass, we give the sum of the ejecta of their stable isotopes.

The ejecta tables are arranged in two groups:

1. tables of wind ejecta, E_j^w
2. tables of total ejecta, $E_j^w + E_j^{\text{sn}}$.

We remind that mass loss in the PARSEC code is applied only to stars with $M_i \geq 14 M_\odot$. It follows that the wind ejecta for stars with $M_i < 14 M_\odot$ are set to zero. It is worth specifying that the ejecta of the VMO that avoid the explosion and directly collapse to black holes (DBH, for $M_{\text{HE}} > 130 M_\odot$) are included in the wind tables. The explosion ejecta tables contain the chemical contribution of all layers that extend from M_{cut} to M_{fin} . This applies to both successful CCSN, PPISN and PISN. We recall that in the case of a failed core-collapse supernova we have $M_{\text{cut}} = M_{\text{rem}} = M_{\text{fin}}$ and the explosion ejecta are zero for all species. As to PISN, we set $M_{\text{cut}} = 0$, as the associated thermonuclear explosion leaves no remnant.

Other relevant stellar parameters are tabulated (in units of M_\odot), namely: the pre-SN mass (M_{fin}), the mass of He core (M_{HE}), the mass of the C-O core (M_{CO}) and remnant mass (M_{rem}). We also provide the pre-SN phase (see also Sect. 2.2):

- RSG: red supergiant
- BSG: blue supergiant
- WC: Wolf-Rayet stars enriched in carbon

- WN: Wolf-Rayet stars enriched in nitrogen
- WO: Wolf-Rayet stars enriched in oxygen
- LBV: luminous blue variables

and the final fate:

- ECSN: electron capture SN
- sCCSN: successful core collapse SN
- fCCSN: failed core collapse SN
- PPISN: pulsation-pair instability SN
- PISN: pair instability SN
- DBH: stars that direct collapse into black hole without explosion

As an example, a reduced version of an ejecta table, containing a smaller number of elements, is presented in Table A.1.

TABLE A.1: An example of a table containing the total ejecta, $E_j = E_j^w + E_j^{\text{sn}}$ (in M_\odot , see Sect. 2.2.2), of massive and very massive stars used in this thesis (extracted from the set MTW), for $Z_i = 0.02$ and a few selected chemical species. The complete tables, available online, include more nuclides, from H to Zn.

M_i	X_{i0}	M_{fin}	M_{He}	M_{CO}	M_{rem}	pre-SN	SN-type	H	^4He	^{12}C	^{14}N	^{16}O	^{19}F	^{20}Ne	^{23}Na	^{25}Mg	...
8.00	8.00	—	1.38	1.38	—	RSG	—	6.95E+01	2.83E+01	3.59E+03	9.70E+00	8.80E+03	6.61E+07	1.88E+03	4.71E+05	6.99E+04	...
9.00	9.00	1.38	1.38	1.366	—	RSG	ECSN	4.213E+00	2.280E+00	1.409E+02	2.544E+02	4.879E+02	3.540E+06	1.126E+04	1.626E+03	4.307E+03	...
11.00	11.00	1.38	1.38	1.366	1.366	RSG	ECSN	4.984E+00	2.445E+00	1.657E+02	2.765E+02	5.750E+02	4.179E+06	1.378E+02	6.694E+04	4.957E+03	...
14.00	13.03	3.79	2.11	1.51	1.51	RSG	sCCSN	4.85E+00	3.78E+00	1.25E+01	3.94E+02	3.34E+01	2.88E+06	4.72E+02	1.15E+03	3.47E+02	...
16.00	13.94	4.56	2.90	1.67	1.66	RSG	sCCSN	6.04E+00	4.66E+00	2.31E+01	4.57E+02	7.32E+01	4.58E+06	1.69E+01	4.45E+03	6.03E+02	...
18.00	14.96	6.31	4.38	1.69	1.69	RSG	sCCSN	7.23E+00	5.91E+00	2.87E+01	4.95E+02	1.17E+00	6.39E+06	4.28E+01	1.04E+02	1.12E+01	...
20.00	17.74	7.12	5.02	1.76	1.76	RSG	sCCSN	7.96E+00	6.44E+00	3.68E+01	5.40E+02	1.53E+00	8.55E+06	5.61E+01	1.47E+02	1.32E+01	...
24.00	19.41	9.15	6.69	1.82	1.82	RSG	sCCSN	9.07E+00	7.54E+00	6.20E+01	6.33E+02	3.04E+00	1.80E+05	9.62E+01	3.08E+02	1.30E+01	...
28.00	20.76	11.01	8.32	1.85	1.85	RSG	sCCSN	1.03E+01	8.66E+00	7.00E+01	7.52E+02	4.12E+00	2.36E+05	1.29E+00	4.09E+02	2.16E+01	...
30.00	16.71	12.22	8.44	16.71	16.71	RSG	fCCSN	8.35E+00	4.65E+00	3.34E+02	5.03E+02	9.27E+02	6.71E+06	2.47E+02	1.16E+03	9.17E+03	...
35.00	13.31	13.31	9.77	13.31	13.31	WC	fCCSN	1.14E+01	9.62E+00	1.33E+01	1.23E+01	1.61E+01	8.19E+06	4.01E+02	2.84E+03	1.49E+02	...
40.00	12.75	12.39	9.28	12.75	12.75	WC	fCCSN	1.28E+01	1.31E+01	6.74E+01	1.62E+01	1.86E+01	9.12E+06	5.02E+02	4.19E+03	1.88E+02	...
45.00	13.89	13.50	10.10	13.89	13.89	WC	fCCSN	1.38E+01	1.56E+01	9.21E+01	1.96E+01	2.05E+01	9.24E+06	5.72E+02	5.24E+03	2.15E+02	...
50.00	15.03	14.61	10.93	15.03	15.03	WC	fCCSN	1.48E+01	1.81E+01	1.16E+02	2.31E+01	2.23E+01	9.37E+06	6.42E+02	6.30E+03	2.41E+02	...
55.00	16.55	16.08	12.03	16.55	16.55	WC	fCCSN	1.58E+01	2.02E+01	1.42E+02	2.60E+01	2.59E+01	9.71E+06	7.06E+02	7.19E+03	2.66E+02	...
60.00	18.10	17.60	13.13	18.10	18.10	WC	fCCSN	1.68E+01	2.23E+01	1.69E+02	2.89E+01	3.00E+01	1.00E+05	7.68E+02	8.09E+03	2.89E+02	...
65.00	19.93	19.37	14.40	19.93	19.93	WC	fCCSN	1.78E+01	2.40E+01	1.98E+02	3.17E+01	3.54E+01	1.02E+05	8.26E+02	8.92E+03	3.11E+02	...
70.00	22.29	21.67	16.09	22.29	22.29	WC	fCCSN	1.89E+01	2.52E+01	2.27E+02	3.43E+01	4.35E+01	1.03E+05	8.74E+02	9.58E+03	3.30E+02	...
75.00	23.43	22.77	16.91	23.43	23.43	WC	fCCSN	1.99E+01	2.76E+01	2.57E+02	3.70E+01	4.90E+01	1.10E+05	9.44E+02	1.05E+02	3.56E+02	...
80.00	24.56	23.87	17.73	24.56	24.56	WC	fCCSN	2.10E+01	2.99E+01	2.87E+02	3.97E+01	5.45E+01	1.16E+05	1.01E+01	1.15E+02	3.83E+02	...
90.00	26.90	26.15	19.39	26.90	26.90	WC	fCCSN	2.30E+01	3.46E+01	3.53E+02	4.65E+01	7.07E+01	1.14E+05	1.15E+01	1.38E+02	4.36E+02	...
95.00	27.58	26.81	19.90	27.58	27.58	WC	fCCSN	2.40E+01	3.75E+01	5.01E+02	5.01E+01	7.54E+01	1.17E+05	1.23E+01	1.50E+02	4.66E+02	...
100.00	27.75	26.97	19.93	27.75	27.75	WC	fCCSN	2.51E+01	4.11E+01	3.84E+02	5.48E+01	7.76E+01	1.18E+05	1.31E+01	1.63E+02	5.00E+02	...
120.00	22.32	21.69	16.11	22.32	22.32	WC	fCCSN	3.01E+01	6.27E+01	2.54E+02	9.20E+01	4.61E+01	1.07E+05	1.77E+01	2.38E+02	6.76E+02	...
150.00	16.57	16.10	12.03	16.57	16.57	WC	fCCSN	4.09E+01	8.81E+01	1.52E+02	1.41E+02	3.10E+01	9.78E+06	2.42E+01	3.37E+02	9.24E+02	...
200.00	16.11	15.66	11.70	16.11	16.11	WC	fCCSN	5.74E+01	1.21E+02	1.44E+02	2.04E+02	3.21E+01	9.18E+06	3.33E+01	4.77E+02	1.27E+01	...
250.00	16.26	15.80	11.83	16.26	16.26	WC	fCCSN	7.40E+01	1.53E+02	1.47E+02	2.67E+02	3.41E+01	8.43E+06	4.23E+01	6.16E+02	1.61E+01	...
300.00	17.13	16.96	12.46	17.13	17.13	WC	fCCSN	9.20E+01	1.83E+02	1.57E+02	3.22E+02	4.21E+01	1.15E+05	5.12E+01	7.41E+02	1.95E+01	...
350.00	16.84	16.37	12.23	16.84	16.84	WC	fCCSN	1.07E+02	2.17E+02	1.59E+02	3.91E+02	3.83E+01	7.28E+06	6.02E+01	8.94E+02	2.30E+01	...

Appendix B

Chemical and high- z galaxy evolution

In this chapter, I provide brief summaries of two studies that I coauthored during my PhD tenure. The first deals with the analysis of merger rates of binary compact objects in galaxies using different methods, including chemical enrichment histories for individual galaxies and from stellar evolution. In the second work, an analytical solution for the evolution of the gas/stellar mass and metal content in star-forming galaxies has been presented.

B.1 Merging Rates of Binary Compact Objects in Galaxies: Perspectives for Gravitational Wave Detections

The recent detections of several gravitational waves (GW) events by the LIGO/Virgo collaborations ([Abbott et al. 2016a](#); [Abbott et al. 2016](#); [Abbott et al. 2016b](#); [Abbott et al. 2017a,b,c](#); [Abbott et al. 2017](#); [Abbott et al. 2019](#)); also <https://www.ligo.org/>), and the many more expected with the advent of the upcoming advanced configurations and detectors like the Einstein Telescope (ET; see [Sathyaprakash et al. 2012](#); [Regimbau et al. 2012](#); also <http://www.et-gw.eu/>), are to provide tremendous breakthroughs in astrophysics, cosmology and fundamental physics ([Taylor & Gair 2012](#); [Barack et al. 2019](#)). The GW events in the LIGO/Virgo operating frequency band are consistently interpreted as mergers of binary compact star remnants, e.g., neutron stars (NS) and/or black holes (BHs). On the one hand, the analysis of the individual GW signal waveforms can provide useful information about the properties and evolution of the progenitor binary systems (remnant masses, spins, orbital parameters: [Weinstein 2012](#); [Abbott et al. 2016a](#); [Abbott et al. 2016](#); [Abbott et al. 2016b](#)). On the other hand, the statistics of GW events can yield astrophysical constraints on stellar binary evolution (SN kicks, common envelope effects, mass transfers; ([Belczynski et al. 2016](#); [Dvorkin et al. 2018](#); [Mapelli & Giacobbo 2018](#)), on the average properties of the host galaxies (chemical evolution, star formation histories, initial mass function; ([O’Shaughnessy et al. 2010](#); [de Mink & Belczynski 2015](#); [Vitale et al. 2019](#)), and even on cosmology at large ([Taylor & Gair 2012](#); [Nissanke et al. 2013](#); [Liao et al. 2017](#); [Fishbach et al. 2019](#)).

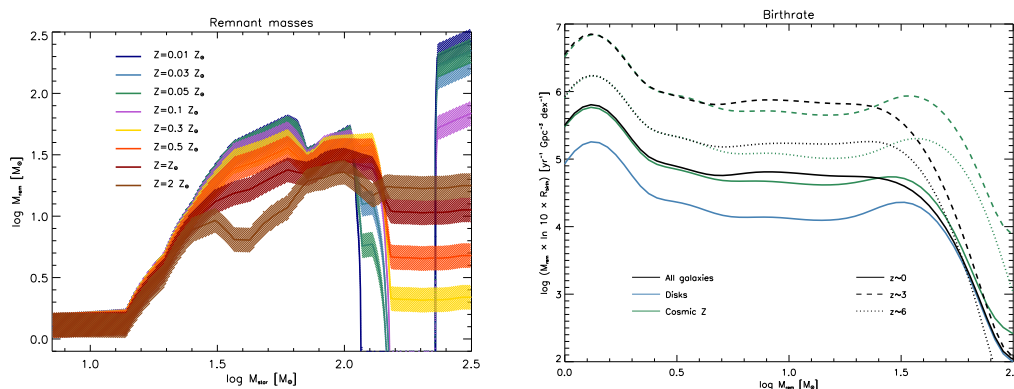


FIGURE B.1: Left panel: Compact remnant mass as a function of the zero-age main sequence star mass at different metallicities $Z = 0.01 Z_{\odot}$ (blue lines), $0.03 Z_{\odot}$ (cyan lines), $0.05 Z_{\odot}$ (green lines), $0.1 Z_{\odot}$ (magenta lines), $0.3 Z_{\odot}$ (yellow lines), $0.5 Z_{\odot}$ (orange lines), Z_{\odot} (brown lines), $2 Z_{\odot}$ (saddle brown lines). Solid lines illustrates the relation $m_{\bullet}(m_{*};Z)$ by Spera & Mapelli (2017) for single stellar evolution, based on the delayed SN engine and including (P)PSNe. We have adopted a compact mass remnant distribution $dp = d \log m_{\bullet}$ with a log-normal shape centered around this relation and with a $1-\sigma$ dispersion of 0.1 dex (illustrated by the shaded areas). Right panel: Compact remnants birthrate $R_{birth}(\log m_{\bullet}; z)$ at different redshift $z \sim 0$ (solid lines), 3 (dashed line), and 6 (dotted line). Green lines refer to the approach based on the cosmic SFR density and cosmic metallicity, while black lines refer to our computation taking into account redshift-dependent galaxy statistics and the star formation and chemical enrichment histories of individual galaxies (blue lines refer to disk-dominated galaxies at $z \lesssim 2$).

In the last decade, a wealth of observations (e.g., UV+far-IR/sub-mm/radio luminosity functions and stellar/gas/dust mass functions, broadband spectral energy distribution, mass-metallicity relationships, size/kinematic evolution, etc.) have allowed estimating the statistics of different galaxy populations as a function of their main physical properties across cosmic time; in addition, these observations have allowed shedding light on the age-dependent star formation and chemical enrichment histories of individual galaxies.

In this work, we have investigated the merging rates of compact binaries in galaxies, and the related rates of GW detection events with AdvLIGO/Virgo and with the Einstein Telescope. We have based our analysis on three main ingredients : (i) redshift-dependent galaxy statistics provided by the latest determination

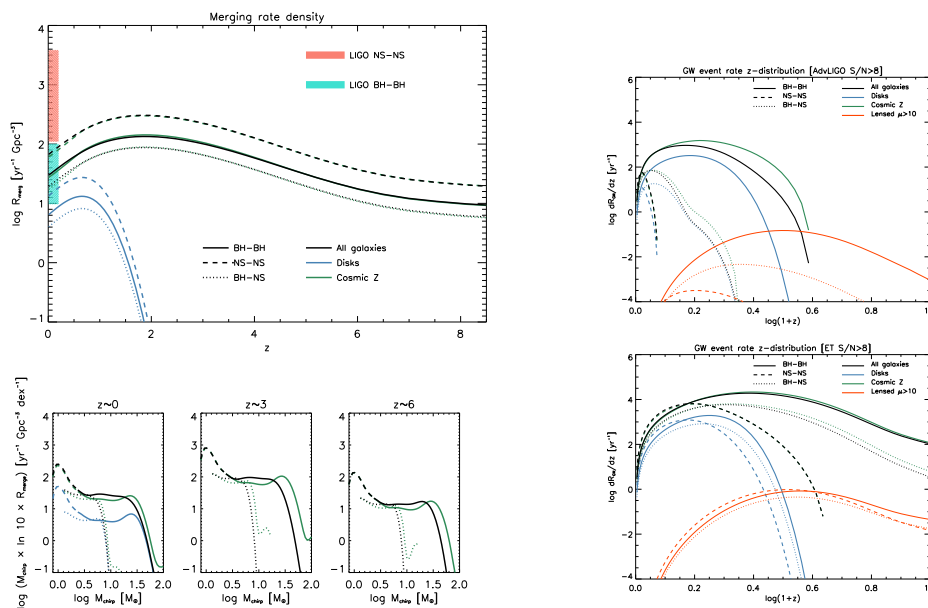


FIGURE B.2: Left panel: Top panel: merging rate density of compact binaries $R_{\text{merg}}(z)$ as a function of redshift. Solid lines refer to BH-BH, dashed lines to NS-NS and dotted lines to BH-NS events. Color-code as in Fig. 4. The cyan and orange shaded areas illustrate the local BH-BH and NS-NS merging rates estimated by LIGO in the O2 run, respectively. Bottom panels: merging rate $R_{\text{merg}}(M_{\bullet\bullet}; z)$ as a function of the chirp mass at redshift $z \sim 0$ (left), 3 (middle), and 6 (right). Right panel: GW event rate per unit redshift expected for the AdvLIGO/Virgo (top panel) and ET (bottom panel) with SNR threshold $\rho \gtrsim 8$. Linestyles and color-code as in Fig. 4. The orange lines refer to galaxy-scale gravitational lensing of GWs with magnification $\mu \gtrsim 10$.

of the SFR functions from UV+far-IR/(sub)mm/radio data ; (ii) star formation and chemical enrichment histories for individual galaxies, modelled on the basis of observations ; (iii) compact remnant mass distribution and prescriptions for merging of compact binaries from stellar evolution simulations. We have presented results for the intrinsic birthrate of compact remnants shown in the left panel of Fig. B.1, the merging rates of compact binaries in the right panel of Fig. B.1, and the related GW detection rates and counts are shown in Fig. B.2, attempting to differentiate the outcomes for BH-BH, NS-NS, and BH-NS mergers. We have compared our approach with the one based on cosmic SFR density and cosmic metallicity, exploited by many literature studies; the merging rates from the two approaches are in agreement within the overall astrophysical uncertainties. We have then investigated the impact of galaxy-scale strong gravitational lensing in enhancing the GW event rate of detectable events toward high-redshift.

In a nutshell, our work has been mainly focused on developing an approach to

post-process the outcomes of stellar evolution simulations toward computing GW event rates of compact binary mergers (both intrinsic and strongly gravitationally lensed). Specifically, we have coupled the metallicity-dependent compact remnant mass spectrum from stellar evolution simulations to the most recent observational determinations of the galaxy SFR functions and the star formation and chemical enrichment histories of individual galaxies; such an approach in principle adds extra layers of information with respect to methods based on the integrated cosmic SFR density and cosmic metallicity like potentially the association of the GW event to the properties of the host galaxy; admittedly, this is the first step and with current data, some degree of uncertainty also comes with it. Nevertheless, accurate treatment of the galaxy-related post-processing along the lines designed here, that hopefully will become feasible in the near future with more precise determinations of the SFR functions and of the enrichment history of galaxies at increasingly higher redshifts $z \gtrsim 3$, will help in fully exploiting future GW observations and stellar evolution simulations to constrain the fundamental processes of stellar astrophysics that ultimately rule the formation and coalescence of binary compact remnants. As a concluding remark, we point out that our approach can also be adapted with minimal change of formalism to multimessenger studies of various galaxy populations at different redshift. Most noticeably, it could be exploited to predict the rate of electromagnetic, neutrino, and cosmic ray emission events associated with NS-NS and/or BH-NS mergers as a function of host galaxy properties and of cosmic time, irrespective of detectability in the GW counterparts.

B.2 New Analytic Solutions for Galaxy Evolution: Gas, Stars, Metals, and Dust in Local ETGs and Their High- z Star-forming Progenitors

Understanding the formation and evolution of galaxies in a cosmological context is one of the main challenges of modern astrophysics (e.g. [Mo et al. 2010](#); [Silk & Mamon 2012](#); [Maiolino & Mannucci 2019](#)). The issue is intrinsically very complex, since it involves many physical processes occurring on vastly different spatial, time, and energy scales.

The ultimate approach to address the problem in fine detail would require the exploitation of intensive hydrodynamical simulations (e.g. [Bekki 2013, 2015](#); [Dubois et al. 2014, 2016](#); [Genel et al. 2014](#); [Hopkins et al. 2014, 2018](#); [Vogelsberger et al. 2014](#); [Schaye et al. 2015](#); [McAlpine et al. 2016, 2019](#)) but a detailed exploration of the related parameter space or different modeling prescriptions is often limited by exceedingly long computational times.

An alternative route to investigate the issue relies on semianalytic models (e.g. [Kauffmann et al. 1993](#); [Lacey & Cole 1993](#); [Cole et al. 2000](#); [De Lucia et al. 2014, 2017](#); [Croton et al. 2006](#); [Somerville et al. 2008](#); [Arrighi et al. 2010](#); [Benson 2012](#); [Lacey et al. 2016](#); [Porter et al. 2014](#); [Cousin et al. 2016](#); [Hirschmann et al. 2016](#); [Fontanot et al. 2017](#)) Such models are less computationally expensive than

hydrodynamic simulations and allow one to more clearly disentangle the relative role of the various physical processes at work; however, the considerable number of fudge parameters can lead to degenerate solutions and somewhat limit the predictive power, especially toward high redshift.

Finally, some specific issues related to the global evolution of the baryonic content in galaxies can be tackled with analytic models, i.e., models with analytic solutions (e.g. Schmidt 1963; Talbot & Arnett 1971; Matteucci & Greggio 1986a; Dwek 1998; Hirashita 2000; Chiappini et al. 2001; Draine 2011; Inoue 2003; Naab & Ostriker 2006; Erb 2008; Zhukovska et al. 2008; Valiante et al. 2009; Dwek & Cherchneff 2011; Asano et al. 2013; Lilly et al. 2013; de Bressan et al. 2014). These are necessarily based on approximate and spatially/time-averaged descriptions of the most relevant astrophysical processes; however, the transparent, handy, and predictive character of analytic solutions often pays off.

In this work, a set of new analytic solutions aimed at describing the spatially averaged evolution of the gas/stellar/ dust mass and metal content in a star-forming galaxy hosted within a dark halo of a given mass and formation redshift has been presented. The basic framework pictures the galaxy as an open, one-zone system comprising three interlinked mass components: a reservoir of warm gas subject to cooling and condensation toward the central regions, cold gas fed by infall and depleted by star formation and stellar feedback (Type II SNe and stellar winds), and stellar mass partially restituted to the cold phase by stars during their evolution. The corresponding metal enrichment history of the cold gas and stellar mass is self-consistently computed using as input the solutions for the evolution of the mass components; the metal equations include effects of feedback, astration, instantaneous production during star formation, and delayed production by Type Ia SNe, possibly following a specified Delay time distribution (DTD). Finally, the dust mass evolution takes into account the formation of grain cores associated with star formation and grain mantles due to accretion onto preexisting cores; astration of dust by star formation and stellar feedback and spallation by SN shock waves are also included. We have then applied our analytic solutions to describe the formation of ETGs and the evolution of their star-forming progenitors. To this purpose, we have supplemented our solutions with a couple of additional ingredients: (i) specific prescriptions for parameter setting, inspired by in situ galaxy-BH co-evolution scenarios for ETG formation, and (ii) estimates of the average halo and stellar mass growth by mergers, computed on the basis of the merger rates from state-of-the-art numerical simulations. We then derive a bunch of fundamental relationships involving spatially averaged quantities as a function of the observed stellar mass: star formation efficiency, SFR, gas mass, dust mass, gas metallicity and stellar metallicity and $[\alpha/\text{Fe}]$ ratio. Here we discuss in brief the evolutionary characteristics of a few of them.

The star formation efficiency f_* which is shown in the left panel of Fig. B.3 is found to be a nonmonotonic function of the stellar mass M_* , with a maximum value of 20%–30% slowly increasing with redshift around $M_* \approx 10^{11} M_\odot$ and a decrease to values less than 10% for $M_* \sim$ a few $10^9 M_\odot$ and $M_* \approx 10^{12} M_\odot$; all in all, star formation in galaxies is a very inefficient process. Such behavior is easily understood

in terms of infall/ condensation and feedback processes. At small masses, infall and condensation are efficient ($f_{inf} \approx 1$), but star formation is regulated by outflows from SNe and stellar winds; conversely we compare these relationships with the data concerning local ETGs and their high- z star-forming progenitors, finding a pleasing overall agreement .

The overall redshift evolution of the MS for ETGs and their progenitors is consistent with a scenario that traces the bulk of the star formation in galaxies back to local, in situ condensation processes. As shown in the right panel of Fig. B.3, specifically, at higher z and in massive galaxies, the interstellar medium is, on average, denser, and the condensation/ star formation timescales are shorter. Thus, star formation in a galaxy of a given stellar mass is higher, causing the MS locus to shift upward.

The gas metallicity depicted in the left panel of Fig. B.4 shows an increasing behavior as a function of the final stellar mass, related to the more efficient production of metals in galaxies with higher SFRs, that will also yield larger stellar masses; the corresponding redshift evolution is negligible, being the gas metallicity essentially related to in situ processes.

The stellar metallicity increases monotonically with stellar mass, mirroring the gas metallicity behavior which can be seen in the right panel of Fig. B.4. This is because massive galaxies are characterized, on average, by higher SFRs that imply larger stellar masses and metal production. Moreover, in low-mass galaxies, the depletion of metals by stellar feedback is enhanced due to the shallower potential wells associated with the host halos. Contrariwise, high-mass galaxies can retain greater amounts of chemical-enriched gas that could be converted and locked into new metal-rich stars, resulting in a higher stellar metallicity. The evolution in redshift is minor, as the stellar metallicity is mainly determined by in situ star formation processes in the central regions; if any, at higher z and a given stellar mass, the stellar metallicity increases slightly, since the average SFR is larger.

We remark that a major value of our approach is to reproduce, with a unique set of physically motivated parameters, a wealth of observables concerning ETGs and their progenitors. Another straightforward application of our solutions would be the description of the spatially averaged properties for local disk-dominated (e.g., spiral) galaxies. On the one hand, this will just require different prescriptions for parameter setting with respect to ETG progenitors. In a nutshell, we expect appreciably longer condensation/star formation timescales of the order of several Gyr and a minor role for BH feedback; this will originate a prolonged star formation history to low SFR levels and appreciable dilution from infalling matter, in turn implying slower accumulation of stellar mass, metals, and dust. On the other hand, additional processes like galactic fountains, differential winds, stellar mixing, and multizonal effects may play a relevant role in local spirals; this will require the basic framework to become more complex and the search for realistic analytic solutions more challenging.

To sum up, the analytic solutions provided here are based on idealized, albeit

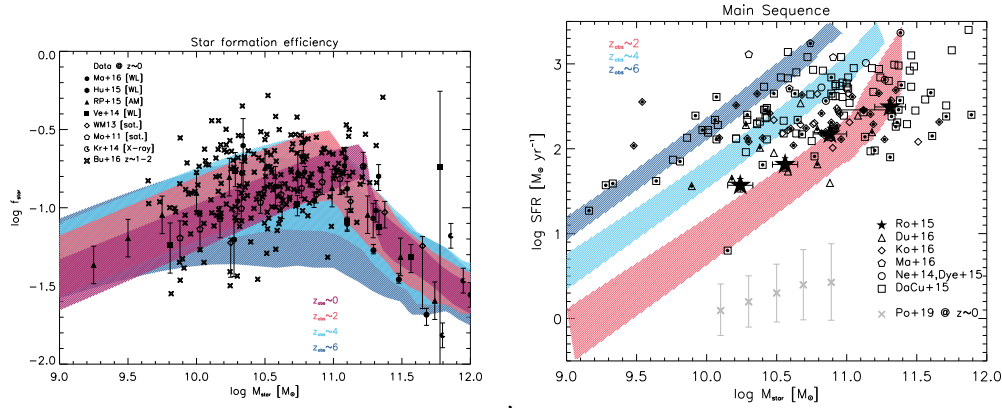


FIGURE B.3: Left panel: Star formation efficiency $f_* = M_*/f_b M_H$ vs. stellar mass M_* at different observation redshifts $z \approx 0$ (red), 2 (orange), 4 (cyan), and 6 (blue); the shaded areas illustrate the 1 variance associated with the average over different formation redshifts. Data points are from Mandelbaum et al. (2016, circles), Hudson et al. (2015, hexagons), and Velander et al. (2014, squares) via weak lensing; Rodríguez & Rubin (2005, triangles) via subhalo abundance matching; Wojtak & Mamon (2013, diamonds) and More et al. (2011, pentagons) via satellite kinematics; Kravtsov et al. (2018, pacmans) pacmans via X-ray observations of BCGs; and Burkert et al. (2016, crosses) via mass profile modeling of galaxies at $z \sim 1-2$. If not explicitly indicated, error bars are ≈ 0.25 dex. Right panel: The SFR vs. stellar mass M_* , alias the MS of star-forming galaxies, at different observation redshifts $z \approx 2$ (orange), 4 (cyan), and 6 (blue); the shaded areas illustrate the 1 variance associated with the average over different formation redshifts. The black filled stars are the observational determinations of the MS at $z \sim 2$ based on the statistics of large mass-selected samples by Rodighiero et al. (2015). The other symbols (error bars omitted for clarity) refer to far-IR data for individual objects at $z \sim 1-4$ (those in the range $z \sim 1.5-2.5$ are marked with a dot) by Dunlop et al. (2017, triangles), Koprowski et al. (2016, diamonds), Ma et al. (2016, pentagons), Negrello et al. (2014); Dye et al. (2015, circles) and da Cunha et al. (2015, squares); for reference, the determination at $z \approx 0$ by Popesso et al. (2019, crosses) is also reported.

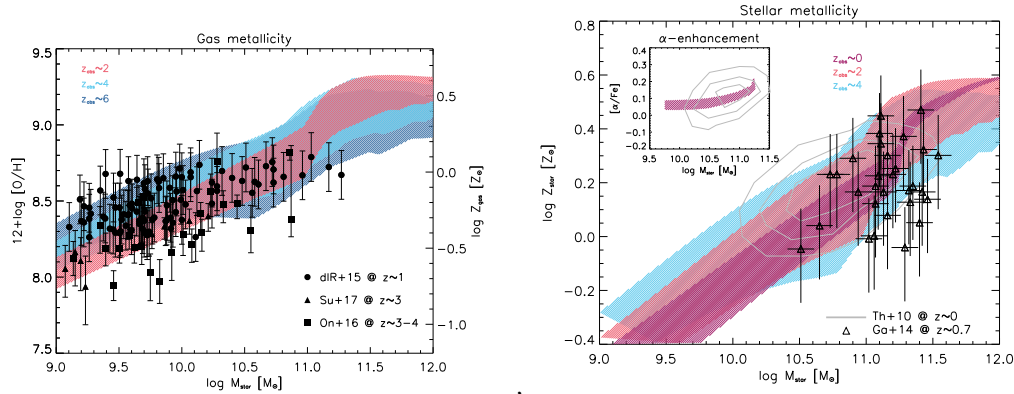


FIGURE B.4: Left panel: Gas metallicity Z_{gas} vs. stellar mass M_* at different observation redshifts, $z \approx 2$ (orange), 4 (cyan), and 6 (blue); the shaded areas illustrate the 1σ variance associated with the average over different formation redshifts. Data points are from [de los Reyes et al. \(2015, circles\)](#) at $z \sim 1$, [Suzuki et al. \(2017; triangles\)](#) at $z \sim 3$, and [Onodera et al. \(2016, squares\)](#) at $z \sim 3-4$. All gas metallicities have been converted to PP04O3N2 calibration. Right panel: Stellar metallicity Z_* vs. stellar mass M_* at different observation redshifts, $z \approx 0$ (red), 2 (orange), and 4 (cyan); the shaded areas illustrate the 1σ variance associated with the average over different formation redshifts. Data for SDSS samples of local ETGs are from [Thomas et al. \(2010, solid contours\)](#) solid contours, and data for individual galaxies at $z \sim 0.7$ are from [Gallazzi et al. \(2014, triangles\)](#). Inset: as above for α -element-to-iron abundance ratio $[\alpha/Fe]$ vs. stellar mass M_* at observation redshift $z \approx 0$ (red).

nontrivial, descriptions of the main physical processes regulating galaxy formation on a spatially average the ground that goes beyond simple approaches to the history of star formation and chemical enrichment, like the closed/leaky-box or gas-regulator models. Yet our solutions are simple enough to easily disentangle the roles of the main physical processes at work, allow quick exploration of the parameter space, and make transparent predictions on spatially averaged quantities. All in all, our analytic solutions may provide a basis for improving the (subgrid) physical recipes implemented in theoretical approaches and numerical simulations and can offer a benchmark for interpreting and forecasting current and future observations with multiband coverage that will become routinely achievable even at high redshift, e.g., via targeted observations with ALMA and dedicated surveys with the JWST.

Bibliography

- Abbott, B. P., Abbott, R., Abbott, T. D., et al. 2016, *Phys. Rev. Lett.*, 116, 061102
- Abbott, B. P., Abbott, R., Abbott, T. D., et al. 2016, *Phys. Rev. Lett.*, 116, 061102
- Abbott, B. P., Abbott, R., Abbott, T. D., et al. 2016a, *Phys. Rev. Lett.*, 116, 241103
- Abbott, B. P., Abbott, R., Abbott, T. D., et al. 2016b, *Phys. Rev. X*, 6, 041015
- Abbott, B. P., Abbott, R., Abbott, T. D., et al. 2019, *Physical Review X*, 9, 031040
- Abbott, B. P., Abbott, R., Abbott, T. D., et al. 2017a, *ApJ*, 851, L35
- Abbott, B. P., Abbott, R., Abbott, T. D., et al. 2017b, *ApJ*, 848, L12
- Abbott, B. P., Abbott, R., Abbott, T. D., et al. 2017c, *Phys. Rev. Lett.*, 119, 161101
- Abbott, B. P., Abbott, R., Abbott, T. D., et al. 2017, *Phys. Rev. Lett.*, 119, 141101
- Abbott, R., Abbott, T. D., Abraham, S., et al. 2020, *Phys. Rev. Lett.*, 125, 101102
- Aihara, H., Arimoto, N., Armstrong, R., et al. 2018, *PASJ*, 70, S4
- Akerman, C. J., Carigi, L., Nissen, P. E., Pettini, M., & Asplund, M. 2004, *A&A*, 414, 931
- Allende Prieto, C., Majewski, S. R., Schiavon, R., et al. 2008, *Astronomische Nachrichten*, 329, 1018
- Anders, F., Chiappini, C., Minchev, I., et al. 2017, *A&A*, 600, A70
- Arrigoni, M., Trager, S. C., Somerville, R. S., & Gibson, B. K. 2010, *MNRAS*, 402, 173
- Asano, R. S., Takeuchi, T. T., Hirashita, H., & Inoue, A. K. 2013, *Earth, Planets, and Space*, 65, 213
- Asplund, M., Grevesse, N., Sauval, A. J., & Scott, P. 2009, *ARA&A*, 47, 481
- Aumer, M., Binney, J., & Schönrich, R. 2017, *MNRAS*, 470, 3685
- Ballero, S. K., Matteucci, F., & Chiappini, C. 2006, *New A*, 11, 306
- Barack, L., Cardoso, V., Nissanke, S., et al. 2019, *Classical and Quantum Gravity*, 36, 143001

- Bekki, K. 2013, *MNRAS*, 436, 2254
- Bekki, K. 2015, *MNRAS*, 449, 1625
- Bekki, K. & Tsujimoto, T. 2011, *ApJ*, 738, 4
- Belczynski, K., Holz, D. E., Bulik, T., & O’Shaughnessy, R. 2016, *Nature*, 534, 512
- Belokurov, V., Erkal, D., Evans, N. W., Koposov, S. E., & Deason, A. J. 2018, *MNRAS*, 478, 611
- Bensby, T., Feltzing, S., & Oey, M. S. 2014, *A&A*, 562, A71
- Benson, A. J. 2012, *New A*, 17, 175
- Boco, L., Lapi, A., Goswami, S., et al. 2019, *ApJ*, 881, 157
- Boeche, C., Chiappini, C., Minchev, I., et al. 2013, *A&A*, 553, A19
- Bond, J. R., Arnett, W. D., & Carr, B. J. 1982, in *NATO Advanced Science Institutes (ASI) Series C*, Vol. 90, *NATO Advanced Science Institutes (ASI) Series C*, ed. M. J. Rees & R. J. Stoneham, 303–311
- Bond, J. R., Arnett, W. D., & Carr, B. J. 1984, *ApJ*, 280, 825
- Bressan, A., Marigo, P., Girardi, L., et al. 2012, *MNRAS*, 427, 127
- Buder, S., Lind, K., Ness, M. K., et al. 2019, *A&A*, 624, A19
- Burkert, A., Förster Schreiber, N. M., Genzel, R., et al. 2016, *ApJ*, 826, 214
- Burrows, A., Vartanyan, D., Dolence, J. C., Skinner, M. A., & Radice, D. 2018, *Space Sci. Rev.*, 214, 33
- Caffau, E., Ludwig, H.-G., Steffen, M., Freytag, B., & Bonifacio, P. 2011, *Sol. Phys.*, 268, 255
- Caffau, E., Maiorca, E., Bonifacio, P., et al. 2009, *A&A*, 498, 877
- Carretta, E., Gratton, R., Cohen, J. G., Beers, T. C., & Christlieb, N. 2002, *AJ*, 124, 481
- Casagrande, L., Schönrich, R., Asplund, M., et al. 2011, *A&A*, 530, A138
- Cayrel, R., Depagne, E., Spite, M., et al. 2004, *A&A*, 416, 1117
- Cayrel, R., Depagne, E., Spite, M., et al. 2003, *VizieR Online Data Catalog*, J/A+A/416/1117
- Chabrier, G. 2003, *PASP*, 115, 763

- Chen, K.-J., Woosley, S., Heger, A., Almgren, A., & Whalen, D. J. 2014, *ApJ*, 792, 28
- Chen, Y., Bressan, A., Girardi, L., et al. 2015, *MNRAS*, 452, 1068
- Cherchneff, I. & Dwek, E. 2009, *ApJ*, 703, 642
- Cherchneff, I. & Dwek, E. 2010, *ApJ*, 713, 1
- Chiappini, C., Hirschi, R., Meynet, G., et al. 2006, *A&A*, 449, L27
- Chiappini, C., Matteucci, F., & Ballero, S. K. 2005, *A&A*, 437, 429
- Chiappini, C., Matteucci, F., & Gratton, R. 1997, *ApJ*, 477, 765
- Chiappini, C., Matteucci, F., & Padoan, P. 2000, *ApJ*, 528, 711
- Chiappini, C., Matteucci, F., & Romano, D. 2001, *ApJ*, 554, 1044
- Chieffi, A. & Limongi, M. 2004, *ApJ*, 608, 405
- Chiosi, C., Bressan, A., Portinari, L., & Tantalo, R. 1998, *A&A*, 339, 355
- Christensen, L., Laursen, P., Richard, J., et al. 2012a, *MNRAS*, 427, 1973
- Christensen, L., Richard, J., Hjorth, J., et al. 2012b, *MNRAS*, 427, 1953
- Cole, S., Lacey, C. G., Baugh, C. M., & Frenk, C. S. 2000, *MNRAS*, 319, 168
- Costa, G., Bressan, A., Mapelli, M., et al. 2020a, arXiv e-prints, arXiv:2010.02242
- Costa, G., Bressan, A., Mapelli, M., et al. 2020b, arXiv e-prints, arXiv:2010.02242
- Costa, G., Girardi, L., Bressan, A., et al. 2019a, *A&A*, 631, A128
- Costa, G., Girardi, L., Bressan, A., et al. 2019b, *MNRAS*, 485, 4641
- Cousin, M., Buat, V., Boissier, S., et al. 2016, *A&A*, 589, A109
- Cristallo, S., Piersanti, L., Straniero, O., et al. 2011, *ApJS*, 197, 17
- Cristallo, S., Straniero, O., Gallino, R., et al. 2009, *ApJ*, 696, 797
- Cristallo, S., Straniero, O., Piersanti, L., & Gobrecht, D. 2015, *ApJS*, 219, 40
- Croton, D. J., Springel, V., White, S. D. M., et al. 2006, *MNRAS*, 365, 11
- Crowther, P. A. 2019, *Galaxies*, 7, 88
- Crowther, P. A., Caballero-Nieves, S. M., Bostroem, K. A., et al. 2016, *MNRAS*, 458, 624

- Cui, X.-Q., Zhao, Y.-H., Chu, Y.-Q., et al. 2012, *Research in Astronomy and Astrophysics*, 12, 1197
- da Cunha, E., Walter, F., Smail, I. R., et al. 2015, *ApJ*, 806, 110
- de Bennassuti, M., Schneider, R., Valiante, R., & Salvadori, S. 2014, *MNRAS*, 445, 3039
- de Jager, C., Nieuwenhuijzen, H., & van der Hucht, K. A. 1988, *A&AS*, 72, 259
- de Laverny, P., Recio-Blanco, A., Worley, C. C., et al. 2013, *The Messenger*, 153, 18
- de los Reyes, M. A., Ly, C., Lee, J. C., et al. 2015, *AJ*, 149, 79
- De Lucia, G., Fontanot, F., & Hirschmann, M. 2017, *MNRAS*, 466, L88
- De Lucia, G., Tornatore, L., Frenk, C. S., et al. 2014, *MNRAS*, 445, 970
- de Mink, S. E. & Belczynski, K. 2015, *ApJ*, 814, 58
- Doherty, C. L., Gil-Pons, P., Lau, H. H. B., Lattanzio, J. C., & Siess, L. 2014, *MNRAS*, 437, 195
- Doherty, C. L., Gil-Pons, P., Siess, L., & Lattanzio, J. C. 2017, *PASA*, 34, e056
- Draine, B. T. 2011, *Physics of the Interstellar and Intergalactic Medium*
- Dubois, Y., Peirani, S., Pichon, C., et al. 2016, *MNRAS*, 463, 3948
- Dubois, Y., Pichon, C., Welker, C., et al. 2014, *MNRAS*, 444, 1453
- Dunlop, J. S., McLure, R. J., Biggs, A. D., et al. 2017, *MNRAS*, 466, 861
- Dvorkin, I., Uzan, J.-P., Vangioni, E., & Silk, J. 2018, *MNRAS*, 479, 121
- Dwek, E. 1998, *ApJ*, 501, 643
- Dwek, E. & Cherchneff, I. 2011, *ApJ*, 727, 63
- Dye, S., Furlanetto, C., Swinbank, A. M., et al. 2015, *MNRAS*, 452, 2258
- Elmegreen, B. G. & Shadmehri, M. 2003, *MNRAS*, 338, 817
- Erb, D. K. 2008, *ApJ*, 674, 151
- Ertl, T., Janka, H.-T., Woosley, S. E., Sukhbold, T., & Ugliano, M. 2016, *ApJ*, 818, 124
- Esteban, C., Bresolin, F., Peimbert, M., et al. 2009, *ApJ*, 700, 654
- Evans, C. J., Walborn, N. R., Crowther, P. A., et al. 2010, *ApJ*, 715, L74

- Farmer, R., Renzo, M., de Mink, S. E., Marchant, P., & Justham, S. 2019, *ApJ*, 887, 53
- Feltzing, S., Bensby, T., & Lundström, I. 2003, *A&A*, 397, L1
- Ferrini, F., Molla, M., Pardi, M. C., & Diaz, A. I. 1994, *ApJ*, 427, 745
- Fishbach, M., Gray, R., Magaña Hernandez, I., et al. 2019, *ApJ*, 871, L13
- Fontanot, F., De Lucia, G., Hirschmann, M., et al. 2017, *MNRAS*, 464, 3812
- Fryer, C. L. 1999, *ApJ*, 522, 413
- Fryer, C. L., Belczynski, K., Wiktorowicz, G., et al. 2012, *ApJ*, 749, 91
- Fryer, C. L. & Kalogera, V. 2001, *ApJ*, 554, 548
- Fryer, C. L., Young, P. A., & Hungerford, A. L. 2006, *ApJ*, 650, 1028
- Fu, X., Bressan, A., Marigo, P., et al. 2018, *MNRAS*, 476, 496
- Fuhrmann, K. 2011, *MNRAS*, 414, 2893
- Fulbright, J. P. 2000, *AJ*, 120, 1841
- Gaia Collaboration, Brown, A. G. A., Vallenari, A., et al. 2018, *A&A*, 616, A1
- Gallazzi, A., Bell, E. F., Zibetti, S., Brinchmann, J., & Kelson, D. D. 2014, *ApJ*, 788, 72
- García-Berro, E., Ritossa, C., & Iben, Icko, J. 1997, *ApJ*, 485, 765
- Genel, S., Vogelsberger, M., Springel, V., et al. 2014, *MNRAS*, 445, 175
- Genzel, R., Förster Schreiber, N. M., Übler, H., et al. 2017, *Nature*, 543, 397
- Genzel, R., Price, S. H., Übler, H., et al. 2020, *ApJ*, 902, 98
- Gilmore, G., Randich, S., Asplund, M., et al. 2012, *The Messenger*, 147, 25
- Girardi, L., Williams, B. F., Gilbert, K. M., et al. 2010, *ApJ*, 724, 1030
- Gräfener, G. 2008, in *Clumping in Hot-Star Winds*, ed. W.-R. Hamann, A. Feldmeier, & L. M. Oskinova, 103
- Grand, R. J. J., Bustamante, S., Gómez, F. A., et al. 2018, *MNRAS*, 474, 3629
- Gratton, R. G. & Sneden, C. 1988, *A&A*, 204, 193
- Grisoni, V., Spitoni, E., & Matteucci, F. 2018, *MNRAS*, 481, 2570
- Grisoni, V., Spitoni, E., Matteucci, F., et al. 2017, *MNRAS*, 472, 3637

- Haemmerlé, L., Woods, T. E., Klessen, R. S., Heger, A., & Whalen, D. J. 2018, *MNRAS*, 474, 2757
- Haft, M., Raffelt, G., & Weiss, A. 1994, *ApJ*, 425, 222
- Han, Z.-W., Ge, H.-W., Chen, X.-F., & Chen, H.-L. 2020, *Research in Astronomy and Astrophysics*, 20, 161
- Haywood, M., Di Matteo, P., Lehnert, M. D., et al. 2018, *ApJ*, 863, 113
- Heger, A., Fryer, C. L., Woosley, S. E., Langer, N., & Hartmann, D. H. 2003a, *ApJ*, 591, 288
- Heger, A., Fryer, C. L., Woosley, S. E., Langer, N., & Hartmann, D. H. 2003b, *ApJ*, 591, 288
- Heger, A. & Woosley, S. E. 2002, *ApJ*, 567, 532
- Helmi, A., Babusiaux, C., Koppelman, H. H., et al. 2018, *Nature*, 563, 85
- Herwig, F. 2000, *A&A*, 360, 952
- Herwig, F. 2005, *ARA&A*, 43, 435
- Hirashita, H. 2000, *PASJ*, 52, 585
- Hirschauer, A. S., Salzer, J. J., Skillman, E. D., et al. 2016, *ApJ*, 822, 108
- Hirschmann, M., De Lucia, G., & Fontanot, F. 2016, *MNRAS*, 461, 1760
- Hopkins, P. F., Kereš, D., Oñorbe, J., et al. 2014, *MNRAS*, 445, 581
- Hopkins, P. F., Wetzel, A., Kereš, D., et al. 2018, *MNRAS*, 480, 800
- Hosek, Matthew W., J., Lu, J. R., Anderson, J., et al. 2019, *ApJ*, 870, 44
- Hsyu, T., Cooke, R. J., Prochaska, J. X., & Bolte, M. 2017, *ApJ*, 845, L22
- Hudson, M. J., Gillis, B. R., Coupon, J., et al. 2015, *MNRAS*, 447, 298
- Hurley, J. R., Pols, O. R., & Tout, C. A. 2000, *MNRAS*, 315, 543
- Hurley, J. R., Tout, C. A., & Pols, O. R. 2002, *Monthly Notices of the Royal Astronomical Society*, 329, 897
- Iben, Icko, J., Ritossa, C., & García-Berro, E. 1997, *ApJ*, 489, 772
- Iglesias, C. A. & Rogers, F. J. 1996, *ApJ*, 464, 943
- Inoue, A. K. 2003, *PASJ*, 55, 901
- Isobe, Y., Ouchi, M., Kojima, T., et al. 2020, arXiv e-prints, arXiv:2004.11444

- Israelian, G., Ecuillon, A., Rebolo, R., et al. 2004, *A&A*, 421, 649
- Itoh, N. & Kohyama, Y. 1983, *ApJ*, 275, 858
- Itoh, N., Uchida, S., Sakamoto, Y., Kohyama, Y., & Nozawa, S. 2008, *ApJ*, 677, 495
- Iwamoto, K., Brachwitz, F., Nomoto, K., et al. 1999, *ApJS*, 125, 439
- Izotov, Y. I., Guseva, N. G., Fricke, K. J., & Papaderos, P. 2009, *A&A*, 503, 61
- Izotov, Y. I., Stasińska, G., Meynet, G., Guseva, N. G., & Thuan, T. X. 2006, *A&A*, 448, 955
- Izotov, Y. I. & Thuan, T. X. 1998, *ApJ*, 500, 188
- Izotov, Y. I., Thuan, T. X., & Guseva, N. G. 2012, *A&A*, 546, A122
- Izotov, Y. I., Thuan, T. X., & Guseva, N. G. 2019, *MNRAS*, 483, 5491
- Izotov, Y. I., Thuan, T. X., Guseva, N. G., & Liss, S. E. 2018a, *MNRAS*, 473, 1956
- Izotov, Y. I., Thuan, T. X., Guseva, N. G., & Liss, S. E. 2018b, *MNRAS*, 473, 1956
- Janka, H.-T. 2012, *Annual Review of Nuclear and Particle Science*, 62, 407
- Jeřábková, T., Hasani Zonoozi, A., Kroupa, P., et al. 2018, *A&A*, 620, A39
- Jurić, M., Ivezić, Ž., Brooks, A., et al. 2008, *ApJ*, 673, 864
- Kalogera, V. & Baym, G. 1996, *ApJ*, 470, L61
- Karakas, A. I. 2010, *MNRAS*, 403, 1413
- Karakas, A. I. & Lugaro, M. 2016, *ApJ*, 825, 26
- Karakas, A. I., Lugaro, M., Carlos, M., et al. 2018, *MNRAS*, 477, 421
- Karlsson, T., Johnson, J. L., & Bromm, V. 2008, *The Astrophysical Journal*, 679, 6
- Kauffmann, G., White, S. D. M., & Guiderdoni, B. 1993, *MNRAS*, 264, 201
- Kawata, D. & Chiappini, C. 2016, *Astronomische Nachrichten*, 337, 976
- Kojima, T., Ouchi, M., Rauch, M., et al. 2020a, arXiv e-prints, arXiv:2006.03831
- Kojima, T., Ouchi, M., Rauch, M., et al. 2020b, *ApJ*, 898, 142
- Koprowski, M. P., Dunlop, J. S., Michałowski, M. J., et al. 2016, *MNRAS*, 458, 4321

- Kozyreva, A., Blinnikov, S., Langer, N., & Yoon, S.-C. 2014a, *A&A*, 565, A70
- Kozyreva, A., Yoon, S.-C., & Langer, N. 2014b, *A&A*, 566, A146
- Kozyreva, A., Yoon, S.-C., & Langer, N. 2014c, *A&A*, 566, A146
- Kravtsov, A. V., Vikhlinin, A. A., & Meshcheryakov, A. V. 2018, *Astronomy Letters*, 44, 8
- Kroupa, P. 2001, *MNRAS*, 322, 231
- Kroupa, P. 2008, in *Astronomical Society of the Pacific Conference Series*, Vol. 390, *Pathways Through an Eclectic Universe*, ed. J. H. Knapen, T. J. Mahoney, & A. Vazdekis, 3
- Kroupa, P., Tout, C. A., & Gilmore, G. 1993, *MNRAS*, 262, 545
- Kroupa, P. & Weidner, C. 2003, *ApJ*, 598, 1076
- Kubryk, M., Prantzos, N., & Athanassoula, E. 2015, *A&A*, 580, A126
- Kunth, D. & Östlin, G. 2000, *A&A Rev.*, 10, 1
- Lacey, C. & Cole, S. 1993, *MNRAS*, 262, 627
- Lacey, C. G., Baugh, C. M., Frenk, C. S., et al. 2016, *MNRAS*, 462, 3854
- Langer, N., Norman, C. A., de Koter, A., et al. 2007, *A&A*, 475, L19
- Larson, R. B. 1972, *Nature*, 236, 21
- Lawlor, T. M., Young, T. R., Johnson, T. A., & MacDonald, J. 2008, *MNRAS*, 384, 1533
- Lebzelter, T., Mowlavi, N., Marigo, P., et al. 2018, *A&A*, 616, L13
- Leung, S.-C., Nomoto, K., & Blinnikov, S. 2019, *ApJ*, 887, 72
- Leung, S.-C., Nomoto, K., & Suzuki, T. 2020, *ApJ*, 889, 34
- Liao, K., Fan, X.-L., Ding, X., Biesiada, M., & Zhu, Z.-H. 2017, *Nature Communications*, 8, 1148
- Lilly, S. J., Carollo, C. M., Pipino, A., Renzini, A., & Peng, Y. 2013, *ApJ*, 772, 119
- Limongi, M. & Chieffi, A. 2003, *ApJ*, 592, 404
- Limongi, M. & Chieffi, A. 2006, *ApJ*, 647, 483
- Limongi, M. & Chieffi, A. 2018, *VizieR Online Data Catalog*, J/ApJS/237/13
- Lynden-Bell, D. 1975, *Vistas in Astronomy*, 19, 299

- Ma, J., Gonzalez, A. H., Vieira, J. D., et al. 2016, *ApJ*, 832, 114
- Mainali, R., Kollmeier, J. A., Stark, D. P., et al. 2017, *ApJ*, 836, L14
- Maiolino, R. & Mannucci, F. 2019, *A&A Rev.*, 27, 3
- Majewski, S. R., Schiavon, R. P., Frinchaboy, P. M., et al. 2017, *AJ*, 154, 94
- Mandelbaum, R., Wang, W., Zu, Y., et al. 2016, *MNRAS*, 457, 3200
- Mapelli, M. & Giacobbo, N. 2018, *MNRAS*, 479, 4391
- Marchant, P. & Moriya, T. J. 2020, *A&A*, 640, L18
- Marigo, P. 2001, *A&A*, 370, 194
- Marigo, P. & Aringer, B. 2009, *A&A*, 508, 1539
- Marigo, P., Bressan, A., Nanni, A., Girardi, L., & Pumo, M. L. 2013, *MNRAS*, 434, 488
- Marigo, P., Chiosi, C., & Kudritzki, R. P. 2003, *A&A*, 399, 617
- Marigo, P., Cummings, J. D., Curtis, J. L., et al. 2020, *Nature Astronomy* [[arXiv]2007.04163]
- Marigo, P., Girardi, L., Bressan, A., et al. 2017, *ApJ*, 835, 77
- Marigo, P., Girardi, L., Chiosi, C., & Wood, P. R. 2001, *A&A*, 371, 152
- Marks, M., Kroupa, P., Dabringhausen, J., & Pawlowski, M. S. 2012, *MNRAS*, 422, 2246
- Matteucci, F. 1986, *MNRAS*, 221, 911
- Matteucci, F. 2001, *The chemical evolution of the Galaxy*, Vol. 253
- Matteucci, F. 2002
- Matteucci, F. 2014, *Saas-Fee Advanced Course*, 37, 145
- Matteucci, F. 2016, *Journal of Physics: Conference Series*, 703, 012004
- Matteucci, F. & Brocato, E. 1990, *ApJ*, 365, 539
- Matteucci, F. & Francois, P. 1989a, *MNRAS*, 239, 885
- Matteucci, F. & Francois, P. 1989b, *MNRAS*, 239, 885
- Matteucci, F. & Greggio, L. 1986a, *A&A*, 154, 279
- Matteucci, F. & Greggio, L. 1986b, *A&A*, 154, 279

- Matteucci, F., Grisoni, V., Spitoni, E., et al. 2019, *MNRAS*, 487, 5363
- Matteucci, F. & Pipino, A. 2005, *MNRAS*, 357, 489
- Matteucci, F., Vasini, A., Grisoni, V., & Schultheis, M. 2020, *MNRAS*, 494, 5534
- McAlpine, S., Helly, J. C., Schaller, M., et al. 2016, *Astronomy and Computing*, 15, 72
- McAlpine, S., Smail, I., Bower, R. G., et al. 2019, *MNRAS*, 488, 2440
- McWilliam, A., Preston, G. W., Sneden, C., & Searle, L. 1995, *AJ*, 109, 2757
- Micali, A., Matteucci, F., & Romano, D. 2013, *MNRAS*, 436, 1648
- Mikolaitis, Š., de Laverny, P., Recio-Blanco, A., et al. 2017, *A&A*, 600, A22
- Miyazaki, S., Komiyama, Y., Kawanomoto, S., et al. 2018, *PASJ*, 70, S1
- Mo, H., van den Bosch, F. C., & White, S. 2010, *Galaxy Formation and Evolution*
- More, S., van den Bosch, F. C., Cacciato, M., et al. 2011, *MNRAS*, 410, 210
- Munakata, H., Kohyama, Y., & Itoh, N. 1985, *ApJ*, 296, 197
- Naab, T. & Ostriker, J. P. 2006, *MNRAS*, 366, 899
- Negrello, M., Hopwood, R., Dye, S., et al. 2014, *MNRAS*, 440, 1999
- Nissanke, S., Holz, D. E., Dalal, N., et al. 2013, arXiv e-prints, arXiv:1307.2638
- Nomoto, K. 1984, *ApJ*, 277, 791
- Nomoto, K., Kobayashi, C., & Tominaga, N. 2013, *ARA&A*, 51, 457
- Nomoto, K., Tominaga, N., Umeda, H., Kobayashi, C., & Maeda, K. 2006, *Nuclear Physics A*, 777, 424
- O'Connor, E. & Ott, C. D. 2011, *ApJ*, 730, 70
- Ohkubo, T., Nomoto, K., Umeda, H., Yoshida, N., & Tsuruta, S. 2009, *ApJ*, 706, 1184
- Ohkubo, T., Umeda, H., Maeda, K., et al. 2006, *ApJ*, 645, 1352
- Onodera, M., Carollo, C. M., Lilly, S., et al. 2016, *ApJ*, 822, 42
- O'Shaughnessy, R., Kalogera, V., & Belczynski, K. 2010, *ApJ*, 716, 615
- Pagel, B. E. J. & Edmunds, M. G. 1981, *ARA&A*, 19, 77
- Pantoni, L., Lapi, A., Massardi, M., Goswami, S., & Danese, L. 2019, *ApJ*, 880, 129

- Pastorelli, G., Marigo, P., Girardi, L., et al. 2020, *MNRAS*, 498, 3283
- Pastorelli, G., Marigo, P., Girardi, L., et al. 2019, *MNRAS*, 485, 5666
- Pettini, M., Zych, B. J., Steidel, C. C., & Chaffee, F. H. 2008, *MNRAS*, 385, 2011
- Pignatari, M., Herwig, F., Hirschi, R., et al. 2016, *ApJS*, 225, 24
- Plevne, O., Önal Taş, Ö., Bilir, S., & Seabroke, G. M. 2020, *ApJ*, 893, 108
- Poelarends, A. J. T., Herwig, F., Langer, N., & Heger, A. 2008, *ApJ*, 675, 614
- Popesso, P., Concas, A., Morselli, L., et al. 2019, *MNRAS*, 483, 3213
- Porter, L. A., Somerville, R. S., Primack, J. R., et al. 2014, *MNRAS*, 445, 3092
- Portinari, L. & Chiosi, C. 1999, *A&A*, 350, 827
- Portinari, L., Chiosi, C., & Bressan, A. 1998, *A&A*, 334, 505
- Prantzos, N., Abia, C., Limongi, M., Chieffi, A., & Cristallo, S. 2018, *MNRAS*, 476, 3432
- Prantzos, N. & Aubert, O. 1995, *A&A*, 302, 69
- Prantzos, N., Boehm, C., Bykov, A. M., et al. 2011, *Rev. Mod. Phys.*, 83, 1001
- Prochaska, J. X., Naumov, S. O., Carney, B. W., McWilliam, A., & Wolfe, A. M. 2000, *AJ*, 120, 2513
- Pustilnik, S. A., Kniazev, A. Y., & Pramskij, A. G. 2005, *A&A*, 443, 91
- Renzo, M., Farmer, R. J., Justham, S., et al. 2020, *MNRAS*, 493, 4333
- Ricotti, M. & Ostriker, J. P. 2004, *MNRAS*, 350, 539
- Ritossa, C., Garcia-Berro, E., & Iben, Icko, J. 1996, *ApJ*, 460, 489
- Ritter, C., Herwig, F., Jones, S., et al. 2018, *MNRAS*, 480, 538
- Robitaille, T. P. & Whitney, B. A. 2010, *ApJ*, 710, L11
- Rodighiero, G., Brusa, M., Daddi, E., et al. 2015, *ApJ*, 800, L10
- Rodríguez, M. & Rubin, R. H. 2005, *ApJ*, 626, 900
- Roederer, I. U., Preston, G. W., Thompson, I. B., et al. 2014, *AJ*, 147, 136
- Rollinde, E., Vangioni, E., Maurin, D., et al. 2009, *MNRAS*, 398, 1782
- Romano, D., Franchini, M., Grisoni, V., et al. 2020, *A&A*, 639, A37
- Romano, D., Karakas, A. I., Tosi, M., & Matteucci, F. 2010, *A&A*, 522, A32

- Romano, D., Matteucci, F., Zhang, Z.-Y., Ivison, R. J., & Ventura, P. 2019, MNRAS, 490, 2838
- Romano, D., Matteucci, F., Zhang, Z. Y., Papadopoulos, P. P., & Ivison, R. J. 2017, MNRAS, 470, 401
- Rosenfield, P., Marigo, P., Girardi, L., et al. 2014, ApJ, 790, 22
- Rosenfield, P., Marigo, P., Girardi, L., et al. 2016, ApJ, 822, 73
- Sahijpal, S. 2014, International Journal of Astronomy and Astrophysics, 4, 491
- Savino, A., Koch, A., Prudil, Z., Kunder, A., & Smolec, R. 2020, A&A, 641, A96
- Schaye, J., Crain, R. A., Bower, R. G., et al. 2015, MNRAS, 446, 521
- Schmidt, M. 1963, ApJ, 137, 758
- Schneider, F. R. N., Sana, H., Evans, C. J., et al. 2018, Science, 359, 69
- Schönrich, R. & Aumer, M. 2017, MNRAS, 472, 3979
- Schönrich, R., Binney, J., & Dehnen, W. 2010, MNRAS, 403, 1829
- Senchyna, P., Stark, D. P., Charlot, S., et al. 2020, arXiv e-prints, arXiv:2008.09780
- Siess, L. 2006, A&A, 448, 717
- Siess, L. 2007, A&A, 476, 893
- Silk, J. & Mamon, G. A. 2012, Research in Astronomy and Astrophysics, 12, 917
- Silva, L., Granato, G. L., Bressan, A., & Danese, L. 1998, ApJ, 509, 103
- Skillman, E. D., Salzer, J. J., Berg, D. A., et al. 2013, AJ, 146, 3
- Slemer, A. 2016, *Investigating chemical enrichment scenarios fro massive stars*, PhD Thesis, Department of Physics and Astronomy, Padova University
- Slemer, A., Marigo, P., Piatti, D., et al. 2017, MNRAS, 465, 4817
- Snaith, O. N., Haywood, M., Di Matteo, P., et al. 2014, ApJ, 781, L31
- Somerville, R. S., Hopkins, P. F., Cox, T. J., Robertson, B. E., & Hernquist, L. 2008, MNRAS, 391, 481
- Spera, M. & Mapelli, M. 2017, MNRAS, 470, 4739
- Spera, M., Mapelli, M., & Bressan, A. 2015, MNRAS, 451, 4086
- Spera, M., Mapelli, M., Giacobbo, N., et al. 2019, MNRAS, 485, 889

- Spite, M., Cayrel, R., Plez, B., et al. 2005, *A&A*, 430, 655
- Stanway, E. R. & Eldridge, J. J. 2018, *Monthly Notices of the Royal Astronomical Society*, 479, 75–93
- Stark, D. P., Ellis, R. S., Charlot, S., et al. 2017, *MNRAS*, 464, 469
- Suárez-Andrés, L., Israelian, G., González Hernández, J. I., et al. 2016, *A&A*, 591, A69
- Sukhbold, T., Ertl, T., Woosley, S. E., Brown, J. M., & Janka, H. T. 2016, *ApJ*, 821, 38
- Takahashi, K. 2018, *ApJ*, 863, 153
- Takahashi, K., Yoshida, T., & Umeda, H. 2018, *ApJ*, 857, 111
- Talbot, Raymond J., J. & Arnett, W. D. 1971, *ApJ*, 170, 409
- Tang, J., Bressan, A., Rosenfield, P., et al. 2014, *MNRAS*, 445, 4287
- Taylor, S. R. & Gair, J. R. 2012, *Phys. Rev. D*, 86, 023502
- Tews, I. & Schwenk, A. 2020, *ApJ*, 892, 14
- Thielemann, F.-K., Hirschi, R., Liebendörfer, M., & Diehl, R. 2011, in *Lecture Notes in Physics*, Berlin Springer Verlag, Vol. 812, *Lecture Notes in Physics*, Berlin Springer Verlag, ed. R. Diehl, D. H. Hartmann, & N. Prantzos, 153–232
- Thomas, D., Maraston, C., Schawinski, K., Sarzi, M., & Silk, J. 2010, *MNRAS*, 404, 1775
- Thuan, T. X. & Izotov, Y. I. 2005, *ApJS*, 161, 240
- Timmes, F. X., Woosley, S. E., & Weaver, T. A. 1995, *ApJS*, 98, 617
- Tomkin, J., Lemke, M., Lambert, D. L., & Sneden, C. 1992, *AJ*, 104, 1568
- Ugliano, M., Janka, H.-T., Marek, A., & Arcones, A. 2012, *ApJ*, 757, 69
- Umeda, H. & Nomoto, K. 2002, *ApJ*, 565, 385
- Umeda, H. & Nomoto, K. 2008, *ApJ*, 673, 1014
- Utrobin, V. P. & Chugai, N. N. 2009, *A&A*, 506, 829
- Utrobin, V. P., Chugai, N. N., & Botticella, M. T. 2010, *ApJ*, 723, L89
- Valentini, M., Borgani, S., Bressan, A., et al. 2019, *MNRAS*, 485, 1384
- Valiante, R., Schneider, R., Bianchi, S., & Andersen, A. C. 2009, *MNRAS*, 397, 1661

- van Dokkum, P., Conroy, C., Villaume, A., Brodie, J., & Romanowsky, A. J. 2017, *The Astrophysical Journal*, 841, 68
- van Dokkum, P. G. & Conroy, C. 2012, *ApJ*, 760, 70
- Vanzella, E., Calura, F., Meneghetti, M., et al. 2017, *MNRAS*, 467, 4304
- Velander, M., van Uitert, E., Hoekstra, H., et al. 2014, *MNRAS*, 437, 2111
- Ventura, P. & D'Antona, F. 2009, *A&A*, 499, 835
- Ventura, P., Di Criscienzo, M., Carini, R., & D'Antona, F. 2013, *MNRAS*, 431, 3642
- Ventura, P., Karakas, A., Dell'Agli, F., García-Hernández, D. A., & Guzman-Ramirez, L. 2018, *MNRAS*, 475, 2282
- Ventura, P., Stanghellini, L., Dell'Agli, F., & García-Hernández, D. A. 2017, *MNRAS*, 471, 4648
- Vera-Ciro, C., D'Onghia, E., & Navarro, J. F. 2016, *ApJ*, 833, 42
- Vincenzo, F., Belfiore, F., Maiolino, R., Matteucci, F., & Ventura, P. 2016, *MNRAS*, 458, 3466
- Vink, J. S., de Koter, A., & Lamers, H. J. G. L. M. 2000, *A&A*, 362, 295
- Vink, J. S., Muijres, L. E., Anthonisse, B., et al. 2011, *A&A*, 531, A132
- Vitale, S., Farr, W. M., Ng, K. K. Y., & Rodriguez, C. L. 2019, *ApJ*, 886, L1
- Vogelsberger, M., Genel, S., Springel, V., et al. 2014, *MNRAS*, 444, 1518
- Walborn, N. R., Sana, H., Simón-Díaz, S., et al. 2014, *A&A*, 564, A40
- Wanajo, S., Nomoto, K., Janka, H. T., Kitaura, F. S., & Müller, B. 2009, *ApJ*, 695, 208
- Weidner, C. & Kroupa, P. 2005, *Astronomische Nachrichten*, 326, 605
- Weinstein, A. J. 2012, *Classical and Quantum Gravity*, 29, 124012
- Wisnioski, E., Förster Schreiber, N. M., Wuyts, S., et al. 2015, *ApJ*, 799, 209
- Wojtak, R. & Mamon, G. A. 2013, *MNRAS*, 428, 2407
- Wolfe, A. M., Gawiser, E., & Prochaska, J. X. 2005, *ARA&A*, 43, 861
- Woosley, S. E. 2016
- Woosley, S. E. 2017, *ApJ*, 836, 244
- Woosley, S. E., Blinnikov, S., & Heger, A. 2007, *Nature*, 450, 390

- Woosley, S. E. & Heger, A. 2015, in *Astrophysics and Space Science Library*, Vol. 412, *Very Massive Stars in the Local Universe*, ed. J. S. Vink, 199
- Woosley, S. E., Heger, A., & Weaver, T. A. 2002, *Reviews of Modern Physics*, 74, 1015
- Woosley, S. E. & Weaver, T. A. 1995, *ApJS*, 101, 181
- Wuyts, S., Förster Schreiber, N. M., Wisnioski, E., et al. 2016, *ApJ*, 831, 149
- Yoon, S. C., Dierks, A., & Langer, N. 2012, *A&A*, 542, A113
- Yoshida, T., Umeda, H., Maeda, K., & Ishii, T. 2016, *MNRAS*, 457, 351
- Yusof, N., Hirschi, R., Meynet, G., et al. 2013, *Monthly Notices of the Royal Astronomical Society*, 433, 1114
- Zhukovska, S., Gail, H. P., & Tieloff, M. 2008, *A&A*, 479, 453
- Zucker, D. B., de Silva, G., Freeman, K., Bland -Hawthorn, J., & Hermes Team. 2012, in *Astronomical Society of the Pacific Conference Series*, Vol. 458, *Galactic Archaeology: Near-Field Cosmology and the Formation of the Milky Way*, ed. W. Aoki, M. Ishigaki, T. Suda, T. Tsujimoto, & N. Arimoto, 421